Design of dual-action & selective Histone Deacetylase enzyme inhibitors

DENNINGTON, MARCUS,RYAN

Design of dual-action & selective Histone Deacetylase enzyme inhibitors

Marcus Dennington

A thesis submitted for the degree of Master of Science

Department of Chemistry

September 2023

ABSTRACT

Carcinogenesis cannot be explained only by genetic alterations. Epigenetic processes such as histone modification via (de)acetylation play a key role in gene expression, where overexpression of histone deacetylase (HDAC) enzymes, can result in aberrant transcription of key genes regulating important cellular functions such as cell proliferation, cell-cycle regulation and apoptosis. Herein we report the synthesis of novel organometallic HDAC inhibitors based upon copper(II) and ruthenium(II), with a view to designing new anticancer agents. An emerging area in the field of HDAC inhibitors is the design of dual-action inhibitors, focussing on the inclusion of copper(II) into the design to harness the DNA targeting and therapeutic effects of copper(II) generally, in addition to the potency of drugs inhibiting HDAC enzymes. In this study a novel copper(II) complex, dichloro(N^{20}-hydroxy-N^{11}-(1,10-phenanthrolin-5-yl)octanediamide)copper(II), was synthesised, inhibiting HDAC activity by 50% *in-vitro* at a lower concentration than clinically approved vorinostat (SAHA), attributing an IC_{50} = 0.32 ± 0.02 µM, compared to SAHA's IC_{50} = 0.70 ± 0.05 µM.

There is a growing body of evidence to suggest that enhanced potency of HDAC inhibitors lies in the design of inhibitors that selectivity inhibit particular HDAC enzymes within the family of 11 zinc-dependent HDACs. The ability of selective recognition using organometallics has been realised through the design of piano stool ruthenium complexes, where variation in the capping arene leads to differences in HDAC isoform selectivity. We report the synthesis of 11 novel ruthenium(II) piano stool complexes which are awaiting a series of HDAC selectivity assays to determine their superior potency.

Overall, this study illustrates the crucial importance of HDAC inhibitors in oncology, the tuneability of such complexes, and the remaining potential of these inhibitors in the design of dual-action and enzyme-selective analogues.

ACKNOWLEDGEMENTS

It is difficult to know where to begin in writing these acknowledgements since there are just so many people that have made my experience at Durham truly remarkable. Of course, I must start with a huge thank you to my supervisor Dr. James Walton. James, you have been so incredibly supportive throughout my study and I truly miss our meetings in which we would spend hours brainstorming so many different pathways to our targets – it was a chemists dream!

There is no way I could have made it through this degree without the support from the Walton Group. I am not sure anything could have prepared me for the stark realisation that what may appear sound, logical theoretical chemistry, does not always result in the anticipated outcome.

Overall, I have never learnt so much from a degree in so many different ways. I reflect and see such a naive chemist back in September 2021, and feel a true appreciation for the dedication it takes to contribute to any scientific field.

Thank you very much James, and thank you to the Walton Group as a whole – you are all awesome!

| CONTENTS

1 | INTRODUCTION 5

1.1 Platinum – Anticancer agents 7

1.2 Ruthenium – Anticancer agents 13

1.3 Copper – Anticancer agents 17

1.4 Histone deacetylase enzyme inhibitors 20

1.5 Dual-action histone deacetylase inhibitors 25

1.6 Project aims 27

2 | RESULTS & DISCUSSION 29

2.1 Synthesis of copper(II) phenanthroline HDAC inhibitor 29

2.2 Copper(II) pyrithione HDAC inhibitors 40

2.3 Ruthenium piano stool complexes 61

3 | CONCLUSIONS & FUTURE WORK 69

4 | EXPERIMENTAL 73

4.1 General methods 73

4.2 Histone deacetylase inhibition assay procedure 73

4.3 General method for High Performance Liquid Chromatography purification 74

4.4 Synthetic methods 74

4.5 NMR spectra 90

5 | REFERENCES 127

1 | INTRODUCTION

The term cancer refers to more than 277 different types of cancer disease. It is the second largest cause of mortality globally, where in 2021, it was estimated that 1,898,160 victims suffered and ~32% died due to this disease in the United States alone.[1,2] Cancer poses huge complications in its diagnosis and treatment due to the variety of this disease at the tissue level. Scientists have identified different stages of cancers, indicating that several gene mutations are involved in cancer pathogenesis.[3] Such mutations to the gene lead to abnormal cell proliferation, where genetic disorders caused by inheritance factors or lifestyle choices have a pivotal role in the mutation and cell growth rate.[4]

Prostate, breast and blood cancer are the most common types of cancer that affect men, women and children, respectively.[5,6] Particular chemical compounds have an obvious role in forming gene mutations, and therefore increase the likelihood of successive mutations leading to cancerous cells. Smoking is the most common example of how a lifestyle choice can influence the onset of cancer, where the carcinogenic chemical compounds in tobacco are believed to account for 20% of all cancers.[7] Overall, it is estimated that over a third of cancers could be prevented with a healthier lifestyle, through controlling factors such as diet, weight, alcohol consumption and physical activity, in addition to smoking.[8] Aside from lifestyle factors, the environment possesses chemical substances with carcinogenic properties that can lead to genetic disorders and gene mutations, as can certain viruses, bacteria and radiation rays.[1,9]

Proto-oncogenes are a group of genes that cause normal cells to become cancerous when they are mutated to oncogenes. Under normal conditions, these genes are responsible for cell division and growth, however, these become expressed at very high levels following their mutation, causing uncontrolled cell division.[10,11] The human genome possesses genes to synthesise more than 30 types of enzymes that can repair DNA damage and prevent rapid cell division, however, these genes are also susceptible to mutation and hence cannot always be recruited to suppress cancer growth.[12]

Epigenetic modifications such as DNA methylation, histone acetylation and nucleosome position all play important roles in cancer formation.[13,14] Removal of a methyl group on a gene, through the process of hypomethylation, primarily occurs in repeated sequences which can lead to deletion of genes as well as chromosomal instability.[15] Hypoacetylation has been observed in a range of cancers including breast, lung, and bladder.[16] The addition of methyl groups to a gene through hypermethylation may also be detrimental to the cell. Often,

hypermethylation occurs in the promoter region, inactivating the transcription of genes involved in repair, cell cycle control and apoptosis. Hypermethylated promoters can however be novel biomarkers for the diagnosis and prognosis of cancer.[17,18]

Histone acetylation is another epigenetic modification associated with cancer if this is not regulated.[19] Histones are proteins that wrap around DNA and provide structural support for chromosomes. The terminal ε-lysine residues of histone proteins can be acetylated or deacetylated, a process regulated by HDAC and HAT enzymes (Figure 1). [20]

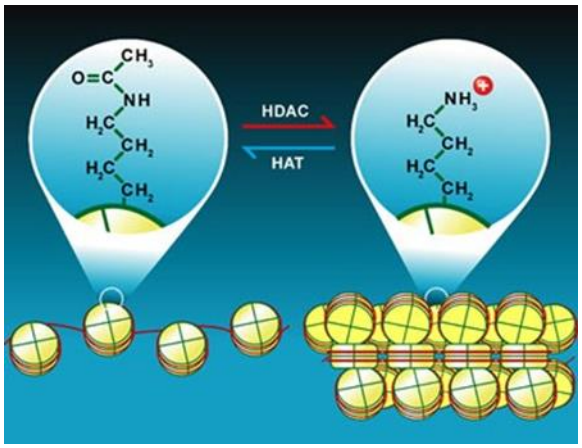

Figure 1: Regulation of terminal ε-lysine residue acetylation/deacetylation by HDAC and HAT enzymes.[21]

Alterations in the acetylation status of histones has been linked to many cancers including colon cancer, lung and leukemia due to the influence these processes have on the access of transcription factors to the gene. For example, removal of an acetyl group increases the charge on the histone protein, causing negatively charged DNA to become wrapped more tightly, preventing the access of vital transcription factors to synthesise proteins essential for controlled cell growth and repair.[22,23] Inhibition of the HDAC enzyme is a key target for the complexes studied in this report. As such, a more detailed summary of the HDAC enzyme is given in **Section 1.4**.

Current cancer research strategies are based on the concept of "targeted" therapies, in which these therapies are drugs or other substances that block the growth and spread of cancer by interfering with specific molecules that are involved in growth, progression, and spread of cancer.[24] Many targeted cancer therapies have been approved by the Food and Drug Administration (FDA) to treat specific types of cancer. Despite the recent progress in regression or control for a wide variety of tumours, some cancers do not respond to current therapeutic therapies, resulting in low survival rates, high recurrence, and frequent relapse and metastases. It is therefore pivotal that the efforts of biologists, chemists, and oncologists are combined to

offer novel therapeutic options for patients and precision medicine is achieved based on the molecular metabolic and (epi)genome signature.[25]

1.1 Platinum – Anticancer agents

In the field of chemotherapeutics, there have been many successful organic molecules used to treat and manage cancers. Metal complexes have also been used in this field, where the metal complex can give significant advantages over organic compounds. The most common metal used in anticancer drugs is platinum.[26] Cisplatin marks a pivotal point in chemotherapeutics since this complex is the very first example of a metal-based agent used to treat cancers.[27] Prior chemotherapeutics were organic compounds, and remained limited to such, due to the understanding that heavy metals, such as platinum, were toxic and thus would be too dangerous for human administration.[28] Cisplatin's discovery has therefore transformed the rationale behind drug design through fusing organic and inorganic chemistry disciplines and has consequently provided a plethora of possibilities for the future of anticancer drug development.

The remarkable success of this cisplatin can be appreciated through the fact that more than 3000 platinum derivatives have been synthesised and tested for their antiproliferative potential against cancer cell lines.[29] However, cisplatin (**1**) is still used in the clinic and is administered alone or in combination with other anticancer drugs, where it is used in the treatment of testicular, ovarian, bladder, oesophageal, colon, gastric, breast, head, neck, melanoma, and prostate cancer.[30] The versatility of this drug has led to extensive scientific investigation to probe its speciation in the blood and the mechanism of its action.

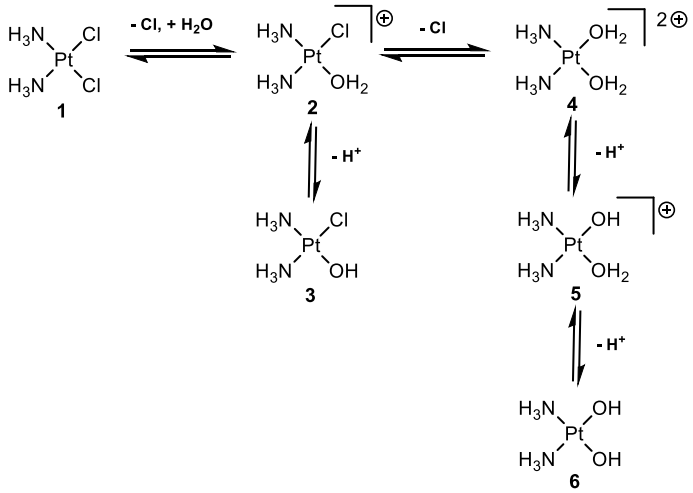

Figure 2: Speciation of cisplatin in aqueous solution as reported by Berners-Price, Ronconi and Sadler.[31]

In an aqueous environment, cisplatin undergoes a ligand exchange reaction in which one chloride ligand is displaced by a water molecule to yield a monoaqua platinum species, **2** (Figure 2). The platinum centre of **2** causes the pK_a of the bound water molecule to drop to 6.41, leading to deprotonation at neutral pH to form monohydroxo species **3**. However, **2** may also undergo a second aquation reaction, giving rise to a diaqua complex, **4**. This second aquation is not favoured in the blood due to the relatively high chloride ion concentration, but in the cytoplasm of the cell, the chloride ion concentration is approximately 95% lower, thus the equilibria is heavily shifted to the right and favours formation of **4** under these conditions. It should also be noted that deprotonation of the diaqua complex is possible due to the drop in pK_a associated with being bound to the Pt^{2+} ion, where each water molecule can lose a proton to yield monohydroxo monoaqua and dihydroxo species **5** and **6**, respectively. It is suggested from these speciation studies that complex **2** and **3** are the major forms found in the blood, but once the drug has entered the cell and exists in the cytoplasm, complexes **4**, **5** and **6** dominate if sufficient time is allotted for the equilibria to shift.[32–35]

1.1.1 Cisplatin mechanism of action

The findings of the aqueous solution chemistry of cisplatin (**1**) provided a strong foundation to determine the mechanism of action of cisplatin. The cellular effects of cisplatin are described by a mechanism comprising of four key steps: (i) cellular uptake, (ii) activation, (iii) formation of DNA adducts and (iv) cellular response.[36]

i) Cellular uptake of cisplatin

Primary investigations of cisplatin uptake demonstrated absorption of cisplatin along a concentration gradient via passive diffusion. These observations were reported after subjecting a cell culture to cisplatin, where the amount of platinum absorbed by cells at a given period of time was measured as a function of the total concentration of cisplatin in the culture medium.[37] The results show that the uptake was proportional to the total platinum concentration in the medium, where saturation did not occur until > 3 mM. It was therefore concluded that cisplatin uptake was not saturable in a metabolic environment and the drug enters the cells via passive diffusion.[38] Such uptake mechanism suggests that dichloro complex **1** and monohydroxo complex **3** are the active species since these are neutral and thus most likely to pass through the highly non-polar phospholipid membrane. This observation does not rule out charged complexes in the toxicity of the drug, since inside the cell the chloride ion concentration drops leading an equilibria shift.[31,39]

Although passive diffusion has shown to be the primary route of cisplatin uptake, an active transport mechanism, which occurs against a concentration gradient using adenosine triphosphate (ATP) as an energy source, has been shown to occur. Active transport utilises proteins embedded in the cellular membrane to allow diffusion of molecules across the phospholipid bilayer. Organic cation transporters, such as OCT1 and OCT2, are examples of such proteins that exist in the membrane and use an active transport mechanism to transfer a wide variety of cationic compounds such as neurotransmitters, coenzymes and drugs across the cell membrane.[28,31] These organic cation transporters offer a potential method of absorption for the charged cisplatin species in Figure 2. The work by Burger *et al.* demonstrated that organic cation transporters transport cisplatin into human embryonic kidney 293 cells and other cell lines.[40] Organic anion transporters are also present in the membrane, thus it has been suggested that negatively charged species of cisplatin, such as $[Pt(Cl)(CO_3)(NH_3)_2]^-$ and $[Pt(Cl)(PO_4)(NH_3)_2]^-$, which may form in the blood due to the presence of carbonate and phosphate anions, may also pass into the cell.[31]

Numerous publications also suggest a role of facilitated diffusion to explain the uptake of cisplatin by cancer cells. One protein that has been proposed to transport cisplatin via this mechanism is a copper transporter named CTR1.[41] The biochemical mechanism of copper movement through CTR1 remains unclear but a limited explanation of how CTR1 functions is by considering binding of copper through an extracellular domain of the protein which is rich in histidine and methionine residues, and act as excellent ligands to copper.[42] Upon binding, a conformational change occurs in the cytoplasmic region of the protein, consequently releasing copper into the cell.[43] Various studies have suggested that both platinum and copper entry the cell via the CTR1 protein, but this seems unlikely owing to the redox activity of copper and relative inert nature of platinum.[44,45,46]

In summary, cisplatin primarily enters the cell via passive diffusion, but active transport is also prevalent through the utilisation of organic cationic transporters in the cell membrane. Other proteins, such as CTR1, have been stated to bind cisplatin and offer a possibility for facilitated diffusion, but the evidence here is conflicting and thus is an unlikely candidate to be vital in the drugs uptake.

ii) Activation, formation of DNA adducts & cellular response

Shortly after the discovery of cisplatin's anticancer properties, it was suggested by various studies that cisplatin's cellular target is DNA, where its interaction with DNA gives rise to its

cytotoxicity.[47] Detailed studies by Fichtinger-Schepman, Reedijk and colleagues showed the presence of an adduct of cisplatin bound to DNA, consisting of *cis*-$[Pt(NH_3)_2]^{2+}$ (**7**) bound to two purine bases of DNA on the same strand, forming 1,2-intrastrand and 1,3-intrastrand crosslinks (Figure 3).[31] The purine bases, adenine and guanine, are both able to form complexes with cisplatin in a 1,2-intrastrand fashion, but only guanine has been reported to form 1,3-intrastand complexes. Interestingly, adducts whereby both purine bases are guanine, i.e. *cis*-$[Pt(NH_3)_2]$-GG (**8**), are far more common than *cis*-$[Pt(NH_3)_2]$-AG (**9**) and *cis*-$[Pt(NH_3)_2]$-AA (**10**) derivatives (Figure 3).[48]

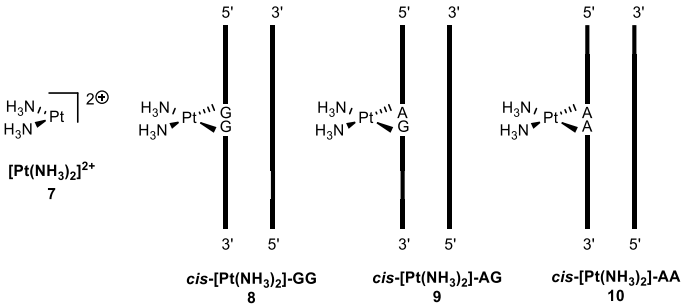

Figure 3: 1,2-instrastrand crosslinks consisting of cis-$[Pt(NH_3)_2]^{2+}$ (**7**) *to form cis-*$[Pt(NH_3)_2]$*-GG (**8**), cis-*$[Pt(NH_3)_2]$*-AG (**9**) and cis-*$[Pt(NH_3)_2]$*-AA (**10**) derivatives.*

The reactant preference of guanine in platination is complicated owing to the chemical similarity of the N7 binding sites in guanine and adenine. Computational studies by Lippard and co-workers suggested that the carbonyl functionality at the C6 position of guanine forms a strong hydrogen bond with the ammine ligand on platinum, and is crucial in stabilising the Pt-guanine adduct transition state relative to the Pt-adenine adduct, making its formation more favourable (Figure 4). The presence of a hydrogen-bond donor at the ligand bound to platinum suggests a ~50% kinetic preference for guanine platination. It was also shown that for the corresponding Pt-adenine adduct, where the ammine could act as a hydrogen-bond donor, is in fact energetically unfavourable, thus the Pt-adenine adduct receives no such transition state stabilisation.[49]

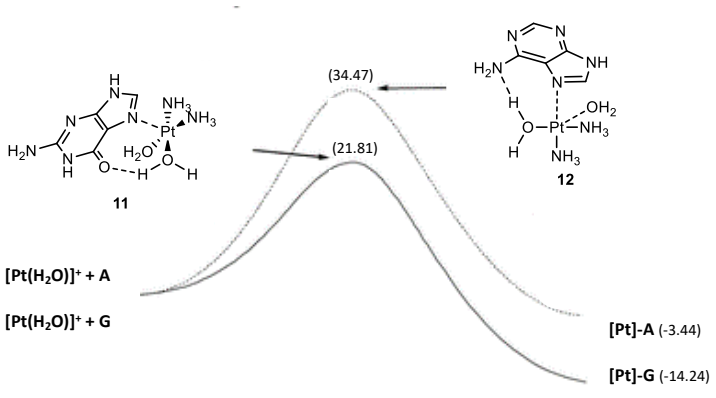

Figure 4: Energy profile diagram from computational studies to elucidate the preference of cisplatin coordination to guanine.[49]

The cis-[Pt(NH_3)$_2$]-GG (**8**) adduct comprises ~65% of the total products of cisplatin's interaction with DNA. The mechanism for the formation of the major adduct has been subject to extensive investigation, with nuclear magnetic resonance (NMR) studies conducted by Davies et al. providing the most insightful findings into the reaction mechanism. In these series of experiments, a short segment of a palindromic DNA duplex was subjected to isotopically labelled cisplatin, cis-[Pt($^{15}NH_3$)$_2$], and the interactions monitored via ^{1}H-^{15}N heteronuclear single quantum correlation (HMQC) NMR spectroscopy. The experiment provided a means of detecting the platinum species discussed in Figure 2 and the rates at which they changed with time in the presence of the DNA duplex. From these studies it was evident that the monoaquated complex, **2**, was largely responsible for the binding of cisplatin to DNA and the diaquated species, **4**, shown to make only a minor contribution. The minor contribution of **4** is due to its slow formation and hence low concentration, since in this time, the monoaquated complex is well underway in its reaction with DNA.[50] The mechanism for the formation of 1,2-instrastrand crosslinks, determined from these NMR spectroscopic studies, is summarised in Figure 5.

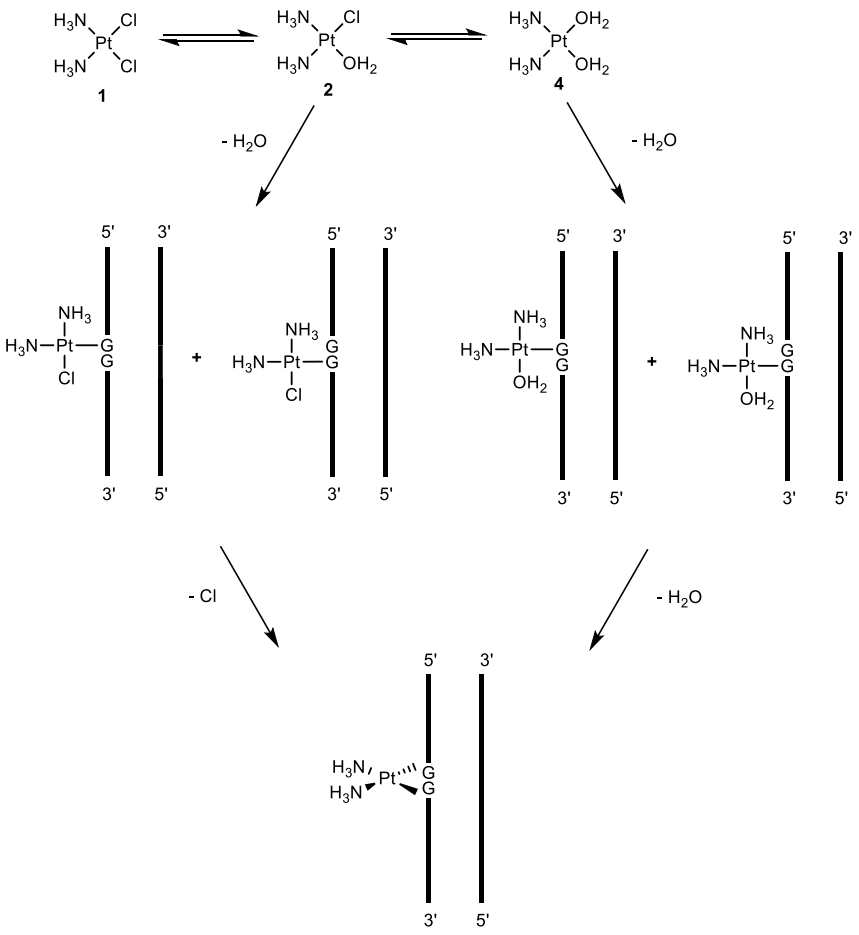

Figure 5: Mechanism of the reaction of cisplatin with DNA to form a 1,2-intrastrand crosslink at the GG site of the DNA duplex as elucidated through ^{1}H-^{15}N HSQC NMR Spectroscopy.

The significant distortion in the DNA double helix caused by these intrastrand crosslinks results in apoptotic cell death. Typically, the DNA lesion is recognized by cellular machinery that either repairs the lesion, bypasses it, or initiates apoptosis. The inhibition of cellular transcription is the most significant mechanism by which apoptosis occurs, since when RNA polymerases transcribe DNA, the enzyme stalls at the platinum cross-link and recruits transcription-coupled repair machinery. If this machinery is unable to repair the lesion, then the cell evokes a programmed cell death pathway.[28]

1.1.2 Cisplatin resistance

Unfortunately, cisplatin does have a huge drawback, which is cellular resistance.[46] Repeated exposure to cisplatin through therapy can lead to the cancer becoming resistant to it – rendering the therapy ineffective. It would be expected that simply raising the concentration of cisplatin administered could overcome these effects, however, the drug's narrow therapeutic window

results in high risk of toxicity to the patient.[37] The resistance is thought to arise through the cell efficiently blocking cisplatin from passing through the phospholipid bilayer, however, since passive diffusion is largely responsible for its transport, it is more probable that cisplatin undergoes chemical modification in the cytoplasm and is exported back out of the cell.[51] Cisplatin that has managed to reach the DNA and form 1,2-intrastrand crosslinks may also be removed through the various DNA repair mechanisms and hence no longer leads to apoptosis of the target cells.[52,53]

1.1.3 Cisplatin analogues

In an attempt to overcome cisplatin side effects and resistance, alternative platinum drugs have been developed. Alongside cisplatin, there are another five platinum drugs that are approved in cancer treatment (Figure 6), where carboplatin (**13**) and oxaliplatin (**14**) are approved by Food and Drug Administration (FDA) and used worldwide, whereas, nedaplatin (**15**), heptaplatin (**16**), and lobaplatin (**17**) are also approved in Japan, Korea and China, respectively.[29,36]

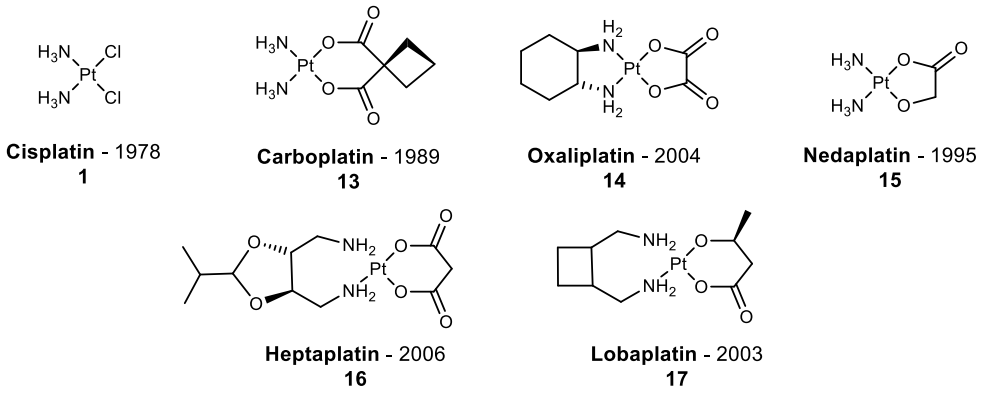

Figure 6: Six clinically approved platinum therapeutic drugs with their year of marketing approval. [29,36]

All of the approved platinum complexes share a common molecular framework, whereby the platinum centre is bound to two cis amine and two cis anionic ligands, leading to a neutral and square-planar complex.[54,55] The amine ligands can be non-chelating, as seen in oxaliplatin, lobaplatin and heptaplatin, or chelating, exhibited in cisplatin , carboplatin and nedaplatin, but for all examples, these amine ligands remain bound to the platinum(II) centre throughout course of its biological action. As a result, this mutual framework means that cisplatin and its analogues follow the same general mechanism of action, thus not overcoming the hurdle of cellular resistance.

1.2 Ruthenium – Anticancer agents

Despite the remarkable success of platinum chemotherapeutics, the main drawback is the associated multiple drug resistance whilst administering these complexes as cancer remedies. Ruthenium complexes are recognised as promising alternatives to platinum complexes due to their differing mechanisms of action, avoiding these platinum resistant pathways.[56] Ruthenium has a number of properties that are desirable for anticancer applications, such as: i) multiple physiological accessible oxidation states (Ru(II), Ru(III) and Ru(IV)) - an advantage in the reducing environment of cancer tissues; ii) multiple coordination sites where ligands can be designed to modulate activity; iii) similar ligand substitution kinetics in aqueous media to platinum(II) complexes and iv) selectivity to cancer targets due to preferential uptake by tumour cells.[57–59] Considering the above, it is no surprise that ruthenium complexes show considerable promise for the treatment of cancers. Ruthenium agents can operate in varying methods, where some directly attack and kill the tumour, whereas others prevent its metastatic growth.[59,60] Numerous ruthenium complexes have been synthesised, with their anticancer properties interrogated, and Figure 7 shows some key examples of these.

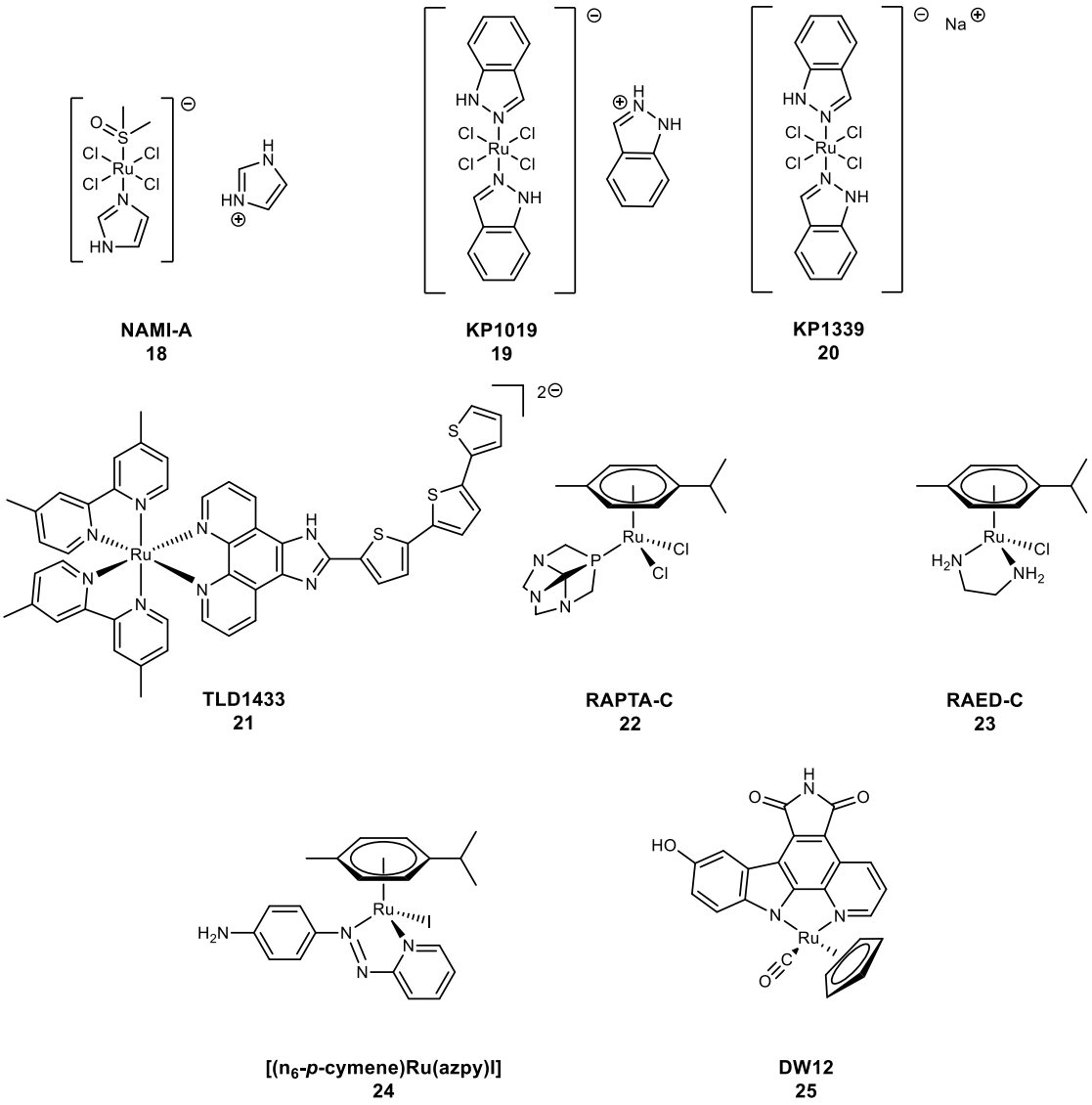

Figure 7: Examples of some of the therapeutic ruthenium complexes discussed.

A few ruthenium complexes have reached clinical trials, where some have been based on ruthenium(III) metal centres such as, NAMI-A (**18**), KP1019 (**19**) and NKP-1339/KP1339 (**20**), but also ruthenium(II) centres, including TLD1433 (**21**), RAPTA-C (**22**) and RAED-C (**23**).[58,61] NAMI-A, KP1019, NKP-1339 and KP1339 reveal their therapeutic properties in a similar manner to platinum(II) compounds, whereby these compounds exhibit their biological effects by losing one or more of their bound ligands and reacting with target molecules in the cell such as DNA and proteins. Both NAMI-A and KP1019 are examples of prodrugs, which are activated upon reduction of the ruthenium(III) centre to ruthenium(II) in the reducing environment of the tumour.[62] These two drugs do not exhibit the same effect on tumour cells, since NAMI-A reduces metastases and hence prevents the spread of secondary tumours, whereas KP1019 is a cytotoxic compound effective against primary tumours only.[63,64] Unfortunately, neither of these

complexes progressed further than Phase II in clinical trials due to poor efficacy and low solubility for NAMI-A and KP1019 complexes, respectively.[62,65]

The redox activity of these ruthenium(III) complexes has resulted in considerable interest in ruthenium(II) drug candidates. Of particular interest are ruthenium(II) half-sandwich complexes that possess a capping arene group. These exciting class of arene compounds have very broad scope and complexes such as RAED-C (**23**) ([Ru(η^6-arene)(dien)]Cl (dien = ethylenediamine)) and RAPTA-C (**22**) ([Ru(η^6-arene)PTA]Cl_2 (PTA = 1,3,5-triaza-7-phosphoadamantene)), remain the most promising.[66–68] Recently, the RAPTA-C complex has been shown to reduce the growth of primary tumours for ovarian and colorectal carcinomas, in which RAPTA-C binds selectively to the histone proteins of chromatin to exhibit its tumour inhibitive properties.[69] This differs slightly to [Ru(η^6-arene)(dien)]Cl type complexes, where the dien ligand is exploited through hydrogen bonding with DNA, offering a similar function to the ammonia ligands in cisplatin.[70]

Owing to the ruthenium(II) metal centre, some compounds are relatively exchange-inert which leads to exhibition of their biological effects via 'nontraditional' mechanisms (i.e. they do not bind to DNA), contrasting the complexes previously discussed. For example, [(η^6-*p*-cymene)Ru(azpy)I], appears to cause cell death by generating reactive oxygen species (ROS) through a catalytic mechanism involving its attached ligands and glutathione (an endogenous component of cellular metabolism).[71] Another compound, DW12 (**25**), expresses its anticancer properties by mimicking the shape of staurosporine (**26**), a natural product that induces apoptotic cell death, which in turn stimulates the production of the cancer-protect proteins (Figure 8).[72]

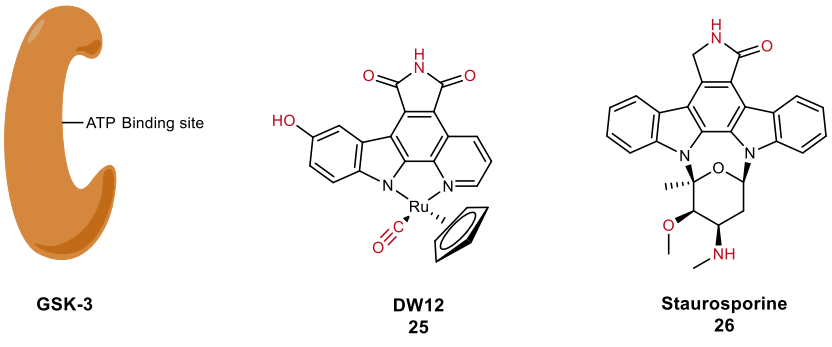

Figure 8: Illustration of how DW12 mimics staurosporine to interact with the adenosine triphosphate (ATP) binding site of Glycogen Synthase Kinase-3 (GSK-3) to induce apoptotic cell death. In DW12, the NH group of the maleimide moiety forms a hydrogen bond with the amide carbonyl of Asp133 in the ATP binding site of GSK-3, one carbonyl group of the maleimide moiety interacts with the NH group of Val135, and the second carbonyl of the same moiety forms a water-mediated hydrogen bond with Asp200. The indole OH group interacts with the carbonyl amide group of Val135. The CO ligand is able to undergo an unusual

interaction mode with the glycine-rich loop of the ATP binding site to optimise binding, rendering DW12 a more potent inhibitor for GSK-3 than staurosporine.[72]

It is clear that the structures and properties of ruthenium anticancer agents are vast. These complexes operate in a number of ways, with the complex either losing its ligands through direct interaction with biological targets, generating reactive oxygen species to chemically modify biological molecules in the cell, or even by acting as shape-specific inhibitors of enzymes that are important for the survival of the cell. These complexes have largely unexploited potential since the ligand combination and coordination geometry between ruthenium and its ligands, exhibit huge effect of the activity of ruthenium compounds through influencing the reactivity, hydrophobicity, binding, cellular uptake and intracellular distribution of the drug candidate.[73]

1.3 Copper – Anticancer agents

Another alternative to platinum-based drug compounds are copper complexes.[74] Copper is an endogenous metal ion, having a huge advantage over platinum and ruthenium since using ions already well tolerated by the body may lead to less systemic toxicity and a larger therapeutic window.[27] Copper is an essential micronutrient in humans, where it is a cofactor of many enzymes involved in processes such as biosynthesis of neuroendocrine peptides and neurotransmitters, detoxification of free radicals, and formation of connective tissues and blood vessels.[75] It is no surprise that the antitumour properties of copper have been extensively studied with such a ubiquitous biological role. Another significant advantage of copper-based therapeutics is their enhanced uptake by cells because of the numerous copper efflux proteins that exist in the cell membrane. Such efflux proteins have been reported to play important roles in the uptake of cisplatin in tumour cells, therefore, copper-based therapeutics offer great pharmacodynamic potential.[43]

Copper(II) complexes can adopt different geometries depending on the types of ligands around the metal centre. For example, copper(II) tetrachloride and copper(II) chloride dihydrate exist as a tetrachlorocuprate and an octahedral complex with Jahn-teller distortion, respectively (Figure 9).

Figure 9: Tetrahedral and distorted octahedral structures of copper(II) tetrachloride and copper(II) chloride dihydrate, respectively.

However, for most copper(II) complexes, there is a strong preference to adopt a square planar geometry owing to copper(II) having a d^9 electronic configuration. Figure 10 shows that once these 9 d-electrons are populated into the energy levels for different geometries, the square-planar field is a considerably lower energy geometry, compared to octahedral or tetrahedral.

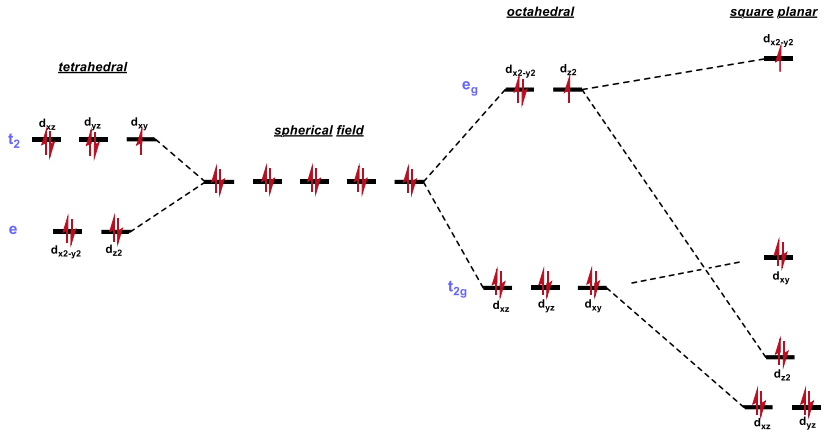

Figure 10: Common geometries adopted by d^9 copper(II) complexes and their relative stabilities.

Copper complexes are analogous to any such metal ion coordinated by ligands, in the fact that the properties of the complex can be tuned via the ligand design, where these ligands themselves may possess antiproliferative activity.[43] Copper tends to be coordinated through nitrogen, sulphur and oxygen donor atoms on the ligands, which are often anionic to neutralise the electrical charge of copper and enable transport through the cell membrane.[76,77] Chemotherapeutic copper complexes demonstrate their effects through numerous pathways, which involve one, or a combination of the following: i) DNA intercalation, ii) DNA aggregation, iii) ROS generation, iv) topoisomerase inhibition and/or v) proteosome inhibition.[78–82] In the biological environment, copper can exist as copper(II) or copper(I) . This redox activity changes the preferred geometry and potentially the activity of the complexes. Copper(I) complexes are d10 and therefore have no crystal field stabilisation energy. As a result, geometry is based on sterics, where tetrahedral or octahedral geometries are observed. The reversibility of the copper(I)/copper(II) redox process is known to affect the anticancer activity of certain

complexes, where reactive oxygen species ae generated in the presence of copper. These ROS ultimately lead to apoptosis.[74]

Figure 11 shows some of the copper(II) complexes that have shown promise in their therapeutic properties. For example, the copper(II) cyclen complex functionalised with three (2-anthraquinonyl)methyl substituents (**29**) reported by Horman *et al.* have shown high toxicity via DNA/RNA synthesis inhibition and aggregation phenomena.[79] The copper(II) phenanthroline complex (**51**), synthesised by Sigman *et al.*, operates as a DNA chemical nuclease upon its intercalation to the DNA backbone.[83] An exciting group of copper(II) complexes centred around a [Cu(phen/bipy)(nitrogen/oxygen-oxygen/nitrogen donor)] type framework are stated to induce cell death through ROS generation.[80]

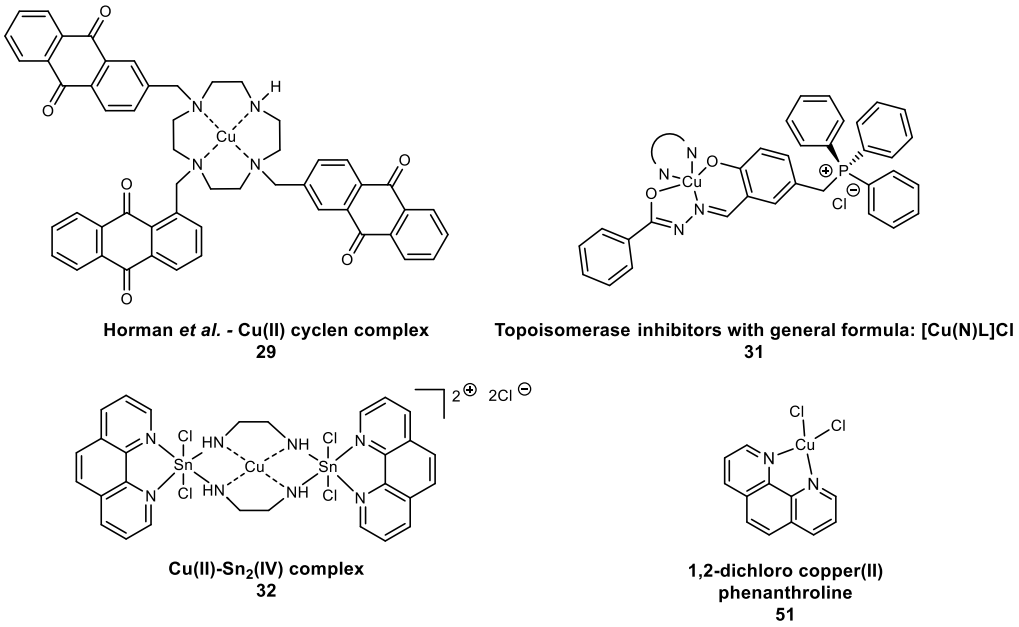

Figure 11: Examples of some of the therapeutic Cu(II) complexes discussed with ranging cellular mechanisms.

A rising class of copper-based therapeutics are topoisomerase inhibitors. Topoisomerase enzymes are essential in DNA replication and protein transcription since these enzymes relax the supercoiling at the replication fork to enable access of enzymes crucial for such processes. Therefore, inhibition of these enzymes will cease DNA replication, protein production and ultimately lead to cell death.[84] A small group of topoisomerase inhibitors, with general formula [Cu(N)L]Cl (N = phen, bipy or 5,5'-dimethyl-2,2'-bipyridine; L = doubly 5-triphenylphosphonium-methyl)-salicylaldehyde deprotonated hyde-benzoyl hydrazone) (**31**), have shown excellent cytotoxic activity against lung and prostate cancer cell lines (Figure 11).[81] Bimetallic complexes of topoisomerase inhibitors have also been reported with potent effects to breast cancer cell

lines in particular. The heterobimetallic Cu(II)-Sn_2(IV) complex (**32**) is not only interesting in its design, but shows a broad scope of activity, with promising results against breast, cervix, kidney, colon, lung and pancreatic cell-lines. This compound operates via the planar phenanthroline heterocyclic ring approaching the topoisomerase–DNA complex and forming a complex itself with the topoisomerase enzyme – ceasing its activity.[85]

Despite the vast range of activities and modes of action displayed by copper complexes, a significant drawback in their application is the poor solubility exhibited in aqueous environments. There has been a focus on developing polymer/nanoparticle analogues of copper agents to improve cellular internalisation and distribution. An intriguing example is a copper species that contains amphiphilic hyperbranched polytriazoles, that have been used as polyprodrugs for copper delivery and label-free cellular bioimaging – offering a theragnostic application toward cancer therapy.[86]

1.4 Histone deacetylase enzyme inhibitors

It is evident that chemotherapeutic drugs based upon platinum, ruthenium and copper exhibit a wide array of activities and hence show differing levels of toxicity towards different cancer cell lines. A novel therapeutic approach for the treatment of cancer and related diseases has recently emerged in developing drugs to target histone deacetylase enzymes (HDACs). Inhibition of HDAC enzymes results in growth arrest, differentiation and apoptosis due to the role these enzymes play in controlling the level of transcription as expressed in Figure 12.[87] Through catalysing the removal of acetyl groups from ε-lysine residues on the N-terminal tail of histone proteins, HDACs can alter chromatin structure and also regulate the pattern of acetylation on non-histone proteins.[88]

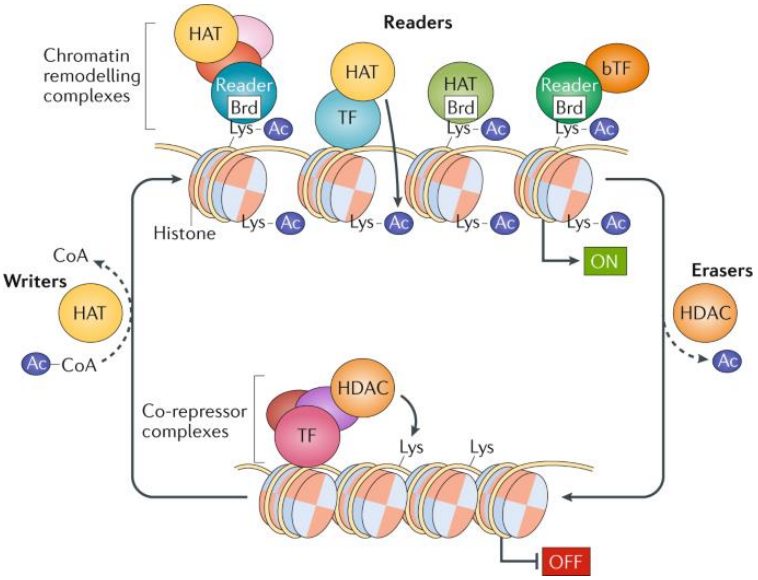

Figure 12: Chromatin-mediated control of gene expression by reversible lysine acetylation catalysed by HAT and HDAC enzymes.[89]

There are 18 HDAC enzymes in the human genome, which are broadly divided into zinc-dependant and nicotinamide adenine dinucleotide (NAD^+)-dependant HDAC enzymes (Table 1). The latter are referred to as sirtuins (class III) and have not been subject to as intensive study as their zinc-dependant relatives.[90] The zinc-dependant subset of the HDAC family are further divided into class I (HDAC1/2/3/8), class IIa (HDAC4/5/7/9), class IIb (HDAC6/10) and class IV (HDAC11).[91–93]

Table 1: Summary of the 18 HDAC enzymes present in the human genome (note: HDAC = histone deacetylase and SIRT = sirtuins).

Group	Class	Name
Zinc-dependant	Class I	HDAC1
		HDAC2
		HDAC3
		HDAC8
	Class IIa	HDAC4
		HDAC5
		HDAC7
		HDAC9
	Class IIb	HDAC6
		HDAC10
	Class IV	HDAC11
NAD^+-dependant	Class III	SIRT (1-7)

There are four FDA clinically approved drugs which target zinc-dependent HDAC enzymes, generally termed as HDAC inhibitors (Figure 13).[94,95]

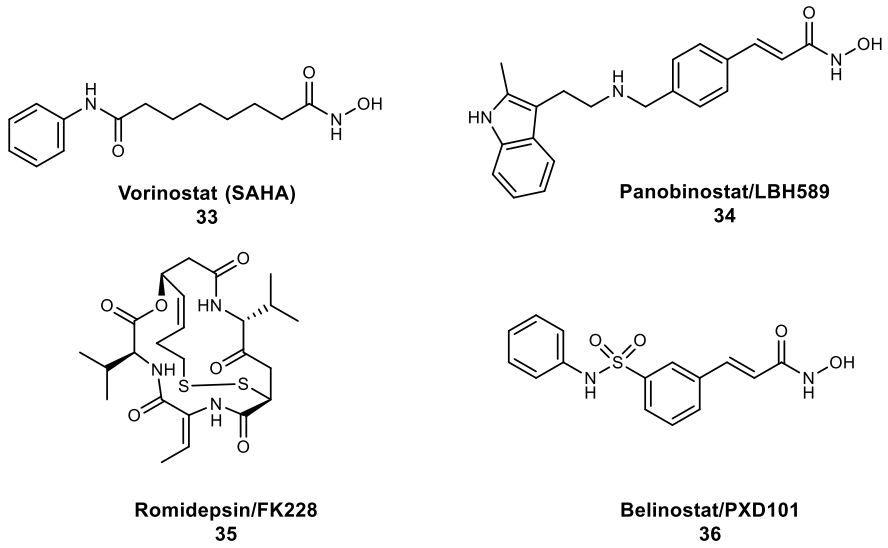

Figure 13: Food & Drug Administration clinically approved HDAC inhibitors: Vorinostat, Panobinostat, Romidepsin and Belinostat.

The four HDAC inhibitors in Figure 13 share a common framework where they adopt a zinc-binding group, linker and capping/head group motif. This common structure is less obvious for romidepsin (**35**), which is in fact a prodrug, whereby the active metabolite has a free thiol group to bind to Zn^{2+} in class I and II HDAC enzymes.[96] These HDAC inhibitors have mostly been applied for haematological cancers, such as cutaneous T-cell lymphoma, peripheral T-cell lymphoma and multiple myeloma, which is rationalised through considering that solid tumours originate from more differentiated cells and hence are less sensitive to epigenetic reprogramming.[97] Despite this, HDAC enzymes have still deservedly received research interest, and since the capping group can be varied without impairing the potency of the inhibitors, the potential of such inhibitors is largely unlocked.[98]

The design of these HDAC inhibitors is not limited to organic variations of the structural motif. A variety of organometallic complexes have been synthesised and tested for their HDAC inhibitory properties, some of which are shown in Figure 14.[99,100]

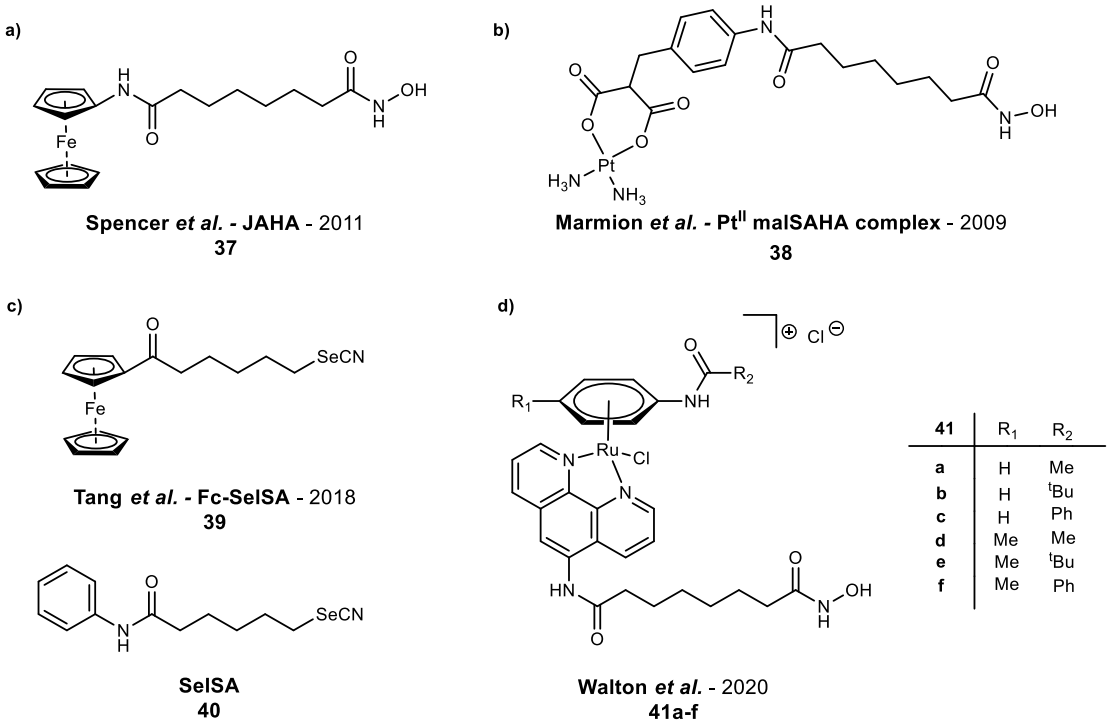

Figure 14: Organometallic analogues of SAHA with their year of discovery. a) contains a ferrocenyl group as a phenyl bioisostere[101]*, b) multifunctional platinum drug candidate with DNA binding, histone deacetylase inhibitory activity*[102]*, c) HDAC inhibitor possessing a selenocyanide (SelSA) zinc-binding motif and ferrocenyl capping group*[100] *and d) piano stool ruthenium(II) HDAC inhibitor library.* [99]

Figure 14 shows that the early examples of metal complex HDAC inhibitors were presented by Marmion *et al.* (Pt-based complexes) and Spencer *et al.* (Fe-based complexes). These complexes showed the potential for HDAC inhibitors in which metal complexes were incorporated, often leading to improved activity. The ferrocene-based HDAC inhibitor, Fc-SelSA, synthesised by Tang *et al.* illustrates clearly the power of targeting HDAC enzymes in oncology treatments. This complex was shown to possess potency to triple-negative breast cancer cells, which is promising owing to the poor efficacy in current treatments available due to the lack of target-directed therapies. Molecular docking studies of Fc-SelSA (**39**), SelSA (**40**) and SAHA (**47**) shows that the ferrocenyl group overlaps with the typical phenyl ring head group, allowing the amido group of Fc-SelSA to form important hydrogen-bonding interactions (Figure 15). These findings indicate that using three-dimensional aryl groups as a cap is an effective strategy for HDAC inhibitor design due to the selective recognition and interaction with protein active sites.[100]

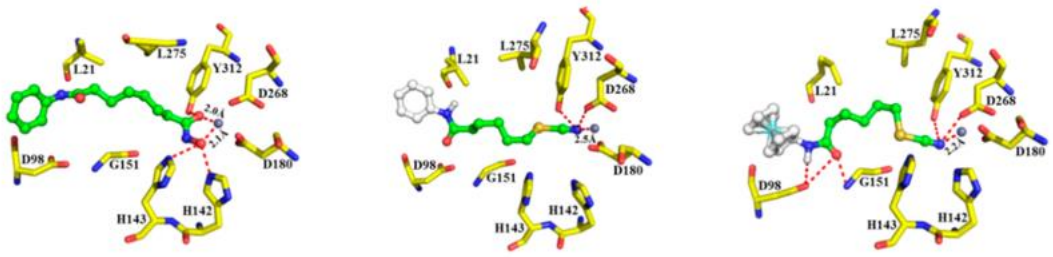

*Figure 15: Docked complexes of SAHA (**47**), SelSA (**40**) and Fc-SelSA (**39**) bound to HDAC. a) Docking poses of SAHA in HDAC that can form hydrogen bonds with residues H142, H143, and Y312; b) Docking poses of SelSA in HDAC that can form hydrogen bonds with residues D268 and Y312 and c) Docking poses of Fc-SelSA in HDAC that can form hydrogen bonds with residues D98, G151, D268, and Y312. (Note: The zinc ion is shown as a gray ball; interactions between the selenocyanide (SeCN) group and zinc are shown as red dashed lines.*[100]

The ability of selective recognition possible using organometallics has also been realised and exploited by Walton *et al.* through the design of piano stool ruthenium complexes that can act as HDAC inhibitors, where variation in the capping arene leads to differences in HDAC isoform selectivity. In this work, six novel ruthenium piano stool HDAC inhibitor complexes were synthesised (Figure 14), and in all cases excellent *in-vitro* anticancer activity was exhibited against the MCF7 human breast adenocarcinoma cell line (Table 2).

Table 2: In-vitro EC_{50} cell anticancer activity and cellular uptake measured against the MCF7 human breast adenocarcinoma cell line.[99]

Compound	EC_{50} / μM	Cellular uptake / %
SAHA	1.5 ± 0.2	-
8a	32 ± 2	0.5
8b	1.4 ± 0.2	18.9
8c	1.7 ± 0.3	13.8
8d	1.2 ± 0.3	13.1
8e	5.1 ± 1.5	6.2
8f	2.1 ± 0.2	11.2

The majority of the ruthenium complexes had an EC_{50} value equalling that of the clinically used inhibitor, SAHA (**47**). As expected, the most potent ruthenium complexes (8b, 8c and 8d) showed the highest cellular uptake (18.9%, 13.8% and 13.1%, respectively). It is clear that variation in the toxicity between the complexes arises from the variation in cellular uptake, although the reason for this variation is not clear.[99]

All six novel complexes were able to inhibit HDAC1 and HDAC6 activity to less than 25% at 1μM inhibitor. Through varying the capping η^6-arene from a phenyl-derived to a tolyl-derived head group, HDAC6 inhibition was increased by a factor of 2.3. It is therefore shown that variation in inhibitory potency arises from variation in the capping arene of the piano stool complex. Surprisingly, it was found that the addition of a transition metal complex does not appear to increase overall potency of the HDAC inhibitor, but the selectivity between isoforms is effected leading to greater potency towards specific isoforms.[99]

1.5 Dual-action histone deacetylase inhibitors

With such potential being realised in the variation of HDAC inhibitor capping groups to elucidate enhanced potency and selectivity of the inhibitor, an emerging area lies in the design of dual-action HDAC inhibitors. The design rationale behind these inhibitors involves reserving the zinc-binding group for HDAC inhibition, but the capping group is a bioactive moiety itself, which leads to a multitargeted cancer agent. Early examples included Marmion's Pt-based inhibitors, which incoporated a cisplatin-like head group, designed to give additional activity in DNA binding.

The studies conducted by Hanif *et al.* exemplify the impact of combining bioactive moieties in an HDAC inhibitor and how this may result in synergistic activity of its components. The design concept of the organometallic HDAC inhibitor presented by Hanif and co-workers (Figure 16) is based on a bioactive Rh^{III} cyclopentadienyl metal centre, that can undergo ligand exchange reactions and form covalent bonds to target donor atoms. A vorinostat-inspired hydroxamic acid as the Zn-binding group and a 2-pyridinecarbothioamide ligand, which has a preference for amino-acid side-chains over DNA. The Rh^{III} complex designed was a potent inhibitor of HDAC6 ($IC_{50} = 5 \pm 1$) over both HDAC1 and HDAC8 ($IC_{50} = 173 \pm 30$ and 29 ± 6, respectively), and was also highly cytotoxic in human cancer cells. Furthermore, experiments in zebrafish showed anti-angiogenic activity of the Rh^{III} complex, which was not seen for the HDAC inhibitor alone, demonstrating the impact of the metal centre on the drugs properties.[103]

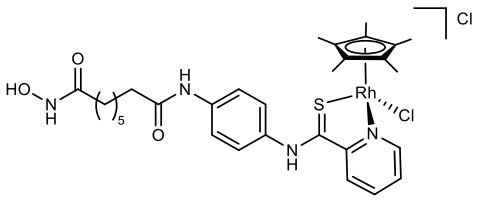

42

Figure 16: Potent multitargeted organorhodium HDAC inhibitor synthesised by Hanif et al.[103]

A multitarget approach that is still in its early stages is the design of HDAC/phospoinositide-3-kinase (PI3K) inhibitors. This arising class of multitarget inhibitors have gathered promising outcomes, where compound Fimepinostat (CUDC-907) (Figure 17) is already in clinical trials.[104] Inhibition of PI3K enzymes is of importance in cancer therapy since this family of lipid kinases play key regulatory roles in many cellular processes including cell survival, proliferation and differentiation.[105] Further studies by Zhang *et al.* have continued to explore the potential of HDAC/PI3K inhibitors, in which two compounds, shown in Figure 17, simultaneously inhibit PI3K and HDAC with nanomolar potencies and favourable antiproliferative activities. Both of these compounds efficiently arrested the cell cycle, and induced apoptosis in certain cancer cell lines. Compound **44** was evaluated further to show significant in vivo anticancer efficacies with tumour growth inhibitions ranging from 45.8%-62.6%, showing the huge promise in the simultaneous targeting of PI3K and HDAC pathways.[106]

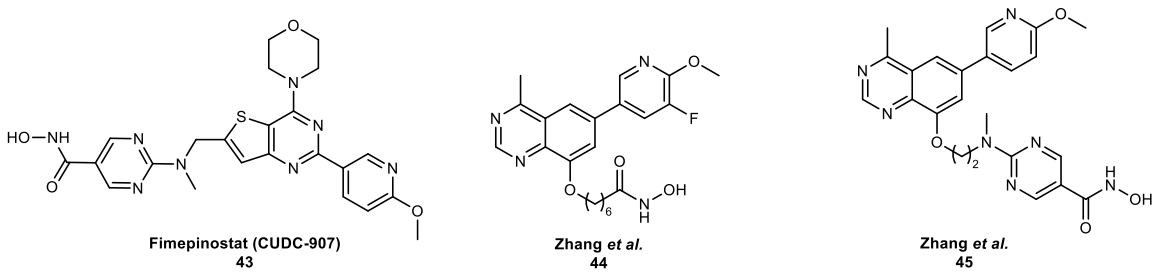

*Figure 17: Dual-action HDAC/PI3K inhibitors including clinically trialled CUDC-907 (**43**) and compounds **44** and **45** synthesised by Zhang et al.* [104, 106]

The therapeutic properties of copper(II) complexes have previously been discussed, however, an approach led my Marmion *et al.* was to combine the DNA binding and nuclease activity of therapeutic copper(II) complexes - namely copper(II)-1,10-phenanthroline, with a known HDAC inhibitor such as SAHA. This design strategy proved remarkable since this would enable oxidative DNA damage as well as HDAC inhibition. Upon entry of the complex into the reducing environment of the tumour cell, the copper(II) ion was expected to be reduced to copper(I) with concomitant release of the HDAC inhibitor.[107,108] Since HDAC inhibition should also render DNA in an "open" chromatin structure, the copper(II)-1,10-phenanthroline core may then have greater access to its DNA target. This innovative approach was even more impressive owing to the protection the copper(II)-1,10-phenathroline core would provide to metabolic hydroxamic acid degradation. Hydroxamic acid degradation occurs through hydrolysis and glucuronidation

which negatively impacts its half-life and pharmacokinetic profile of a hydroxamate-based HDAC inhibitor, hence introduction of copper(II) at this site to protect the hydroxamate functionality, is expected to enhance the inhibitors therapeutic potential.[109,110]

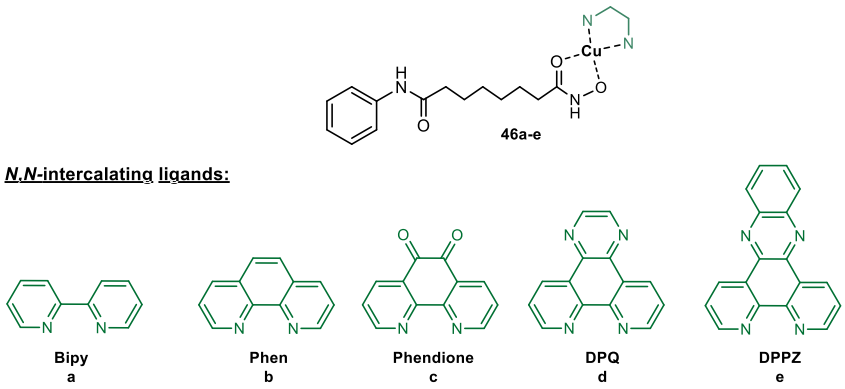

Figure 18: Copper(II) protected hydroxamic acid HDAC inhibitor reported by Marmion et al.[110]

The complexes reported by Marmion *et al.*, shown in Figure 18, exhibited excellent DNA recognition with very high binding affinity for the lead agents Cu-SAHA-DPQ (**46d**) and Cu-SAHA-DPPZ (**46e**). The biophysical studies conducted involving nucleic acid polymers, indicated intercalative binding at both adenine-thymine (A-T) and guanine-cytosine (G-C) rich sequences for CuSAHA complexes containing DPQ, DPPZ, and Phen derivatives. This metallodrug class exerts cytotoxic activity predominantly through an apoptotic pathway, where the complexes mediate DNA damage by producing reactive oxygen species (ROS) as shown through spin trapping experiments that revealed superoxide, the hydroxyl radical, and hydrogen peroxide playing critical roles in strand scission. The agents were also found to have promising antiproliferative effects against a panel of epithelial cancers, and the HDAC inhibition activity was achieved over a shorter time frame as compared to clinical standard, showing the importance of protecting the hydroxamate functionality.[110]

1.6 Project aims

Throughout this literature review it has been realised that organometallic anticancer agents are highly promising, and that enhancing their applications in specific HDAC inhibitor design is largely untapped. Huge potential lies in tuning the selectivity of HDAC inhibitors, and also in their capability of becoming effective multitargeted agents. Therefore, this study has the primary aim of further investigating the properties of copper(II) dual-action HDAC inhibitors and exploring the selective nature of ruthenium-based HDAC inhibitors. The key aims of this project are summarised below:

1. Synthesise, purify and characterise a library of novel dual-action copper(II) HDAC inhibitor complexes.
2. Synthesise, purify and characterise a library of novel ruthenium(II) piano-stool HDAC inhibitor complexes.
3. Perform general HDAC assays to assess the efficacy of the novel inhibitors synthesised.
4. Assess the potency levels of the novel inhibitors synthesised relative to clinically approved SAHA through determination of their minimal concentration needed for 50% inhibition *in-vitro* (IC_{50} value).
5. Perform HDAC assays on specific HDAC isoforms to determine the selectivity profiles of the novel complexes synthesised.

2 | RESULTS & DISCUSSION

The recent rise in the development of dual-action HDAC inhibitors, as discussed in **Section 1.5**, provides solid framework to develop more versatile, potent inhibitors for clinical use. The incorporation of copper(II) into an HDAC inhibitor sparks considerable research interest for the Walton Group due to the roles copper(II) plays in Histone Acetylase Transferase (HAT) upregulation, reactive oxygen species (ROS) generation and its excellent DNA targeting properties.

2.1 Synthesis of copper(II) phenanthroline HDAC inhibitor

2.1.1 Synthesis of dichloro(N^{20}-hydroxy-N^{11}-(1,10-phenanthrolin5-yl)octanediamide)copper(II)

Our investigation began with an aim to synthesise an analogue of suberoylanilide hydroxamic acid (SAHA), whereby the phenyl head group of SAHA would be switched to a copper binding moiety. This in theory would mean that reaction with a copper(II) source would provide a dual-action copper(II) HDAC inhibitor.

The Walton Group has previously reported the synthesis of a SAHA analogue possessing a 1,10-phenathroline head group, where this head group has the capacity to chelate metals through the two nitrogen donors on the phenanthroline aromatic system to form a stable 5-membered ring.[111] The properties of this head group have been exploited for the synthesis of an array of ruthenium(II) based HDAC inhibitors, where such complexes possess promising HDAC activity. Following from the success of these complexes, it was decided to use this 1,10-phenathroline head group as a copper(II) binding moiety in this study, as illustrated in Figure 19.

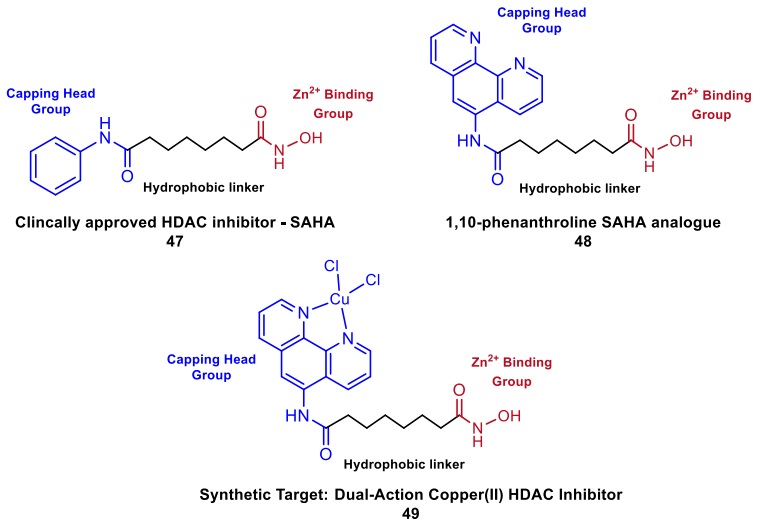

*Figure 19: Clinically approved suberoylanilide hydroxamic acid (SAHA) (**47**), 1,10-phenanthroline SAHA analogue synthesised by the Walton Group (**48**) and copper(II) dual-action HDAC inhibitor target (**49**).*

Dichloro(1,10-phenanthroline)copper(II) (**51**) is a copper(II) complex with similar structure to our synthetic target, with a chelating 1,10-phenanthroline ligand (Scheme 1). This complex can be readily purchased from chemical suppliers and hence demonstrates the suitability of 1,10-phenathroline as a binding group for copper(II). To establish a suitable reaction pathway to form copper(II) phenanthroline complexes, dichloro(1,10-phenanthroline)copper(II) was also synthesised through a reaction of 1,10-phenanthroline and copper(II) chloride dihydrate (Scheme 1).

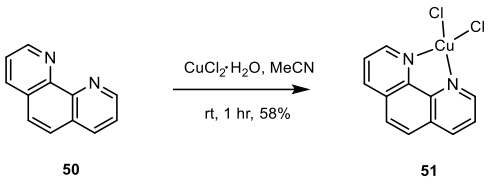

50 **51**

Scheme 1: *Synthetic route for dichloro(1,10-phenathroline)copper(II), 51.*

The reaction product was analysed via electrospray ionisation (ESI) mass spectrometry, where the resulting mass spectrum revealed a molecular ion peak for complex **51** with *m/z* = 423. This peak showed a characteristic copper isotope pattern as a result of copper possessing two stable isotopes, ^{63}Cu and ^{65}Cu, with relative abundances of 69% and 31%, respectively, confirming that this molecular ion peak belongs to a copper containing species. An *m/z* = 423.12 supports a complex where two molecules of 1,10-phenanthroline are bound to the copper centre, with no chloride ligands present. This complex, however, has a doubly positive charge, which is unlikely to form in preference to the neutral 1,10-phenanthroline dichloride complex. An ESI mass spectrum was recorded for a sample of dichloro(1,10-phenanthroline)copper(II) obtained from a chemical supplier as comparison, where this sample also revealed a molecular ion peak *m/z* 423.12. This suggests that the species with *m/z* 423.12 is likely to form in the mass spectrometer, as opposed to being the synthesised molecule, so provides evidence to confirm the synthesis of **51** in the instance that elemental analysis was not available.

Satisfied that 1,10-phenanthroline is a capable ligand of complexing copper(II), and thus is a promising head group to incorporate into our copper(II) HDAC inhibitor, a retrosynthetic analysis of our target molecule, **54**, aided the design of the successful synthetic route (Scheme 2).

Synthetic Scheme:

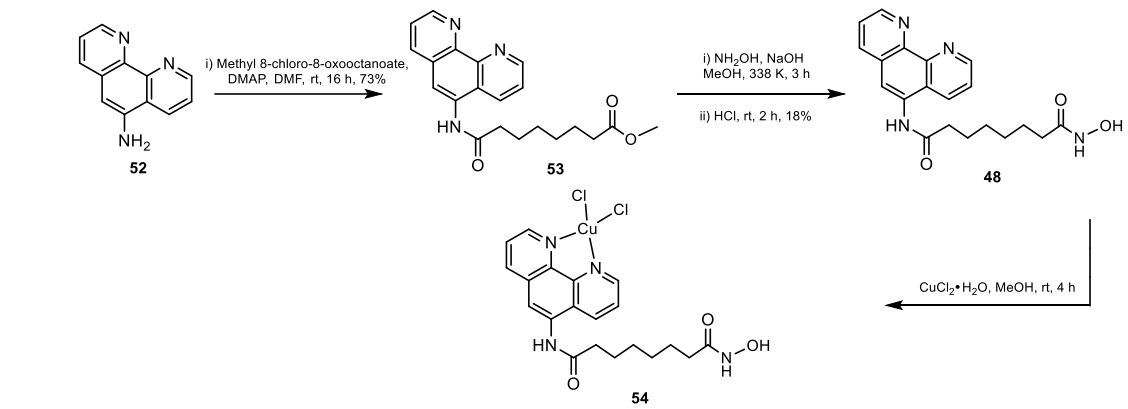

Proposed Mechanism:

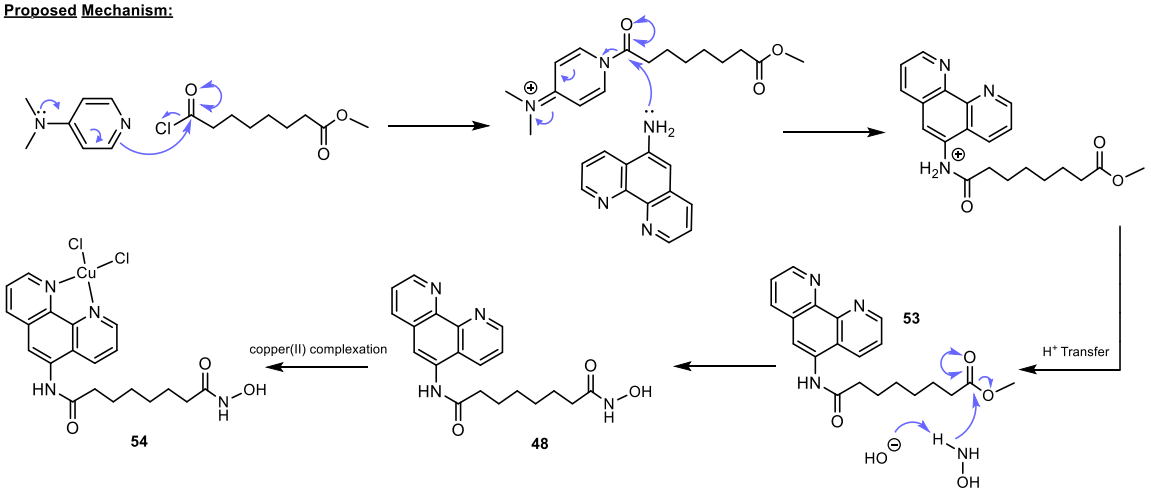

*Scheme 2: Successful synthetic route for target **54** (top) and mechanism of formation of **54** (bottom).*

Starting from 1,10-phenathrolin-5-amine, the head group was attached to the hydrophobic linker through an acyl substitution reaction with methyl 8-chloro-8-oxooctanoate, in which 1,10-phenanthroline-5-amine acts as a nucleophile to attack the δ+ carbon atom of the acyl chloride to form a stable amide bond. It would be expected that the leaving group is the chloride ligand upon nucleophilic attack, however, the addition of a 4-dimethylaminopyridine (DMAP) catalyst results in formation of a highly activated acyl pyridinium ion intermediate prior, that is then subsequently displaced by 1,10-phenanthroline-5-amine to yield **53**. Installation of the hydroxamic acid in **48** proceeds through a simple based-catalysed nucleophilic substitution reaction whereby hydroxylamine (NH_2OH) attacks the carbonyl group of the methyl ester to eliminate methanol. In the solution state, **48** is seen to adopt a very intriguing conformation as revealed via Nuclear Overhauser Effect Spectroscopy (NOESY). The NOESY spectrum (Figure 20) reveals that the amide proton of **48** at δ 10.10 (H^a) shows an nOe to both of the hydroxamic acid protons at δ 10.35 and δ 8.67 (H^c and H^b, respectively). This is unexpected since the alkyl linker is not conformationally restricted, and hence no nuclear Overhauser effect (nOe) would be

expected between these sets of protons in the molecule. To be visible in a NOESY experiment, it is plausible that a hydrogen bond exists between the oxygen atom of the hydroxamic acid carbonyl group and the hydrogen of the secondary amide. This would form a 10-membered ring, infrequently encountered in chemistry, however, there are known reactions that occur through a 10-membered ring transition state. It was attempted to crystallise the compound for analysis via X-ray crystallography to see if this conformation is preserved in the solid state, but attempts to obtain crystals suitable for crystallography of the compound were unfortunately unsuccessful.

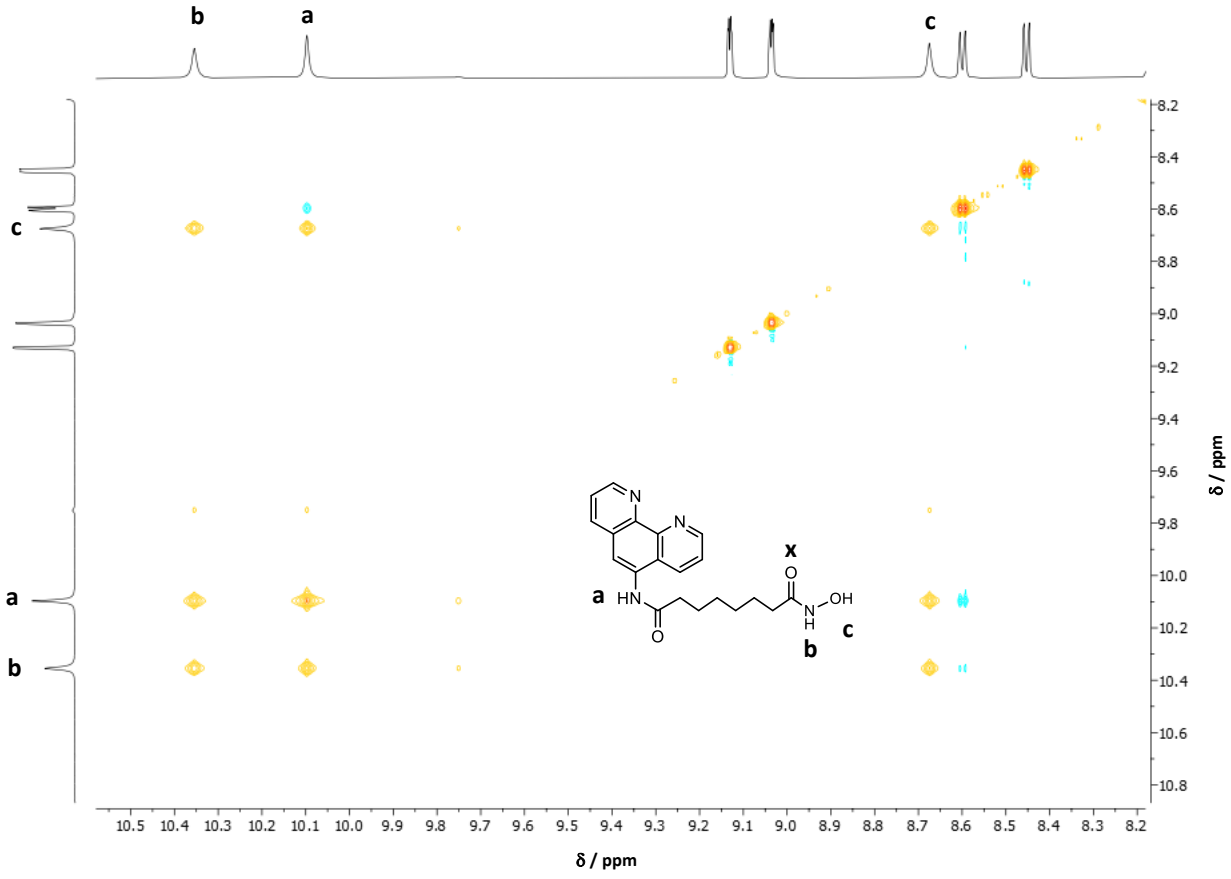

*Figure 20: Aromatic region in the NOESY NMR spectrum of 53, revealing a restricted conformation for the alkyl linker in the solution state due to a hydrogen bonding interaction between **a** and **x**.*

Focussing back to Scheme 2, it was expected that our target **54** could potentially be problematic in its synthesis due to competition between the 1,10-phenanthroline head group and hydroxamic acid zinc(II) binding group. Hydroxamic acids, termed hydroxamates upon ionisation, are capable of chelating to a wide variety of metals such as iron, zinc and copper. Owing to the remarked similarity of hydroxamate and 1,10-phenanthroline binding modes, it

was predicted that these ligands could compete for the copper(II) source, where it may be necessary to leave the hydroxamic acid protected as the methyl ester, **53**, for reaction with copper(II) chloride dihydrate and later install the hydroxamic acid (Figure 21).

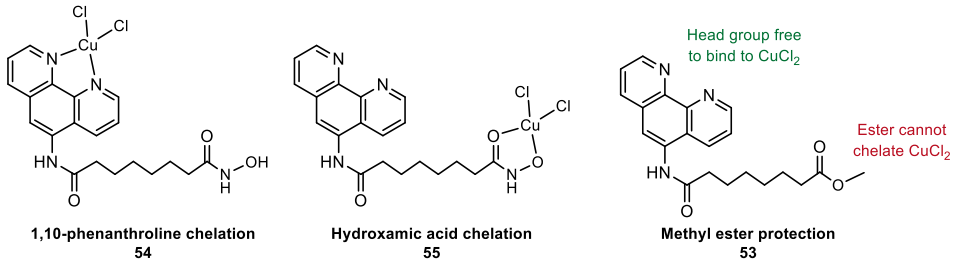

*Figure 21: Chelating mode of the 1,10-phenanthroline head group (**54**); chelating mode of hydroxamate zinc(II) binding group (**55**) and potential method of overcoming binding group competition (**53**).*

Initial attempts to synthesise **54** began with 30 mg of **48** charged with equal equivalents of copper(II) chloride dihydrate in methanol or water solvents at room temperature. The reaction mixture appeared as a suspension in both solvents due to the poor solubility of **48**, and analysis of the reaction mixture via ESI mass spectrometry revealed no peak for the product **54**, or other copper containing species. Removal of the solvent *in vacuo* resulted in a dark green solid which was analysed via Atmospheric Solids Analysis Probe (ASAP) mass spectrometry, a technique in which vaporization of the solid occurs once exposed to a hot nitrogen desolvation gas, where only evidence of free ligand **48** was provided.

A range of experiments at different temperatures were conducted on a 30 mg scale in 1:1 equivalence of **48** and copper(II) chloride dihydrate in both methanol and water solvents at 298 K, 303 K, 313 K, 323 K, 333 K and 343 K in an attempt to improve the solubility of **48** in the reaction mixture and explore if an activation energy barrier was preventing complexation to copper(II). All of the above reactions were analysed via ESI and ASAP mass spectrometry and still showed no evidence of our target **54**. However, the lack of a peak for **54** is not indicative of the lack of the target in solution as this is a neutral complex, and only charged ions are detected in ESI.

Having synthesised **51**, and reports of copper(II) complexes complexed through hydroxamate ligands in the literature, it was confusing that the mass spectrometric data revealed no evidence of copper containing species at all. Although the pK_a of ligand **48** was unknown, 1,10-phenanthroline has a $pK_a \approx 4.27$ at 293 K in water, thus the 1,10-phenanthroline nitrogen atoms in **48** are highly unlikely to be protonated under the reaction conditions and hence remain available to coordinate to copper(II). Hydroxamates typically have a $pK_a \approx$ 7-10 in water, so the speciation of the hydroxamic acid less clear. Despite the ^{1}H NMR spectrum of **48** demonstrating

that the hydroxamic acid is protonated in a DMSO, the pK_a value is dependent on the type of solvent and thus the ^1H NMR data does not provide insight into the speciation at these reaction conditions. To see if **48** would complex copper(II) through the hydroxamic acid, 30 mg of **48** was reacted with copper(II) chloride dihydrate as described above, with an additional equivalent of base to ensure the functional group existed as a hydroxamate - still no complex was observed. It was later decided to alter the equivalents of copper(II) chloride dihydrate in attempt to synthesise **54**, where 0.25 and 0.5 equivalents of copper(II) chloride dihydrate revealed a base peak in the mass spectrum at *m/z* 428.36 with the characteristic copper isotope pattern after removal of the solvent *in vacuo*. Accurate mass of this peak supported the successful synthesis of **54** due to the responsible mass spectrometric species shown in Figure 22.

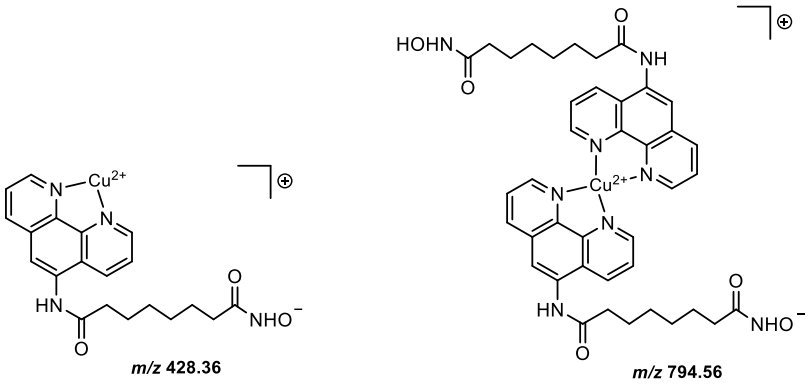

*Figure 22: Mass spectrometric species with m/z 428.36 and m/z 794.56 supporting the successful synthesis of complex **54**.*

Also, in the ESI mass spectrum, a very weak molecular ion peak was present at *m/z* 794.56 which supports two molecules of **48** binding the copper(II) centre, similar to that seen for dichloro(1,10-phenanthroline)copper(II) (**51**). The entire coordination environment of copper(II) is still unknown due to the fragmentation upon ionisation of the sample in the ESI and ASAP experiments. Elemental analysis of the sample offers a simple solution to this problem where we are still awaiting this data. Furthermore, it is still not clear as to whether the copper(II) is coordinated via the phenanthroline or hydroxamate ligand, hence the NMR studies described below confirm the binding mode desired for **54**.

2.1.2 Chemoselective ligand coordination

The competition between the 1,10-phenanthroline head group and hydroxamic acid zinc(II) binding group cannot be interrogated via mass spectrometry so other techniques must be used to probe the ligand chemoselectivity. X-ray crystallography offers the most plausible method to

probe the structure of **54**, however, our attempts to grow crystals of the complex did not produce diffraction patterns suitable for analysis.

A key issue in the study of copper(II) complexes is the $3d^9$ configuration at the copper(II) centre, which leads to an unpaired electron residing in the dx^2-y^2 orbital and hence paramagnetic behaviour. Paramagnetism is particularly problematic in analytical techniques such as NMR spectroscopy due to the fast spin-lattice (T_1) relaxation of the NMR signal, which results in very broad, usually abstruse resonances in the spectra. The fast relaxation originates from through-space interactions between the spin of an unpaired electron and the nucleus of interest. The interaction between the spin of an unpaired electron and the nuclear spin is strongly distance dependent, with the effect rapidly decreasing with increasing distances from the paramagnetic centre. Thus, if a nucleus is situated suitably far away from the paramagnetic centre, the spin-lattice relaxation may be so slow (i.e. the T_1 value is higher) that the resonance for the nucleus may become observable in the NMR spectrum.

Considering the above, it was hypothesised that NMR spectroscopy could help elucidate the location of copper(II) binding through the extent of the relaxation of particular resonances in the ^{1}H NMR. For example, Figure 23 shows the ^{1}H NMR spectrum of **48**, where the resonances of the 1,10-phenatroline ^{1}H's, $H^{a\text{-}g}$, would lie very close to the copper(II) centre if copper(II) was bound through the 1,10-phenanthroline head group, rendering them unobservable in the ^{1}H NMR spectrum. Since the alkyl linker and hydroxamic acid zinc(II) binding group are situated much further away from the copper(II) centre in this instance, their resonances, $H^{i\text{-}p}$, may potentially be observable in the NMR spectrum. In contrary, if the copper(II) centre was chelated via the hydroxamate, the alkyl linker and hydroxamic acid ^{1}H resonances would experience fast spin-lattice relaxation and not be seen, yet the 1,10-phenathroline ^{1}H resonances may still be visible.

To conduct this study, 5 mg of **54** was dissolved in DMSO-d_6 and the ^{1}H NMR spectrum recorded at 298 K. The result of this experiment is shown in Figure 23, where the ^{1}H resonances for the 1,10-phenanthroline head group are completely unobservable, and broad, yet observable, signals exist for the hydrophobic linker and hydroxamic acid ^{1}H's ($H^{i\text{-}n}$ and $H^{o/p}$, respectively). An overlay of the ^{1}H NMR spectrum for **48** and **54** is also shown in Figure 23, which demonstrates the results of the NMR study. The broad signals observed in Figure 23 for **54** overlay extremely well with the alkyl resonances and hydroxamic acid resonances for **48**, whereas the aromatic signals that exist for **48** are too broad to be observed for **54** due to faster spin-lattice relaxation.

This study reveals clearly that the 1,10-phenanthroline head group lies closer in space to the paramagnetic copper(II) centre than both the hydrophobic linker and hydroxamic acid functionality. This study provides strong evidence in favour of copper(II) binding via the 1,10-phenathroline head group as opposed to the hydroxamate. It is worth mentioning that the ^{1}H's for the hydrophobic linker and hydroxamic acid of **54** are still sufficiently close to the copper(II) centre for the ^{1}H's to experience the paramagnetic relaxation effects described, hence the signal broadening in Figure 23, but the spin-lattice relaxation is not so fast that their resonances cannot be observed in the NMR spectrum.

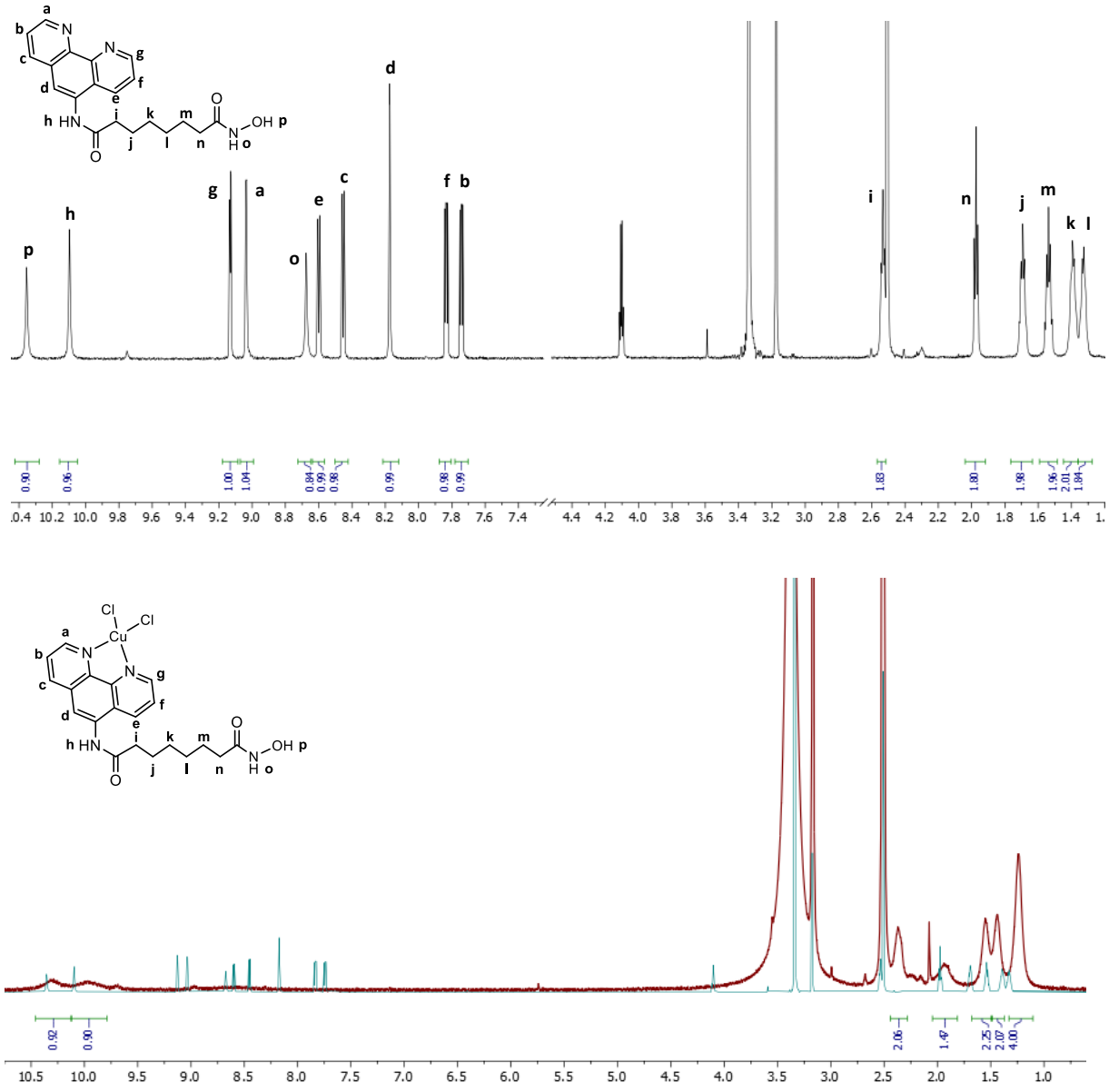

*Figure 23: a) Assigned ^{1}H NMR spectrum of **48** in DMSO-d_6 (top) and assigned ^{1}H NMR spectrum of **54** in DMSO-d_6 (red) with the ^{1}H NMR spectrum of **48** (green) overlaid for comparison of the paramagnetic relaxation effects (bottom).*

With the results of the copper(II) paramagnetic relaxation study in hand, further evidence to support the 1,10-phenathroline binding mode was gathered through infrared (IR) spectroscopy. The hydroxamic acid zinc binding group possesses carbonyl functionality, which is ideal for interrogation through this technique due to the strong C=O stretching vibration of the carbonyl group that occurs in a unique part of the IR spectrum. The strength of the carbonyl absorption is due to a large change in dipole moment upon stretching of the polarised C=O bond, where the unique range of 1500-1800 cm^{-1} in which the vibration occurs, owes itself to the strength of the carbonyl bond. For example, if the hydroxamate were to chelate copper(II) to yield **54**, it would be expected that the wavenumber for the carbonyl stretching vibration would shift to lower wavenumbers since electron density is being removed from the carbonyl bond since the oxygen atom is donating electron density to the copper(II) centre, subsequently reducing the carbonyl strength, which would lead to a smaller force constant and in turn a lower wavenumber in accordance with Hooke's Law. If the hydroxamic acid was not involved in binding copper(II), no shift in wavenumber would be seen for the carbonyl absorption.

An IR spectrum was first recorded of **48** (Figure 25), where there are two intense absorbances in the characteristic carbonyl region at 1650 cm^{-1} and 1540 cm^{-1} for the stretching vibration of the two carbonyl groups in the molecule. Conclusive assignment of a particular absorbance to a specific amide or hydroxamic acid carbonyl is not possible, but consideration of the electronic effects ongoing in **48** can be used as a guide for an approximate assignment. The nitrogen atom in any amide exhibits a positive mesomeric effect (+M), where it can donate its lone pair of electrons into the carbonyl bond, to give a resonance form as illustrated in Figure 24. **57** results in significant single bond character of the carbonyl bond, and when its carbonyl stretching frequency is compared to that of an analogous carboxylic acid, the amide carbonyl will appear at a lower wavenumber in the IR spectrum due to its lower force constant than the carboxylic acid - since the oxygen atom of the carboxylic acid is a poorer lone pair donor than a nitrogen atom due to its higher electronegativity. The resonance exhibited in amide bonds are a reason for their great stability, however, the addition of substituents adjacent to the nitrogen in the amide can change the relative proportions of these two canonical forms.

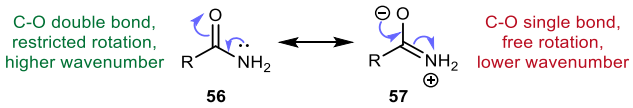

Figure 24: Canonical forms of the amide bond and subsequent effect on the wavenumber of the infrared absorption.

Considering the structure of both **48** and **54**, the presence of the 1,10-phenanthroline aromatic ring system next to the amide nitrogen strengthens the carbonyl bond since the nitrogen lone pair can be delocalised around the phenanthroline ring, resulting in greater double bond character of the carbonyl, so a higher wavenumber carbonyl stretch will be observed due to the larger force constant. For the hydroxamic acid, the nitrogen atom is not subject to any mesomeric effects, but instead inductive, where the nitrogen atom of the hydroxamic acid experiences an inductively withdrawing effect from the oxygen atom of the hydroxyl group. Although the inductive effect will result in a shift in the carbonyl stretch to higher wavenumbers, the delocalisation of the nitrogen lone pair in the amide around the aromatic ring is expected to be more significant, leading to the amide carbonyl having more double bond character, a higher force constant and hence assigned to the higher wavenumber value of 1650 cm^{-1}.

An IR spectrum was then recorded for copper complex **54**, where an overlay of the IR spectra obtained for both **48** and **54** can be viewed in Figure 25. The carbonyl stretches for the amide and hydroxamic carbonyls in **54** appear at the same wavenumber as in the spectrum of **48**, which is further evidence that the hydroxamic acid is not involved in the binding of copper(II) to form **54**. The spectra differ noticeably in their intensity, but this is wholly due to the difference in sample concentrations and not reflective of perturbations in the chemical bonding. In summary, the IR spectroscopy data complements the NMR paramagnetic relaxation studies, in which both analytical techniques support copper(II) complexation through the 1,10-phenanthroline head group.

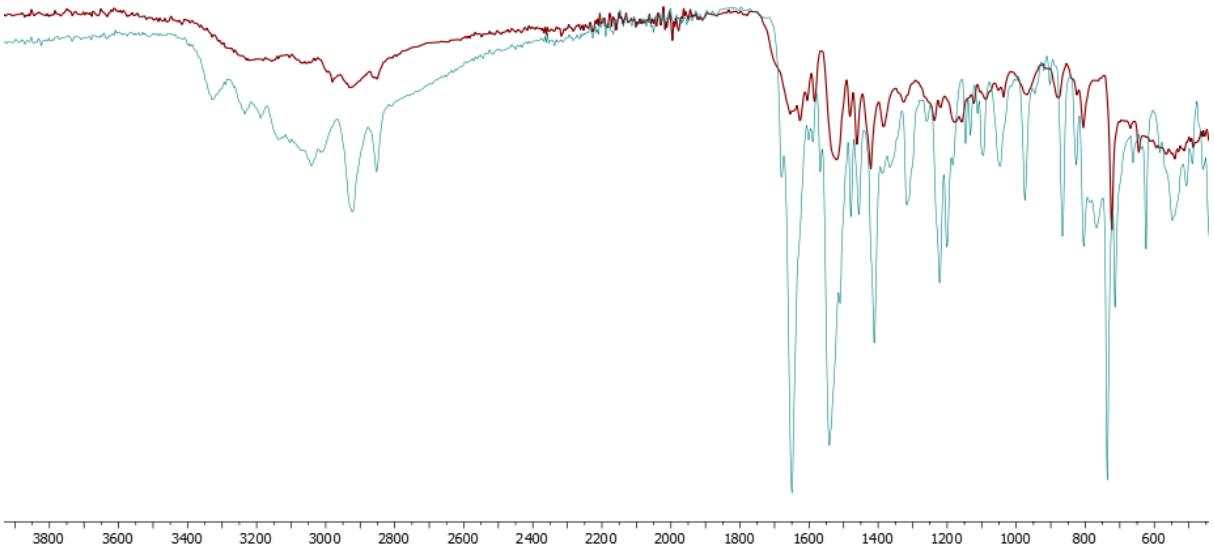

*Figure 25: Superimposed infrared spectra of **54** (green) and **48** (red) to monitor any shifts in wavenumber of the carbonyl functional groups upon copper(II) complexation.*

2.1.3 Histone deacetylase enzyme inhibition assay

To investigate the suitability of **54** as an HDAC inhibitor, a general HDAC enzyme assay was conducted, as described in **Section 4.2**. A two-point assay was performed at concentrations of 10 μM and 1 μM for **54**, **48** and the reference compound SAHA, with the results shown in Figure 26.

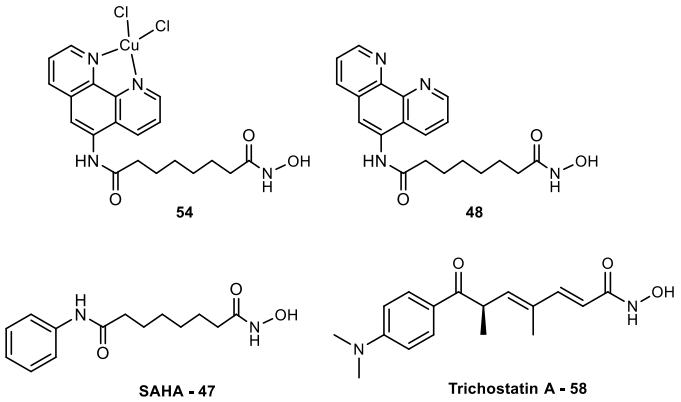

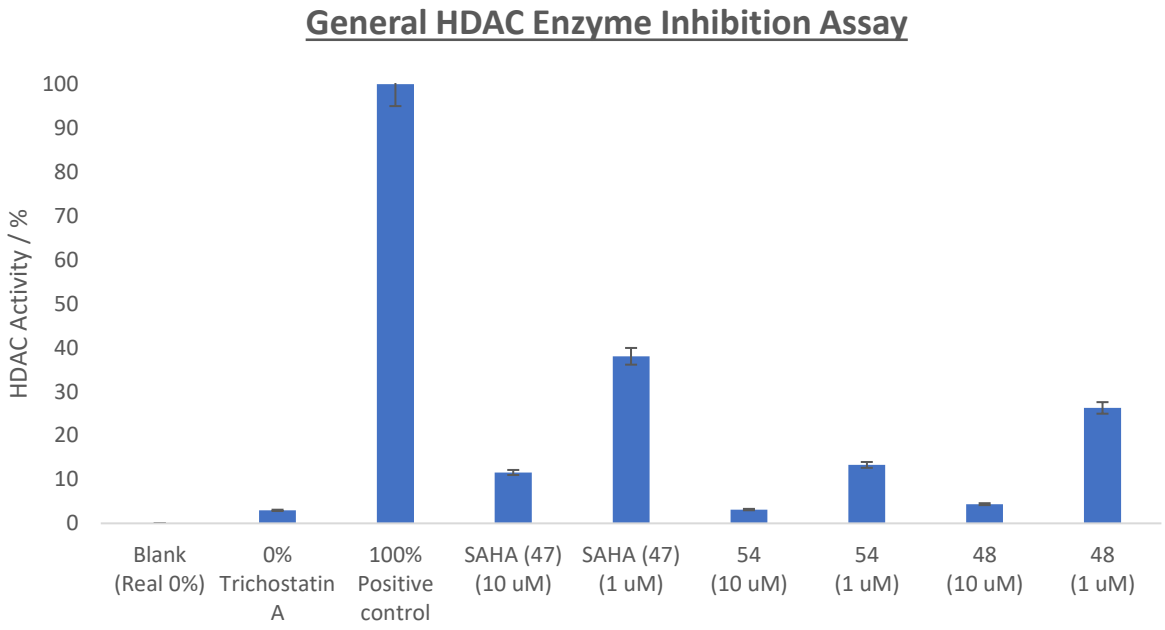

*Figure 26: Two-point general HDAC inhibition assay results at concentrations 10 μM and 1 μM for **SAHA** (**47**), **54** and **48**.*

This initial testing shows very promising results for complex **54**. At both 10 μM and 1 μM inhibitor concentrations, **2c** is a more effective HDAC inhibitor than both the ligand itself, **48**, and clinically approved SAHA. The extent of inhibition at 10 μM is very close to that of Trichostatin A (**58**) (TSA), the so-called 100 % effective inhibitor, which demonstrates the immense potency of **54**.

Inhibitory drugs are often compared through an IC_{50} value, i.e. the minimal concentration of a drug that is required for 50% inhibition *in-vitro*, therefore, the assay was repeated using 8

different concentrations of **54** at 10.0 μM, 2.50 μM, 625 nM, 156 nM, 39.1 nM, 9.77 nM, 2.44 nM and 0.100 nM and a different 8 concentrations of 20.0 μM, 5.00 μM, 1.25 μM, 313 nM, 78.1 nM, 19.5 nM, 4.88 nM and 0.100 nM for **48** and SAHA (**47**) to determine each of their IC_{50} values. The results of this assay are shown in Figure 27.

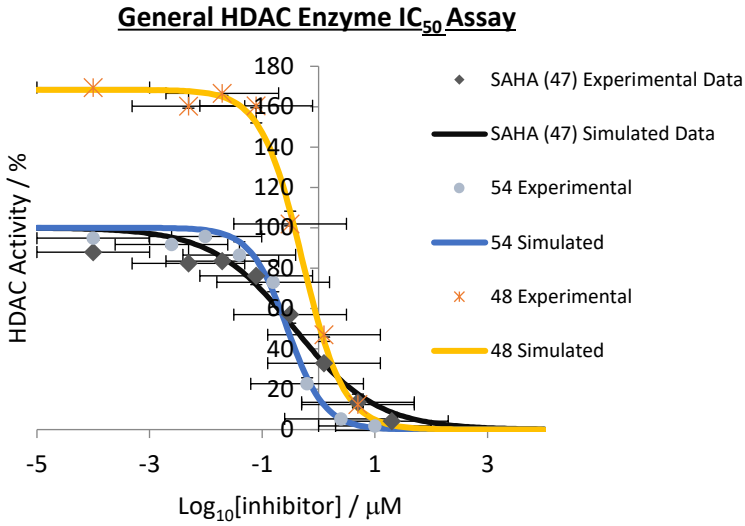

Compound	IC_{50} / μM
SAHA (**47**)	0.70 ± 0.05
54	0.32 ± 0.02
48	0.51 ± 0.06

*Figure 27: IC_{50} plots for **54**, **48** and SAHA (**47**) with their IC_{50} values shown in the table.*

The calculated IC_{50} value of 0.32 ± 0.02 μM for **54** is lower than that of both **48** and SAHA (**47**), which agrees with the two-point assay, in that **54** is a more potent HDAC inhibitor since a lower concentration of the drug is needed for the same level of HDAC enzyme inhibition. From the lower IC_{50} of **54** compared to **48**, it is clear that the addition of copper(II) is improving the drug potency. As a control to demonstrate that merely the presence of copper(II) does not inhibit the HDAC enzyme, an IC_{50} assay was conducted for **51**, which lacks the hydroxamic acid zinc(II) binding group, where this complex was found to have an IC_{50} = 11.33 ± 0.08 μM, demonstrating that the hydroxamate functionality is essential for activity as an HDAC inhibitor.

2.2 Copper(II) pyrithione HDAC inhibitors

2.2.1 Attempted synthetic routes

Following the successful synthesis of **54**, it was desirable to expand our copper(II) HDAC inhibitor library. Copper pyrithione complexes have been subject to intense study by the Walton Group, with some complexes reported to exhibit impressive antibacterial and anticancer activity, potentially due to the copper(I)/copper(II) redox activity.[112] The pyrithione ligand is an organosulfur compound, formally termed as a 1-hydroxypyridine-2-thione. Pyrithiones exist as

a pair of tautomers, shown in Figure 28, where the thione and thiol tautomers are the major and minor form, respectively.

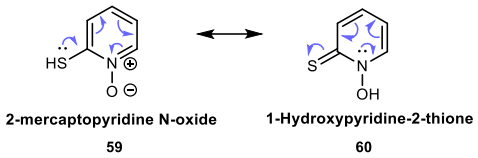

2-mercaptopyridine N-oxide **1-Hydroxypyridine-2-thione**

59 **60**

*Figure 28: Thiol and thione tautomers of the pyrithione ligand - termed 2-mercaptopyridine N-oxide (**59**) and 1-hydroxypyridine-2-thione (**60**), respectively.*

A plethora of copper(II) complexes possessing functionalised pyrithione ligands have been synthesised by the Walton Group (Figure 29), yet no studies have focussed on incorporation of a hydroxamic acid HDAC inhibitor to this ligand.

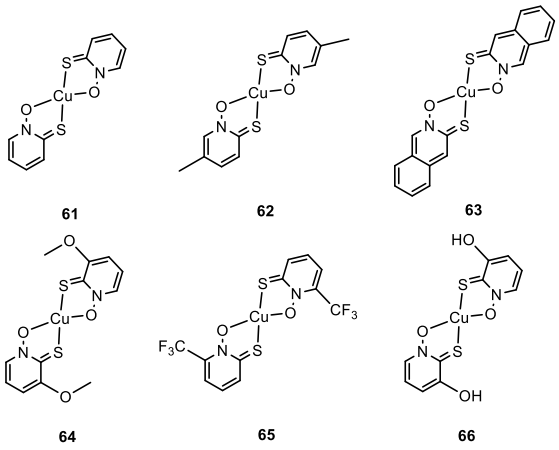

61 **62** **63**

64 **65** **66**

Figure 29: Copper(II) pyrithione complexes previously synthesised by the Walton Group.

It was proposed that a dual-action copper(II) HDAC inhibitor could be synthesised through incorporating a pyrithione ligand as our head group to bind the copper(II) centre. It is hoped that the combination of a HDAC inhibition combined with a copper(II) pyrithione complex could give synergistic anticancer activity. The synthetic strategy followed for obtaining our target, **72**, is shown in Scheme 3.

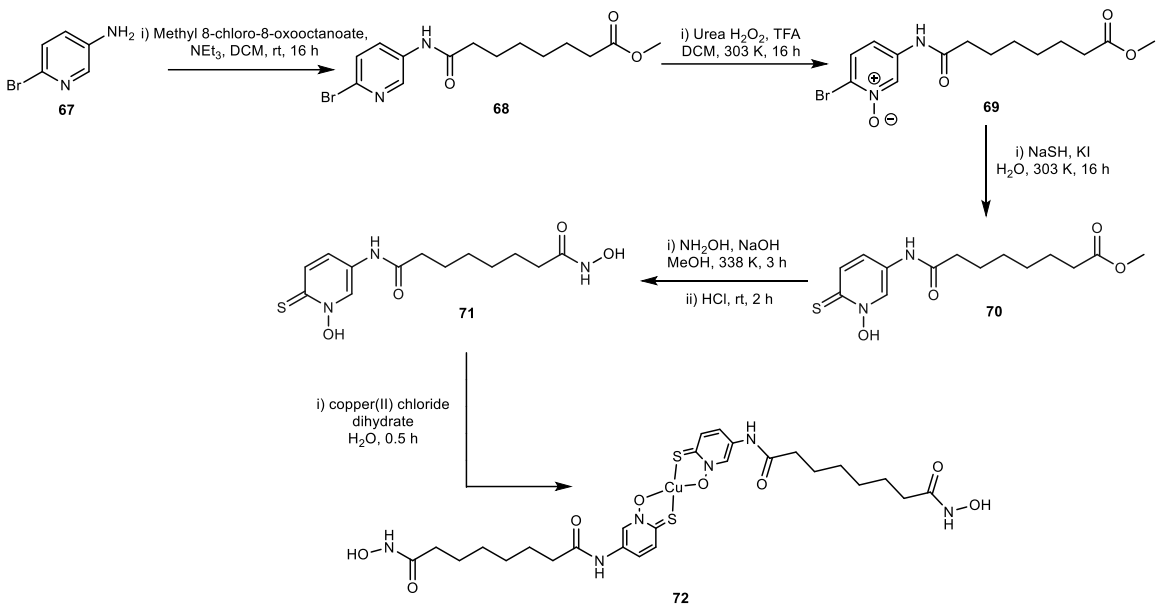

Scheme 3: Proposed synthetic route for copper(II) pyrithione HDAC inhibitor, **72**.

The starting reagent, 5-amino-2-bromopyridine (**67**), possesses amine functionality for a base catalysed nucleophilic addition to methyl-8-choro-8-oxooctanoate to successfully synthesise **68**, which was confirmed by NMR Spectroscopy and mass spectrometry. Conversion of **68** to the N-oxide, **69**, was achieved using an oxidising agent consisting of urea hydrogen peroxide and trifluoroacetic anhydride (TFA), confirmed via the shift in the aromatic resonances in the ^{1}H NMR spectrum and mass spectrum. The oxidising agent meta-chloroperoxybenzoic acid (mCPBA) is a common reagent for the conversion of pyridines to their N-oxides, however, in initial tests the oxidising power of this reagent was insufficient for formation of **69**. Owing to the *in situ* generation of the strong organic peroxy acid, trifluoroperacetic acid, when using a mixture of urea hydrogen peroxide and TFA, **69** was synthesised in excellent yield. A likely issue in the use of mCPBA for the oxidation of **68** lies in the electron deficiency of the pyridine ring of **68**. The *ortho*-bromine atom of **68** inductively withdraws electron density from the aromatic pyridine ring to result in an electron deficient pyridine ring. Since nucleophilic attack of the nitrogen lone pair, held in an sp^2 orbital orthogonal to the π-system, must occur on the peroxy acid to form the N-oxide, a peracid that is more electrophilic than mCPBA, such as trifluoroperacetic acid, is needed to achieve efficient nucleophilic attack of the pyridine.

Installation of the thiol group via aryl substitution to form **70** (Scheme 3) proved extremely problematic and challenging in its synthesis, where a variety of procedures were trialled. Initially, 100 mg of **69** was suspended in water with an excess of sodium sulfide (Na_2S) at room temperature. The reaction proceeded overnight and showed no evidence of pyrithione

formation in the mass spectrometric data. The result was unsurprising due to the poor solubility of **69** in the reaction mixture. Due to the solubility challenges, a temperature series was investigated, spanning from 293 K to 373 K in 20 K intervals. Despite the improved solubility, particularly at 353 K, analysis of the reaction media showed no evidence of **70** formation. An alternative method involves the use of excess sodium hydrosulfide (NaSH) in water instead of Na_2S. The speciation of Na_2S in water leads to Na_2S reacting as the bisulfide anion (HS^-), therefore, using a direct source of the bisulfide anion may lead to the target **70**. The solubility trend was very similar to that exhibited for Na_2S, where 353 K showed excellent solubility, yet still no product was observed. Other procedures involving the use of equimolar mixtures of sodium sulfide and sodium hydrosulfide, and the addition of sodium hydroxide were also trialled, yet revealed no product.

Adamek and co-workers reported the synthesis of numerous derivatives of pyrithione ligands from their N-oxide precursors through use of a potassium iodide catalyst and excess sodium hydrosulfide.[113] Due to the improved solubility seen at 353 K for **69**, this procedure was trialled at this temperature and reacted overnight. There was no evidence of a peak in the mass spectrometric data for **70**, however, the ^1H NMR obtained after work up of this reaction, shown in Figure 30, provided very insightful information.

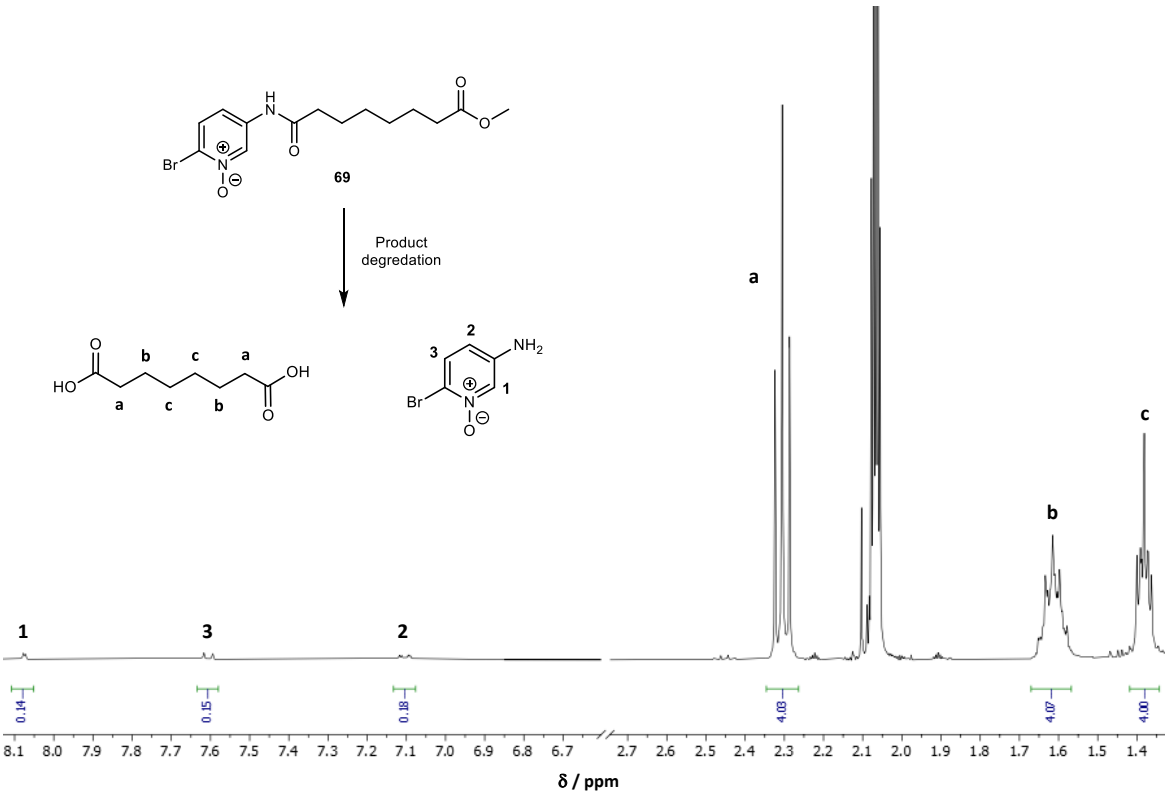

Figure 30: ^{1}H NMR of spectrum obtained after workup of reaction conditions reported by Adamek and co-workers in DMSO-d_6, showing decomposition of ***70***.

The resonances at δ 1.38 (4H, m, H^{c}), δ 1.62 (4H, m, H^{b}) and δ 2.30 (4H, t, $^{3}J_{HH}$ = Hz, H^{a}) correspond to the alkyl linker protons. The relative integral of 4H's for δ 2.30 is interesting since these proton resonances are not usually equivalent and typically give two resonances each in the ^{1}H NMR spectrum, with each signal possessing an integral of 2H. The equivalence of these resonances suggests both ends of the alkyl linker are identical hence we do not see a chemical shift difference. Inspection of the aromatic region confirms decomposition of **69**, since the weak resonances at δ 8.07 (d, $^{4}J_{HH}$ = 2.05 Hz, H^{a}) , δ 7.61 (d, $^{3}J_{HH}$ = 9.03 Hz, H^{3}) and δ 7.10 (dd, $^{3}J_{HH}$ = 9.03 Hz, $^{4}J_{HH}$ = 2.05 Hz, H^{2}) integrate to approximately 4% of that of the alkyl ^{1}H's. If the pyrithione head group and hydrophobic alkyl linker were part of the same molecule, the relative ^{1}H integrals would be 1:2, respectively. It is not immediately clear how the decomposition of the molecule is occurring, but it is obvious that the substitution pattern on the pyridine ring is preserved since three ^{1}H's exhibiting the magnitudes of scalar coupling they do, support a 2,5-substituted pyridine species. Considering the above, it is logical to expect that the amide bond in **70** is cleaved to release the 5-amino-2-bromopyridine N-oxide from the hydrophobic linker. A plausible explanation could be deprotonation of water by bisulfide anions to produce hydroxide ions, which in turn attack the amide bond to liberate carboxylic acid functionality on the linker. This reaction must occur at both carbonyl groups on the alkyl linker due to the equivalence of

protons H^a and H^b, releasing the alkyl linker as a dicarboxylic acid, which is supported in the mass spectrometric data with an *m/z* 175.15. Comparison of the aromatic chemical shifts to 5-amino-2-bromopyridine suggest that the 5-amino-2-bromopyridine is not the aromatic species responsible for the resonances, with the more deshielded ortho ^1H, and more shielded para ^1H, supporting 5-amino-2-bromopyridine N-oxide as the aromatic species. The broad signals to the right of each aromatic peak suggest the presence of some 5-amino-2-bromopyridine, however, most of this signal is lost in the noise.

The mass spectrometric data also shows significant presence of a species with *m/z* 157.87, which corresponds to the acylium cation generated by cleavage of the C-N bond of the amide in the ESI experiment. The significant formation of this ion illustrates the lability of the amide bond in **70**, which is perhaps uncharacteristic due to the resonance stabilisation amides exhibit. The lability of this amide bond can be rationalised by considering the resonance stabilisation of the resulting 5-amino-2-bromopyridine N-oxide anion upon both fragmentation in the ESI mass spectrometer and nucleophilic acyl substitution. Four canonical forms exist for the 5-amino-2-bromopyridine N-oxide anion, where such delocalisation lends itself to be a very stable leaving group and hence leads to the amide bond being more susceptible to nucleophilic attack than would be expected.

The improved solubilisation of **69** observed in the reaction media at higher temperatures correlates with chemical decomposition of the molecule, therefore, it was decided to repeat the procedure published by Adamek *et al.* at room temperature and monitor the reaction over a period of days. After 48 hours of stirring, mass spectrometric analysis of the reaction mixture displayed a peak at *m/z* 299 which had not previously been seen in any mass spectra. The molecular weight of **70** is 312 $gmol^{-1}$, where a loss of CH_2, perhaps due to COOMe converting to COOH, once accounting for protonation in ESI experiment, would result in the species detected in the mass spectrum. It is plausible that the methyl ester not preserved in the reaction product when considering the conversion of the alkyl linker to a dicarboxylic acid seen previously. High resolution mass spectrometry was used to confirm that the molecular ion at *m/z* 299 belonged to **73** with molecular formula $C_{13}H_{19}N_2O_4S$ (Figure 31). The ^1H NMR spectrum of **73** supports formation of the carboxylic acid derivative of **70**, where no ^1H resonance is observed for the methyl group, and the pyrithione head group and hydrophobic alkyl linker possess the expected relative resonance integrals. The ^1H NMR spectrum also supports the pyrithione ligand existing as the expected thione tautomer, owing to the resonance at δ 10.37 (1H, br, H^a) that possesses an nOe to δ 8.96 (H^d), which is indicative of a protonated N-oxide.

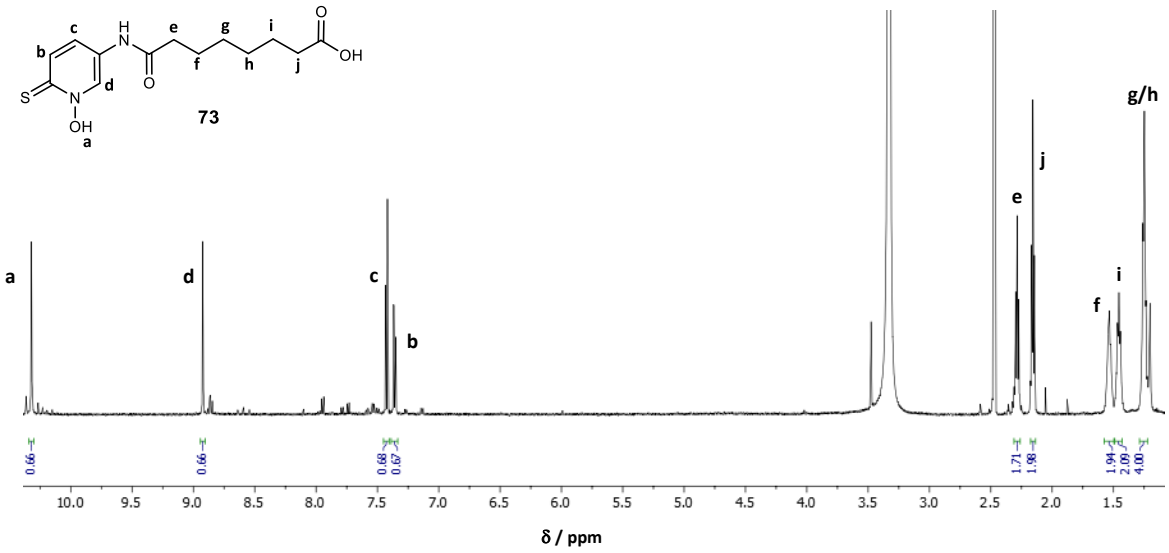

*Figure 31: Assigned ^{1}H NMR spectrum of **73** in DMSO-d_6.*

Upon optimisation of the reaction conditions for the synthesis of **73**, yields as high as 15% could only be achieved. The low yielding nature of the reaction is thought to be due to the chemical decomposition of **69** still occurring at this lower temperature, where formation of **73** and decomposition by the hydroxide ions are in competition. It is apparent that the presence of a potassium iodide catalyst is imperative for the successful formation of the pyrithione group. The exact reason is not clear, where a halogen exchange reaction on the aromatic ring has been hypothesised, since iodide is an excellent nucleophile owing to its lower electronegativity than the other halogens, but also a better leaving group than bromide, due to its larger atomic radius and associated lower bond enthalpy through the poorer orbital overlap. Another reason for the potassium iodide catalyst may lie in the stability of the associated salt biproduct. For example, the higher lattice enthalpy of potassium bromide (KBr) than potassium iodide (KI) possibly drives the reaction, where interactions between the potassium cation and the bromide substituent lead to greater polarisation of the aryl bromide bond, and subsequently more efficient nucleophilic attack of the bisulfide anion.

Although the pyrithione head group has been successfully synthesised, converting the carboxylic acid functionality of **73** to the required hydroxamic acid zinc binding group presented a new challenge. Installation of the hydroxamic acid into SAHA derivatives is routinely achieved by reaction of the methyl ester precursor in the presence of hydroxylamine. It was therefore attempted to convert carboxylic acid back to the methyl ester to yield **70** via refluxing **73** in methanol in the presence of a H_2SO_4 catalyst as shown in Figure 32. Conversion of the carboxylic

acid to the methyl ester was not observed under these conditions, so alternative routes were explored.

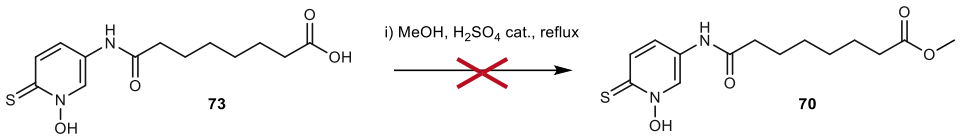

*Figure 32: Attempted conversion of the carboxylic acid **73** to the methyl ester **70** using a H_2SO_4 catalyst.*

Giacomeli and co-workers previously reported the one-step conversion of carboxylic acids to hydroxamic acids under very mild conditions for a variety of amino acids. The procedure used is shown in Figure 33 and was trialled on **73**.[114]

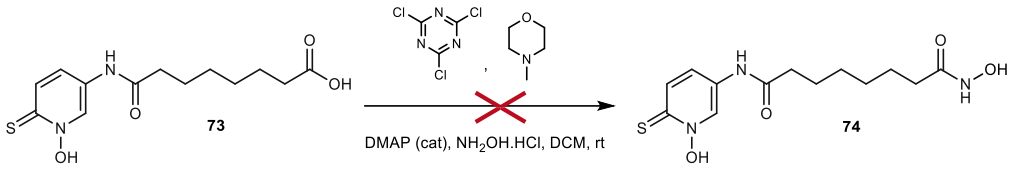

Figure 33: One-step conversion of carboxylic acids to hydroxamic acids under the very mild conditions reported by Giacomeli and co-workers.[114]

Although low resolution mass spectrometry revealed a peak at *m/z* 314.46 which supported conversion to the hydroxamic acid, high resolution mass spectrometry did not support such product since no feasible molecular formula fitted within the range of such mass. In addition, the ^{1}H NMR experiments also proved unsuccessful where the signal to noise ratio was so poor that the spectrum was rendered uninterpretable.

With few procedures of such reactions reported in the literature, and further restrictions due to solubility of **73** in only DMF and DMSO solvents, formation of a copper pyrithione complex from **73** was attempted, with a view to install the hydroxamic acid zinc binding group after copper complexation. Stirring of **73** in DMF at room temperature, followed by the dropwise addition of 0.5 equivalents of copper(II) chloride dihydrate produced **75** as characterised by high resolution mass spectrometry with a molecular ion peak at *m/z* 658.57 (Figure 34). Unfortunately, **75** did not possess solubility different from that of **73**, where DMF and DMSO were the only suitable candidates. As expected, the subsequent reactions to install the hydroxamic acid binding group to **75** were unsuccessful.

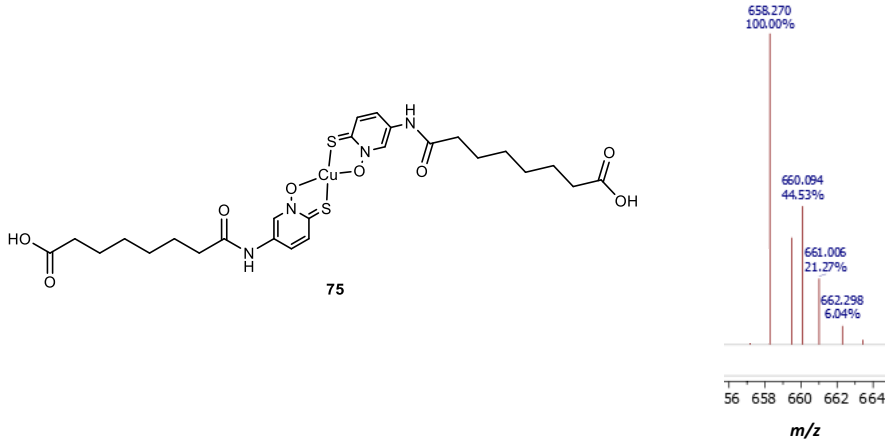

*Figure 34: Copper Isotope cluster in the ESI mass spectrum to suggest formation of **75**.*

2.2.2 *Pyrithione ligands as HDAC zinc(II) binding groups*

The difficulty in installing hydroxamic acid functionality to the pyrithione ligand led to an attempt to exploit the pyrithione group as the zinc binding group itself. The binding potential of pyrithione ligands for the Zn^{2+} dependent HDAC enzyme targets had already been realised by Muthyala and colleagues, where three novel molecules were reported in their work, as shown in Figure 35. These compounds offered excellent HDAC inhibition and the electron density maps obtained from X-ray crystallography displayed almost identical binding geometries of hydroxamates and pyrithiones to the zinc(II) metal in the HDAC enzyme pocket.[115]

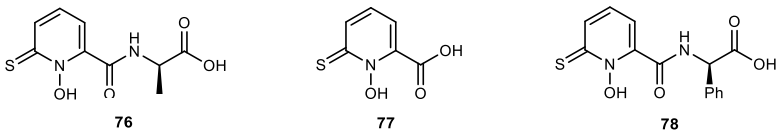

*Figure 35: Pyrithione HDAC inhibitors **76**, **77** and **78** synthesised by Muthyala and co-workers.*[115]

Referring to Figure 35, it is intriguing that the pyrithione HDAC inhibitors reported to not mimic the structural motif of SAHA or other clinically approved HDAC inhibitors. Hence, with molecule **73** in hand, it was attempted to perform an amide coupling reaction with aniline to produce **79** (Scheme 4), which is a direct mimic of SAHA (**47**), with the hydroxamate functionality switched for a pyrithione zinc binding group (Figure 48).

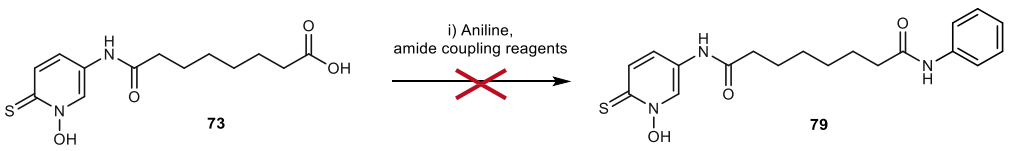

*Scheme 4: Generic scheme for the amide coupling reaction of **73** with aniline to synthesise pyrithione SAHA mimic, **79**.*

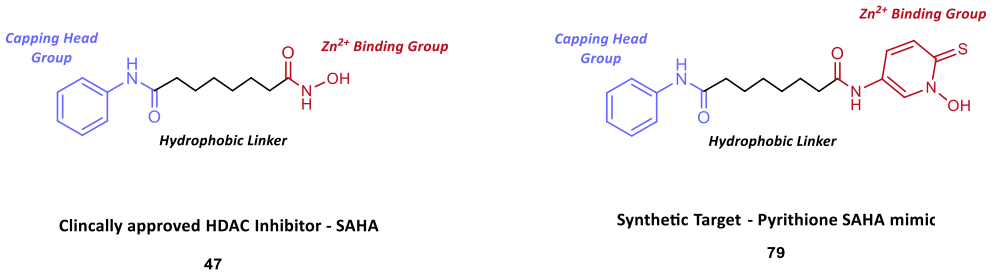

*Figure 36: Clinically approved suberoylanilide hydroxamic acid (SAHA) (**47**) and amide coupling pyrithione HDAC inhibitor target (**79**).*

Amide coupling reactions require use of a coupling agent to invoke reactivity into the carboxylic acid, where the initial coupling reagent tested was 1-ethyl-3-(3-dimethylaminopropyl)carbodiimide (EDC) due to its water-soluble urea biproducts which simplify the purification. The reaction is expected to proceed through the mechanism illustrated in Figure 37 where the hydroxyl group of the carboxylic acid attacks the carbon centre of the diimide of EDC to yield an activated ester. Hydroxybenzotriazole (HOBt) then attacks the ester via its hydroxyl group to undergo a nucleophilic acyl substitution, liberating a water-soluble urea biproduct and activated benzotriazole ester. The activated benzotriazole ester is subsequently attacked by the amine, aniline in this case, to yield the amide coupled product **79**. HOBt is commonly employed in amide coupling reactions to suppress racemisation of single enantiomer chiral compounds, and to suppress formation of the N-acyl urea biproduct that reduces the overall yield. Despite this, the reaction was also performed in absence of HOBt.

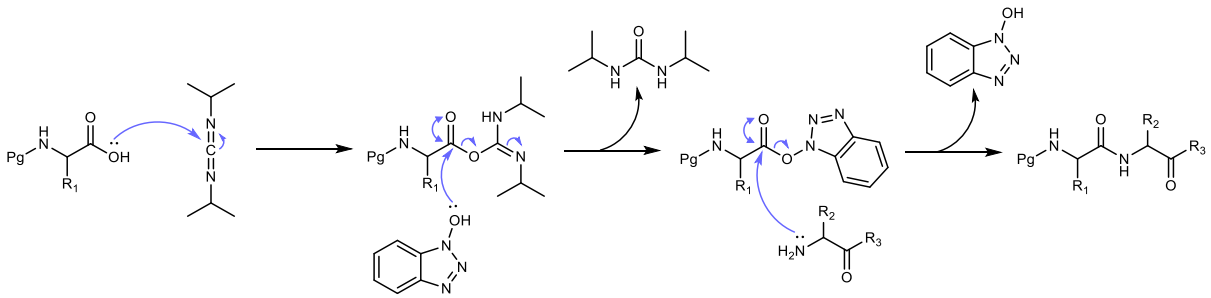

Figure 37: Amide coupling mechanism using 1-ethyl-3-(3-dimethylaminopropyl)carbodiimide (EDC) as a coupling reagent.

Mass spectrometric analysis of the reactions with and without HOBt revealed a peak at *m/z* 373.46 supporting formation of our target **79**, however, the ^{1}H NMR spectra obtained after workup did not support such findings in both cases. The ^{1}H NMR spectrum, shown in Figure 38, clearly shows resonances in the aromatic region for aniline bound to the hydrophobic linker, but the pyrithione resonances cannot be seen in the spectrum. The relative integrals between aniline and the hydrophobic linker suggest only one aniline molecule is bound. The loss of the pyrithione zinc binding group suggests that the amide coupling reaction has occurred on the amide functional group instead of the carboxylic acid. This result is not too surprising since in **Section *2.2.1*** it was exhibited that the amide bond of **70** was significantly more labile than anticipated due to extensive resonance stabilisation of the 5-amino-2-bromopyridine N-oxide leaving group. The ESI mass spectrometry data supports the formation of aniline bound to the carboxylic acid linker, with a molecular ion peak at *m/z* 250.81. The mass spectra also reveal strong presence of a species with *m/z* 325.74, which would fit with aniline substituting twice, but this is not in agreement with ^{1}H NMR data, which is possibly a reflection of the impressive sensitivity of mass spectrometry compared to NMR spectroscopy.

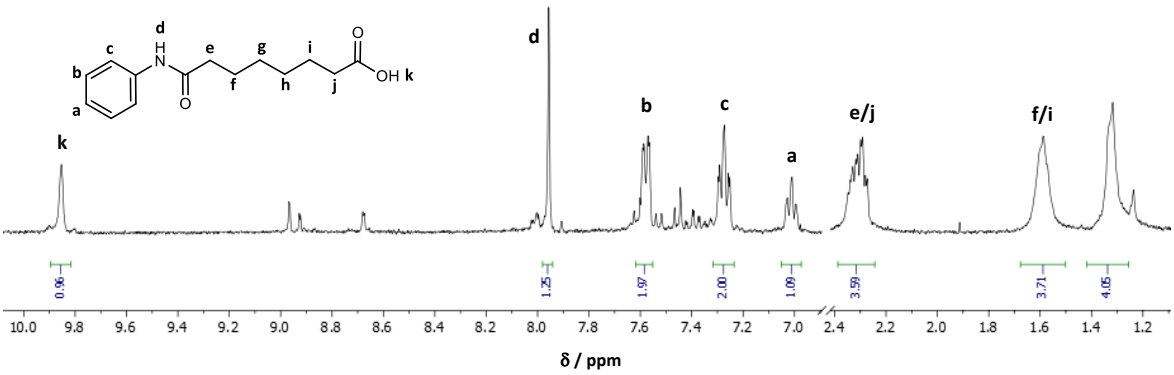

Figure 38: Assigned ^{1}H NMR spectrum of the 1-ethyl-3-(3-dimethylaminopropyl)carbodiimide (EDC) amide coupling product in DMSO-d_6.

Alternative coupling reagents were explored in case any difference in selectivity between the amide and carboxylic acid groups were observed. In particular, the propanephosphonic acid anhydride (T3P) coupling agent was investigated owing to its excellent reaction selectivity, high product purities, excellent yields, and relevance in current industrial syntheses. T3P exists as a cyclic trimer, with a phosphorus–oxygen core, where its chemical reactivity in amide couplings imitates EDC. Despite the exciting profile of this amide coupling reagent, the same observations as for EDC were observed. The lack of success in obtaining **79** lies in the stability of the pyrithione head group – even if it were possible to isolate **79**, this inherent instability renders it

a poor drug candidate in the first instance. The synthesis of **79** was therefore not pursued any further and other synthetic routes explored.

2.2.3 'Click' reaction for copper(II) pyrithione HDAC inhibitors

Referring back to the pursuit of a Cu(II) pyrithione HDAC inhibitor, a Cu(II) pyrithione complex with alkyne functionality, **80**, shown in Figure 39, had been previously synthesised in the Walton Group, opening up alternative synthetic routes which could incorporate the infamous 'click' and Sonogashira cross-coupling reactions.

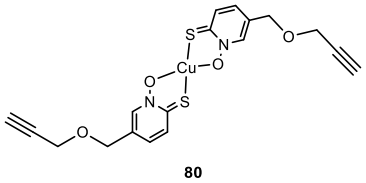

80

*Figure 39: Copper(II) pyrithione complex with alkyne functionality, **80**, for potential 'click' and Sonogashira reactions with a suitable HDAC inhibitor.*

It was first decided to explore the 'click' reaction pathway. This reaction is pericyclic, involving a 1,3-dipolar cycloaddition between an alkyne and azide, which act as a dipolarophile and 1,3-dipole, respectively, catalysed via a copper(I) catalyst (Figure 40). The result of their reaction is a stable 5-membered triazole ring, hence if azide functionality could be installed into a SAHA analogue, the resulting click reaction with **80** would yield a Cu(II) pyrithione HDAC inhibitor. The synthesis began with an attempt to directly substitute an azide group onto the previously synthesised molecule **68**, to form **82**, with the overall reaction scheme shown in Scheme 5.

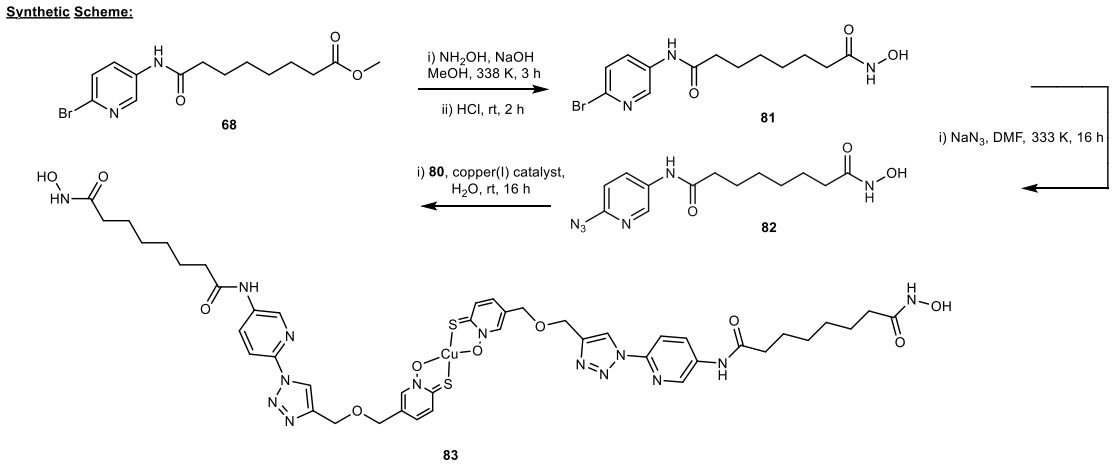

*Scheme 5: Synthetic route proposed for the 'click' reaction of with **80** to form copper(II) pyrithione HDAC inhibitor, **83**.*

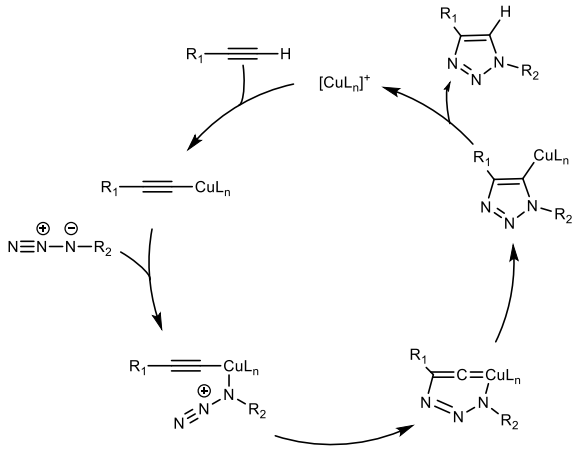

*Figure 40: General catalytic cycle for the azide-alkyne 'click' reaction where $[CuL_n]^+$, R_1 and R_2 are the copper(I) catalyst, copper(II) pyrithione alkyne complex **80** and azide functionalised SAHA analogue **82**, respectively.*

It was hoped that the inductively electron-withdrawing effect of both the nitrogen in the pyridine ring and ortho bromide substituent would be strong enough to result in nucleophilic aromatic substitution at the ortho position through use of an azide nucleophile. A procedure modified from Riva *et al.* was followed whereby **68** was reacted with an excess of sodium azide and ammonium chloride (NH_4Cl) at 383 K overnight. Mass spectrometric analysis of the reaction mixture showed only starting material and no evidence of any chemical transformation. The reaction was then repeated with the addition of a potassium iodide catalyst, in hope for a similar effect as witnessed for the synthesis of **73**, but unfortunately no transformation was seen.

Yuan and colleagues have reported the synthesis of 2-azido-4-aminopyridine from 4-amino-2-chloropyridine using NaN_3 and NH_4Cl at 383 K, which differs slightly from the starting material precursor 5-amino-2-bromopyridine for **68** in the amine group position on the ring and type of

halogen.[116] The close similarity between 5-amino-2-bromopyridine and 4-amino-2-chloropyridine lead to following this procedure, yet no conversion of the starting material was observed. It is evident that nucleophilic aromatic substitution on **68** is challenging, where the bromine is probably not electronegative enough to facilitate this S_NAr, whereas the reported chloride version is. A SAHA analogue was then designed that would facilitate an aliphatic S_N2 substitution mechanism by incorporating an alkyl bromide, that could subsequently be displaced to install the desired azide functionality for the 'click' reaction. Our synthetic rationale is illustrated in Scheme 6, where in the first step of the synthesis, 5-amino-2-methylbenzene reacts with methyl 8-chloro-8-oxooctanoate yield **85**, analogous to that described for **69**. Bromination of **85** to synthesise **86** was hoped to be achieved via reaction with *N*-bromosuccinimide (NBS), where this reaction occurs via a radical substitution mechanism shown in Figure 41.

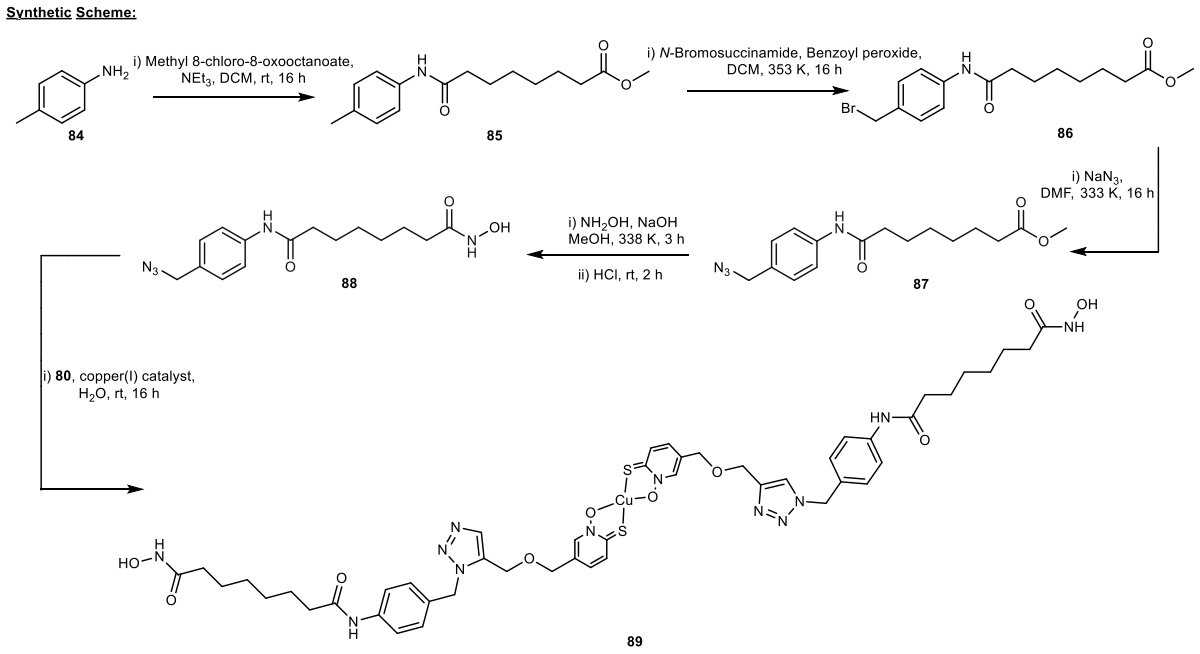

*Scheme 6: Synthetic route proposed for the 'click' reaction of **88** with **80** to form a copper(II) pyrithione HDAC inhibitor.*

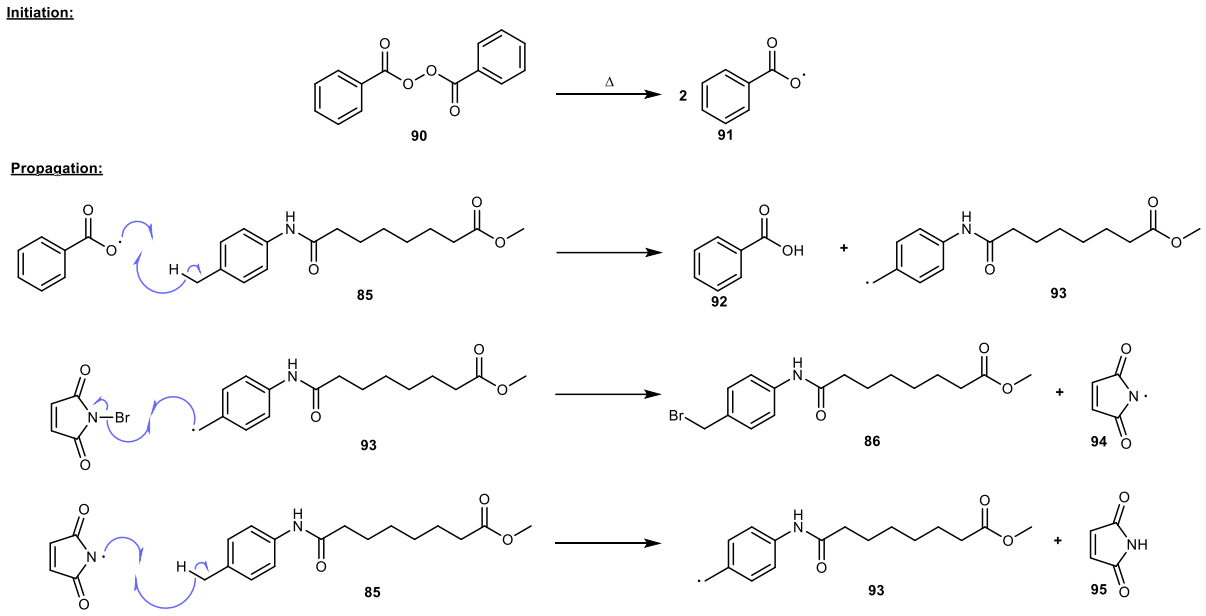

Figure 41: *Free radical mechanism for the allylic bromination of* ***85*** *using N-bromosuccinamide.*

Mass spectrometric analysis of the reaction mixture revealed formation of the intended product **86** with *m/z* 356.35 and the characteristic 1:1 ratio of ^{79}Br and ^{81}Br isotopes. It is also clear from the mass spectrum that a dibrominated species has formed, with *m/z* 435.27 and complex isotope pattern owing to the presence of two bromine atoms in the molecule. Recrystallisation of NBS in water has been proven to reduce the amount of dibrominated species formed in such reactions due to the removal of excess Br_2, hence was used in a repeat of this reaction. Despite this, the dibrominated side product was still present in significant amounts, where chromatographic separation would be required to obtain a pure sample of **86**. This separation proved challenging due to the similarity in the R_f values of **86** and the dibrominated side product, hence co-elution was problematic in the purification. Pure ^{1}H NMR spectra could not be obtained following this method, and overlapping signals in the aromatic region made distinguishing between monobrominated and dibrominated resonances extremely difficult.

In hope to circumvent this problem, it was hypothesised that direct bromination of *p*-toluidine would result in larger polarity differences between the monobrominated and dibrominated products since the alkyl linker would be no longer present. Column chromatographic separation was still challenging, however, a pure ^{1}H NMR of the monosubstituted brominated product was obtained as shown in Figure 42, eluting at 10.5 % ethyl acetate in hexane.

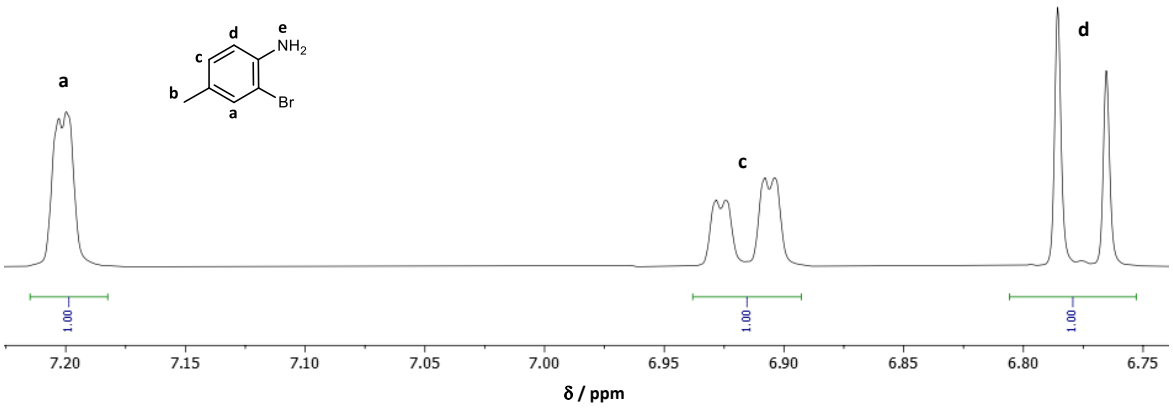

Figure 42: Assigned aromatic ^{1}H NMR of the monobrominated product from the reaction of p-toluidine with N-bromosuccinamide in acetone-d_6.

It is immediately obvious that the expected bromination product has not been synthesised in this reaction due to three aromatic ^{1}H signals in the ^{1}H NMR above ($H^{a,c,d}$), as opposed to the two aromatic resonances expected due to chemical equivalence. Upon integration, these aromatic signals integrate to 1 ^{1}H, where the resonance of the methyl group at δ 2.85 has a relative integral of 3 ^{1}H's. This demonstrates that the methyl group is fully intact and substitution has instead occurred on the aromatic ring. Through consideration of the radical mechanism, it is not logical to expect formation of such species, through the arguments of radical stability. The initial hydrogen atom abstraction of the benzoyl radical in Figure 41 should occur on the methyl group due to resonance stabilisation of the methyl radical with the aromatic ring. Although hydrogen atom abstraction on the aromatic ring is possible, the radical would be held in an sp^2 hybridised orbital orthogonal to the π-system, thus does not experience resonance stabilisation from the aromatic ring. In addition to this, the aromatic radical is held in an orbital with higher s character than the aliphatic methyl radical, which will experience further destabilisation due to its closer proximity to the nucleus, hence another competing mechanism must be in operation. It is apparent that the aromatic ring is electron rich due to the +I effect of the methyl group, and even stronger +M effect of the amine group. This sets up the aromatic ring for electrophilic aromatic substitution with *N*-bromosuccinimide, where the aromatic ring attacks the δ+

bromine atom attached to the nitrogen on the succinimide, as shown in Figure 43, to form a succinimide biproduct which precipitates from the reaction mixture.

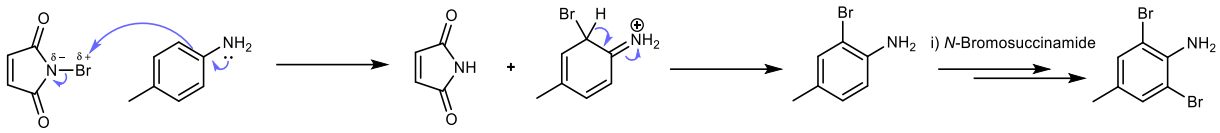

Figure 43: *Electrophilic aromatic substitution mechanism for the formation of monobrominated and dibrominated reaction products using N-bromosuccinamide.*

The regioselectivity observed in the reaction product can again be rationalised through the electronic effects of the substituents. The methyl group is directing to the *ortho* and *para* positions of the aromatic ring, where the *para* position is occupied by the amine group. The amine group also is directing to the *ortho* and *para* positions, but due to being directly opposite the methyl group, the *ortho* position is *meta* with respect to the methyl group. Due to the strong +M effect of the amine group, where +M > +I, substitution is seen on the carbons adjacent to the amine group, leading to the regioisomer shown being made exclusively. This can be confirmed experimentally via 2D NMR spectroscopy, specifically Correlation Spectroscopy (COSY) to reveal ^{1}H coupling partners and Nuclear Overhauser Effect Spectroscopy (NOESY) to reveal ^{1}H's close in 3D space. Referring back to Figure 42, it can be revealed that δ 6.77 shows a strong nOe to δ 6.90, which are also coupling partners. δ 6.90 shows a weak nOe to δ 7.20 and are also coupled, but δ 7.20 couples to nothing else. The methyl group with a resonance at δ 2.18 shows an nOe δ 7.20 and δ 6.90, confirming the assignment in Figure 42.

Considering electrophilic aromatic substitution is occurring on the aromatic ring, we proceeded to change the aromatic ring from benzene to pyridine, conserving the same substitution pattern, in hope that the inductively withdrawing nitrogen atom in the ring would decrease the electron density such that the radical mechanism would out-compete the electrophilic aromatic substitution and form our intended product in isolable yields. The crude product of this reaction was purified via column chromatography where ^{1}H NMR spectroscopy of all the UV-visible fractions unfortunately revealed mono and dibromo electrophilic aromatic substitution products.

The difficulties associated with bromination of the methyl group led to exploration of other suitable leaving groups. An alternative starting material with scope for functionalisation was 4-aminobenzyl alcohol, whereby the hydroxyl group could be converted to a leaving group for the subsequent azide addition. To begin, 4-aminobenzyl alcohol was reacted with phosphorus

tribromide (PBr_3) in Et_2O, to yield 4-(bromomethyl)aniline as reported by Hussaini and co-workers (Figure 44a).[117] Despite this being a literature procedure, the solubility of 4-aminobenzylalcohol was problematic in the reaction mixture, existing as a suspension throughout the reaction. After 16 hours, the solid was separated from the reaction mixture via gravity filtration, after which both solid and filtrate were analysed via mass spectroscopy to reveal no evidence of product in both cases. Different solvents were trialled, with DMF and THF showing to be suitable candidates once testing the solubility of 4-aminobenzyl alcohol and phosphorus tribromide separately. In DMF, once the two reagents were combined, precipitation of 4-aminobenzyl alcohol rapidly occurred. The use of a THF solvent showed no precipitation, but analysis of the reaction mixture showed no product formation.

It was then attempted to convert the hydroxyl group of 4-aminobenzyl alcohol to a sulfonyl group, which act as excellent leaving groups for a wide variety of reactions. The reaction of 4-aminobenzyl alcohol with methane sulfonic acid and diisopropylethylamine (DIPEA) was not successful and subsequent attempts to instead install a tosyl group using toluene sulfonic acid resulted in the same outcome, where starting material remained unreacted in all cases (Figure 44).

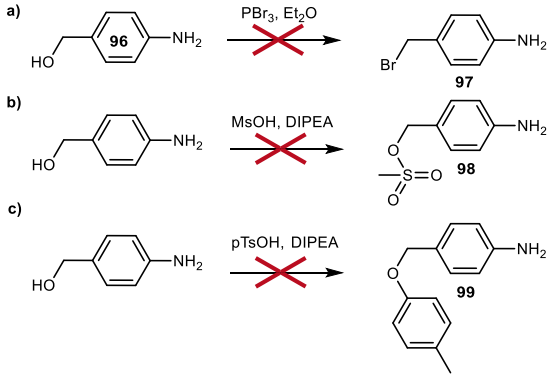

Figure 44: a) Attempted 4-(bromomethyl)aniline synthesis, b) attempted installation of a sulfonyl leaving group and c) attempted installation of a tolyl leaving group.

2.2.4 Sonogashira cross-coupling for copper(II) pyrithione HDAC inhibitors

The challenges correlated with synthesising a compound with a suitable leaving group for installation of an azide led to consideration of using the Sonogashira cross coupling reaction with the available Cu(II) pyrithione alkyne complex **80** (Figure 39).

Owing to the fact that molecule **69**, previously synthesised as described in **Section *2.2.1***, is an aryl bromide, it appears an ideal candidate for a Sonogashira cross-coupling reaction with **80**. The full synthetic route proposed to target **100** is shown in Scheme 7.

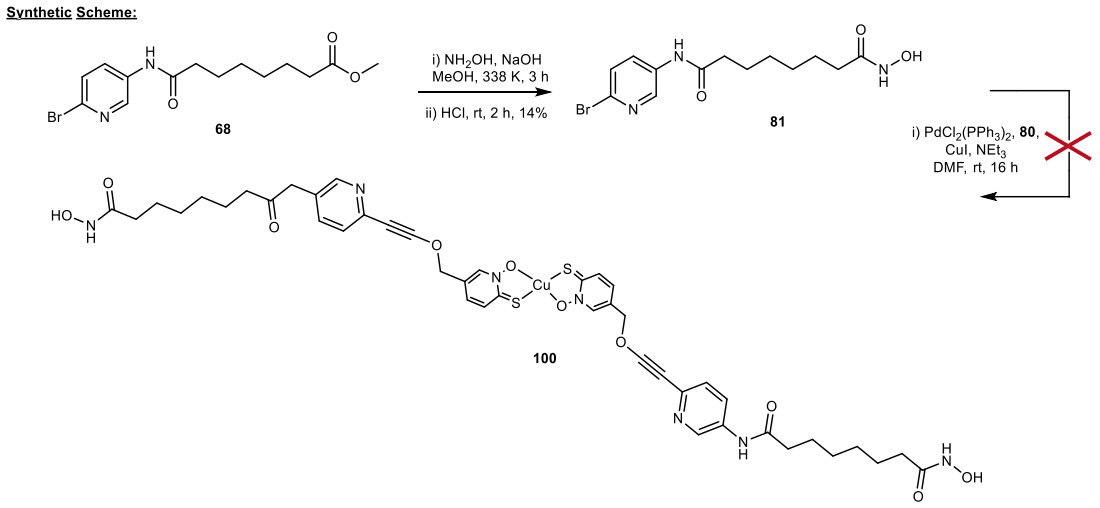

*Scheme 7: Synthetic route for the Sonogashira cross-coupling reaction of **81** with **80** to form copper(II) pyrithione HDAC inhibitor, **100**.*

The conversion of the methyl ester, **68**, to the desired hydroxamic acid, **81**, was routinely achieved via reaction of **68** with 50 % hydroxylamine solution at pH 11 in methanol. The Pd-precatalyst chosen was $Pd(PPh_3)_2Cl_2$, which was activated in-situ by the addition of a triethylamine base to $Pd(PPh_3)_2$. It was hoped that **81** would undergo oxidative addition to $Pd(PPh_3)_2$ via cleavage of the aryl carbon-bromine bond. Concurrently, the Cu(I) halide salt, CuI, will react with **80**, to complete the transmetallation step. Subsequent reductive elimination from the transmetallation product would hope to produce our first example of a copper(II) pyrithione HDAC inhibitor, **100**. Mass spectrometric analysis of the reaction mixture and resulting solid post-workup showed no evidence of **100**, or any copper containing species other than the alkyne pyrithione complex. Thin layer chromatography (TLC) also did not suggest the formation of any new species in the reaction mixture. The presence of the copper(I) co-catalyst can lead to homocoupling of alkyne derivatives in the reaction if the conditions are not completely inert. Hence, a copper-free version of the Sonogashira reaction was also attempted using the same substrates and pre-catalyst, yet no transformation was observed through TLC or mass spectrometry.

The individual steps of the catalytic cycles for the Sonogashira cross-coupling reaction are hugely influenced via the steric and electronic properties of the substrates, which offer plausible explanations as to why this route was not viable. For example, the oxidative addition step is promoted by electron-withdrawing groups at the aryl halide, where the presence of the pyridine nitrogen alone may not be sufficient for cleavage of the aryl carbon-bromine bond. Another likely cause for the failure of this reaction lies in steric influences during the transmetallation step. Complex **80** invokes incredible steric bulk around the Pd(II) centre, which although

facilitates efficient reductive elimination of the product **100**, results in an unfavourable transmetallation step due to the steric strain around the Pd(II) centre - especially since **81** also possesses a sterically demanding alkyl component. Finally, the hydroxamate functionality can bind to the Pd catalyst, which ceases any catalytic activity and thus sops the conversion desired.

An alternative route that may offer greater success is cross-coupling **81** and the pyrithione ligand of **80** prior to formation of the copper(II) complex. It must be considered that the 'naked' pyrithione ligand may dimerise and form disulfide bridges which will overly complicate the synthesis.

2.2.5 Copper(II) complex with a (N,O) donor SAHA analogue

Moving away from the preparation of a copper(II) pyrithione based HDAC inhibitor, another ligand synthesised in the Walton Group offered a potential route to a second copper(II) HDAC inhibitor. The ligand **103** previously synthesised is shown in Scheme 8, where this SAHA analogue was found to chelate to a ruthenium(II) metal centre. The chelating binding mode of this ligand with ruthenium occurs through (*N*,*O*) donor atoms as illustrated below in **Section *2.3.1*** (Figure 47), which is driven by the formation of a stable six-membered ring upon (*N*,*O*) binding. It is proposed that this ligand may also show affinity to copper(II), so a synthetic route to our target complex, **104**, was proposed as shown in Scheme 8.

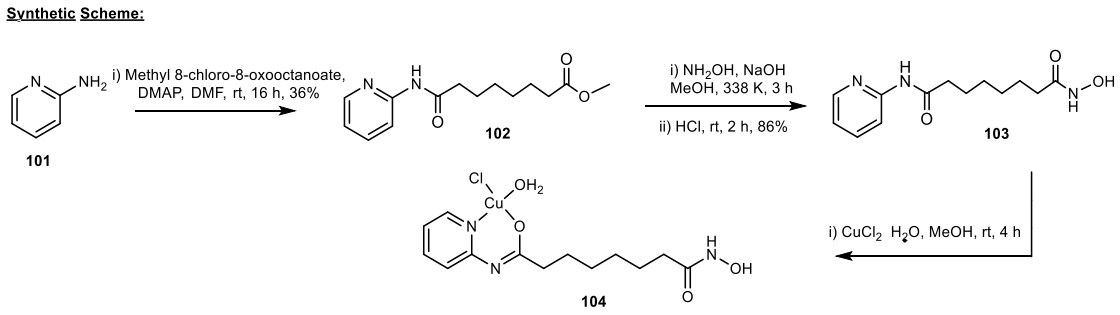

*Scheme 8: Synthetic route for a copper(II) dual-action HDAC inhibitor, **104**, incorporating SAHA analogue, **103**.*

The synthesis of **102** and **103** followed analogous procedures described for compounds **53** and **48**, respectively, and their formation was confirmed by ^{1}H-NMR spectroscopy and mass spectrometry. It was anticipated that **104** would be formed readily upon reaction with copper(II) chloride dihydrate, however, no conversion was observed upon analysis of the reaction mixture by mass spectrometry. It was suspected that loss of the amide ^{1}H of **103** was limiting the formation of **104**, hence the reaction was repeated with 1 equivalent of triethylamine base, but again, no complex was observed. Referring to the synthesis of the copper phenanthroline complex **54** in **Section *2.1.1***, it was clear that formation of **54** proceeded reluctantly, with

specific combinations of reaction scale, temperature, and copper(II) chloride dihydrate equivalence dictating the success of complex formation. Therefore, an investigation into the reaction scale, temperature and equivalence dependence was repeated for the synthesis of **104**. The solvents used were either methanol or water, with the use of triethylamine and sodium hydroxide bases, respectively. Unfortunately, these studies did not display any mass spectrometric evidence to indicate that **104** had been synthesised and thus this route was not pursued further. Considerations on why **104** did not form possibly lie in the ligand geometry around the copper(II) centre. Alluding to the *p*-cymene ruthenium complex below in Figure 47, which incorporates the same ligand, the geometry about the ruthenium(II) metal centre in the piano stool complex is described as pseudo-octahedral, or tetrahedral considering the p-cymene capping group occupying a single coordination site. The tetrahedral geometry suggests that the bite angle of **103** about the ruthenium(II) centre is around 109.5°, which is significantly larger than the 90° required for formation of a square planar copper(II) complex. Furthermore, the internal bond angles within a 6-membered ring adopting a chair conformation, which is formed upon chelation of **103** to the ruthenium(II) centre, are also 109.5°. The larger size of the ruthenium(II) ion perhaps allows greater freedom in ligand geometry and reduced steric interactions between neighbouring ligands when compared with copper(II) metal centres, hence demonstrates why **103** is an unsuitable ligand for copper(II) complexation. However, if the *p*-cymene complex is considered pseudo-octahedral, a 90° bite angle is needed, the same as for **104**. Therefore, the key reason may be due to the strength of the bond between the metal centre and pyridine nitrogen. The ruthenium-pyridine bond is strong due to good sigma donation, but ruthenium is a stronger back donor into the π^* orbitals of pyridine than copper, resulting in stronger metal-ligand bonding and thus more favourable complex formation.

2.2.6 Histone deacetylase enzyme inhibition assay

Despite the lack of success in designing a suitable copper(II) pyrithione HDAC inhibitor, it was decided to still test **73** and **75**, shown again in Figure 46, to explore whether the pyrithione functionality could effectively inhibit the HDAC enzyme, and if its potency would be improved when incorporated into a copper(II) complex. The results of the HDAC enzyme inhibition assay are shown in Figure 45, in which two concentrations of 10 μM and 1 μM were tested for each compound.

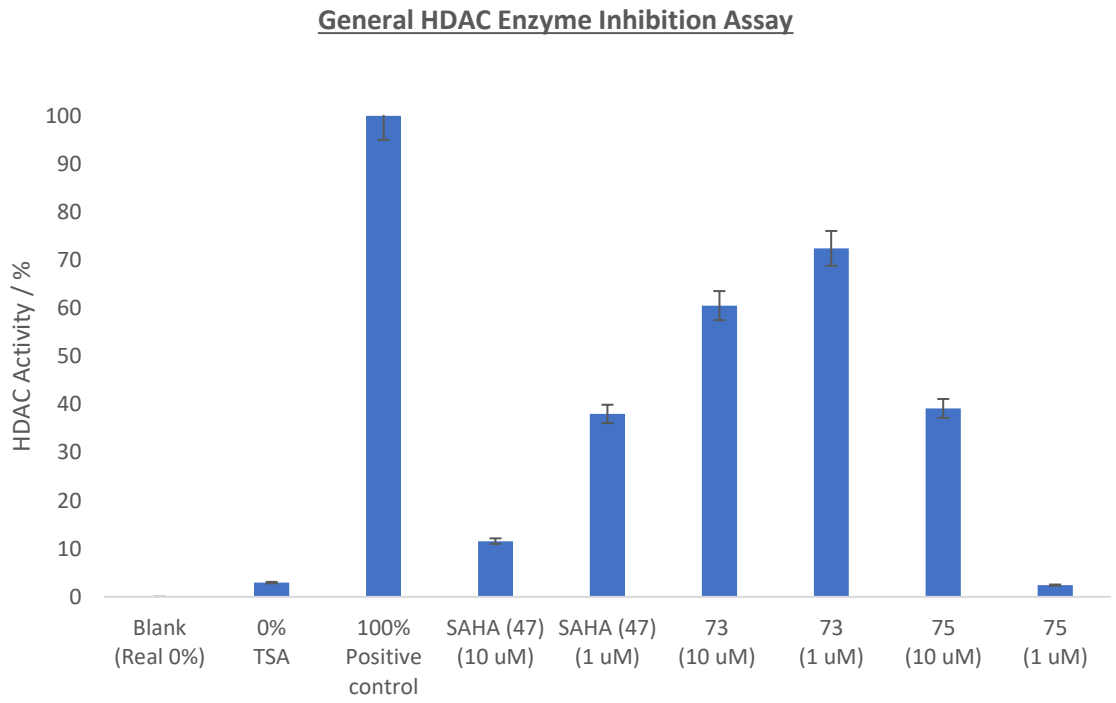

*Figure 45: Two-point general HDAC inhibition assay results at concentrations 10 μM and 1 μM for SAHA (**47**), **73** and **75**.*

The pyrithione ligand, **73**, does not show an improvement on clinically approved SAHA, although, complexation of this ligand to copper(II) to form 75, does appear show increased HDAC inhibition relative to the free ligand. The data obtained for **75** is of concern though, since the 1 μM concentration shows significantly greater HDAC inhibition than 10 μM, signifying potential precipitation of the complex at higher concentrations. Regardless, further repeats of this data are needed to identify the anomaly.

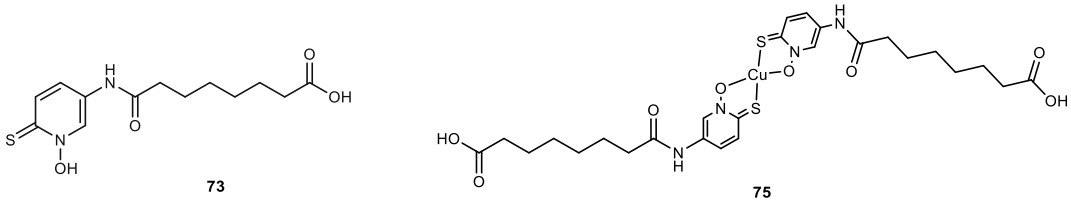

*Figure 46: Synthesised complexes **73** and **75** used for HDAC testing.*

2.3 Ruthenium piano stool complexes

2.3.1 Synthesis of ruthenium(II) piano stool complexes

The associated problems encountered with synthesis of a second copper(II) HDAC inhibitor, and the promising HDAC inhibition profile of the *p*-cymene ruthenium(II) complex in Figure 47, led to the proposed synthesis of a library of the ruthenium(II) complexes incorporating ligand **103**. Potential has already been realised in ruthenium(II) HDAC inhibitors generally, but the

selectivity of the *p*-cymene ruthenium(II) complex to HDAC1 offers an exciting prospect for development of specific HDAC inhibitors. The synthetic protocol used for the *p*-cymene ruthenium(II) complex is shown in Figure 47, where subsequent complexes were synthesised following a similar procedure. Unpublished complex **105** had previously been synthesised by a Masters student within the Walton Group. It was decided to synthesise a library of analogous complexes with varying capping arenes, in order to investigate any changes in HDAC inhibitory activity or selectivity.

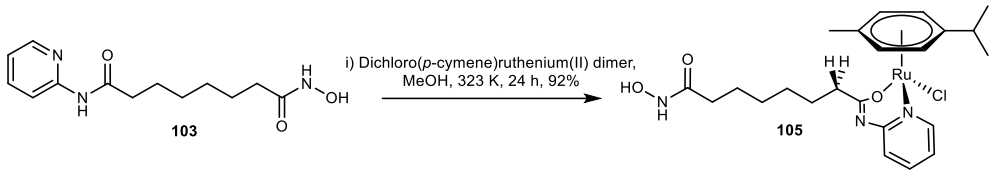

Figure 47: *Synthesis of p-cymene ruthenium(II) complex,* ***105****, incorporating the SAHA analogue,* ***103****, previously reported by the Walton Group.*

The reaction of ruthenium dichloride dimers, such as $[(p\text{-cymene})RuCl_2]_2$, with suitable lewis bases to form monometallic adducts are transformations frequently encountered. However, the novelty of this complex lies in the unexpected bidentate coordination mode of **103** – which has proven to be a very effective HDAC1 inhibitor once incorporated into a ruthenium(II) complex. The coordination mode of **103** has been elucidated through NMR spectroscopy, where H^x and $H^{x'}$, as shown in Figure 48 are diastereotopic and hence magnetically inequivalent upon complex formation due to the conformational restriction upon forming a 6-membered ring about the ruthenium(II) centre. Heteronuclear Single Quantum Coherence (HSQC) experiments revealed that the diastereotopic ^1H's are connected to the same carbon, whilst Heteronuclear Multiple Bond Correlation (HMBC) experiments demonstrate that the same correlations exist between carbons situated further than one bond away from the diastereotopic ^1H's. Tautomerism of the amide bond to the corresponding imidic functional group is thought to be driven by the formation of a stable 6-membered ring upon chelation to the ruthenium(II) centre, where the oxygen atom of the imidic functional group is a negatively charged two-electron donor, satisfying the charge requirements for an overall neutral 18-electron ruthenium(II) complex. It was initially expected that **103** would bind through the pyridine nitrogen only, however, displacement of a chloride ligand to enable bidentate coordination can be simply rationalised through the chelate effect and subsequent favourable entropic effects of this phenomenon.

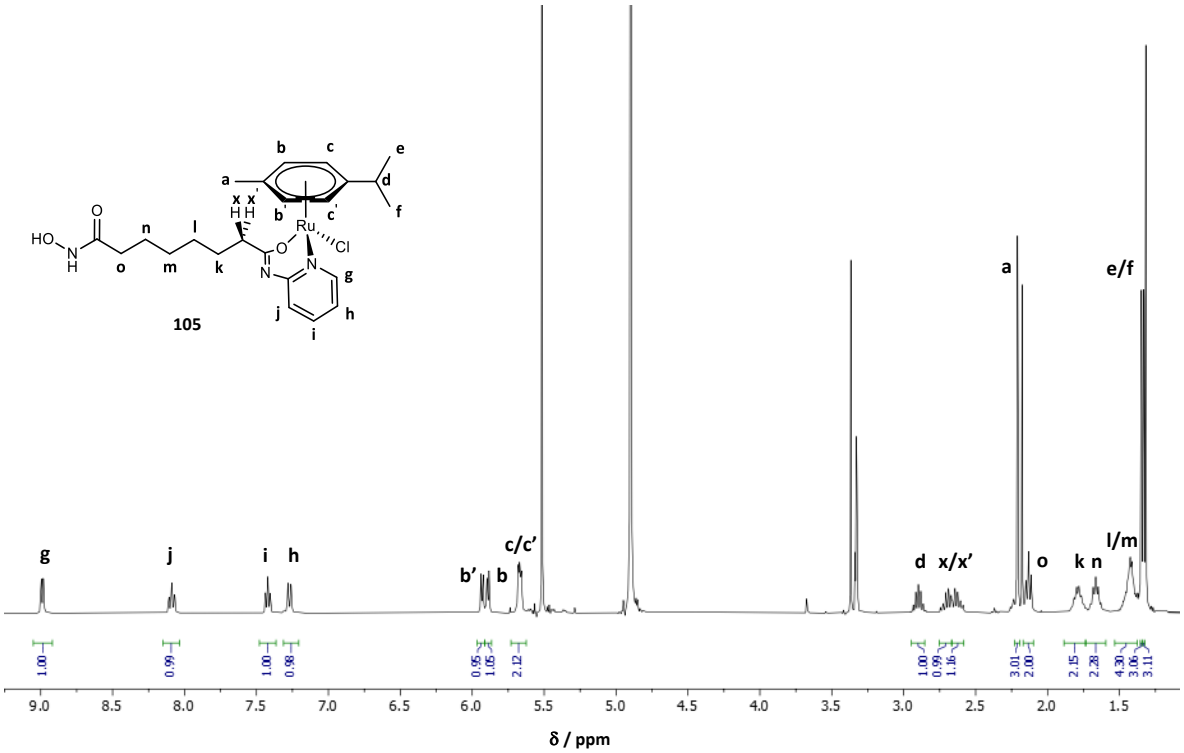

*Figure 48: Assigned ^{1}H NMR spectrum of ruthenium(II) p-cymene complex, **105**, in MeOD. The diasterotopic ^{1}H's $H^{x/x'}$ indicate the bidentate coordination of ligand **103**.*

2.3.2 Expanding the ruthenium(II) complex library

It was desirable to synthesise derivatives of the p-cymene ruthenium(II) complex for a structure-activity-relationship (SAR) investigation, where reaction of ligand **103** with different ruthenium(II) dichloride dimers would lead to novel complexes that differ in their capping arene group. A few ruthenium(II) dichloride dimers are available commercially, however, the Walton Group have also synthesised novel ruthenium(II) dichloride dimers which are suitable for use in this study.[99] A library of 11 new ruthenium(II) complexes were synthesised following the scheme in Figure 49. The library shown in Figure 49 includes variation in substituent and branching of the capping arene group. All complexes were fully characterised by multinuclear NMR and mass spectrometry as described in **Section *2.3.1,*** where all complexes in the library showed the same diastereotopic protons, showing that variation in the capping arene does not alter the coordination mode of the ligand **103**. It's important to highlight that the synthesis of these compounds proceeded without any unsuccessful instances when subjected to the dimer, which demonstrates that given more time, the scope of this library could have been extended even further and structure-activity relationships probed in detail.

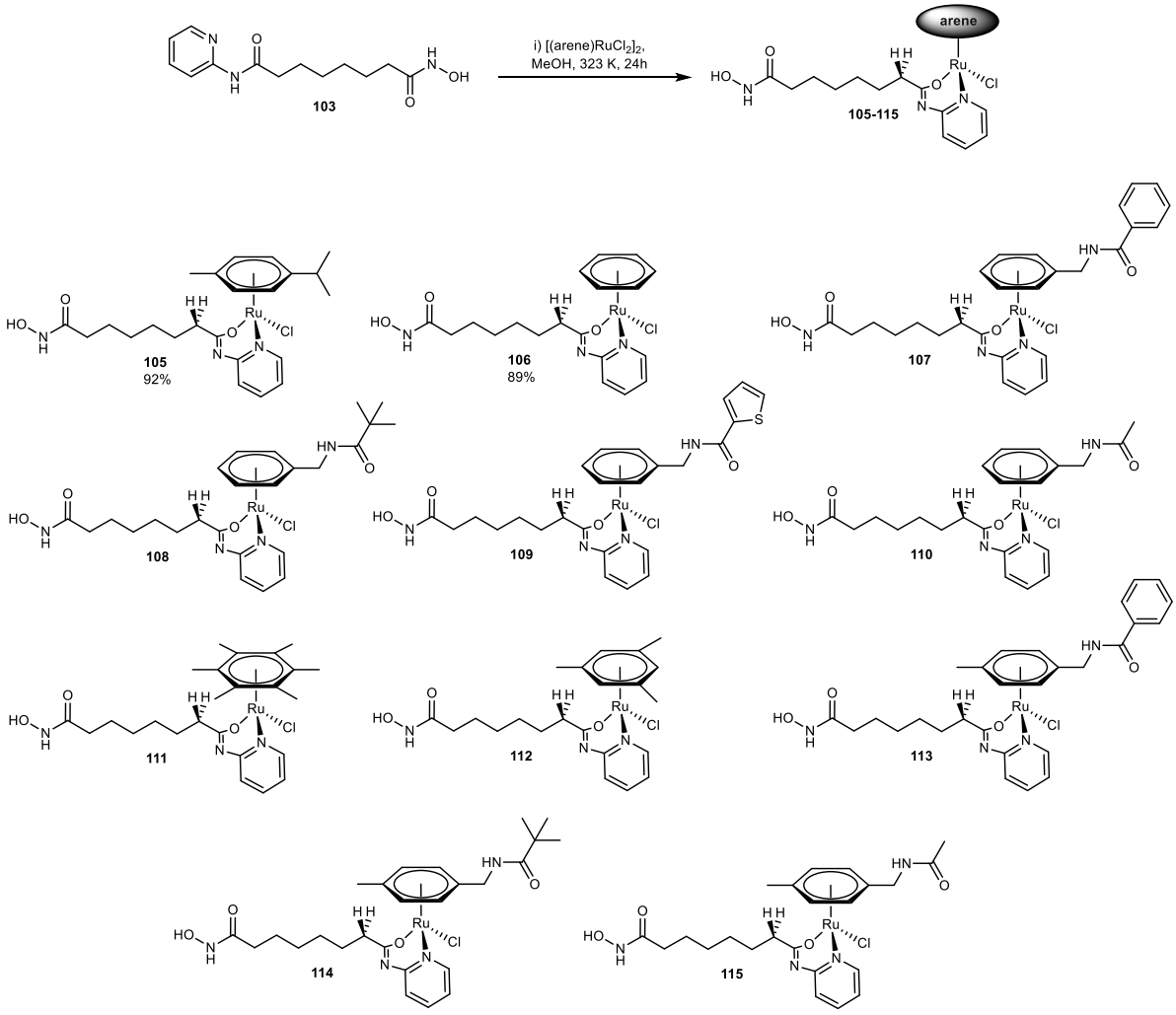

Figure 49: Library of 11 new ruthenium(II) complexes incorporating SAHA analogue, ***103****.*

Through synthesising these ruthenium(II) complexes with differing capping arene groups, it is hoped to investigate the steric and electronic effects of these substituents on HDAC isoform selectivity since the outer surface of the catalytic pocket is unique to each HDAC isoform. For example, the steric bulk of the head group increases in the order **110** < **109** < **107** < **108**, which may result in poorer fitting of the inhibitor into the HDAC pocket as the steric hinderance increases, or fitting that is tuned in favour to a specific isoform. The electronic properties between the complexes also differ, where the phenyl and thiophene substituents can exhibit π-interactions with amino acids possessing aromatic substituents on their side chains, which may improve binding and selectivity to the HDAC isoforms. The study by Walton *et al.* described in **Section 1.4**, comments on the idea that more bulky and more hydrophobic groups are likely provide more favourable interaction with the catalytic channel rim of HDAC6, which is known to be wider and shallower than other HDAC. Following this, significant variation in the capping

groups was included for the library shown in Figure 49, such that selectivity could be tested for a variety of HDAC isoforms since their catalytic channel and binding site vary greatly.

2.3.3 Beyond ruthenium(II) metal centres

While Ru complexes are commonly explored as anticancer complexes, Rh(III) and Ir(III) complexes are less well studied. Dichloride dimers of rhodium(III) and iridium(III) are commercially available, and so $[Cp^*RhCl_2]_2$ and $[Cp^*IrCl_2]_2$ were reacted with **103**, respectively (Figure 50). The corresponding reactions did not proceed with such ease as the ruthenium(II) dichloride dimers. For example, the corresponding rhodium(III) complex did not show the expected diastereotopic ^{1}H's in the ^{1}H NMR spectrum for a bidentate coordination mode, and instead suggested a monodentate mode of **103** binding, which occurs through the pyridine nitrogen. The suggested structure of the rhodium(III) complex, **116**, is shown in Figure 51, where mass spectrometry of the sample shows a molecular ion peak at *m/z* 557.17 which supports a molecular formula of $C_{23}H_{36}ClN_3O_4Rh$. Aside from the monodentate binding mode of **103**, **116** differs in the fact that it is a positively charged complex, where a single water molecule is bound to the rhodium(III) centre. This charged species would certainly be more readily detectable in the mass spectrometric experiment than the neutral dichloride equivalent (in which the bound H_2O is replaced by Cl^-), hence, elemental analysis is needed to determine the identity of the coordinating ligands around the rhodium(III) centre. It is intriguing that **103** no longer adopts a bidentate mode of coordination to the rhodium(III) centre, considering the remarked similarities between ruthenium(II) and rhodium(III), however, the increased oxidation state, and resulting contraction in ionic radii, may rationalise this behaviour.

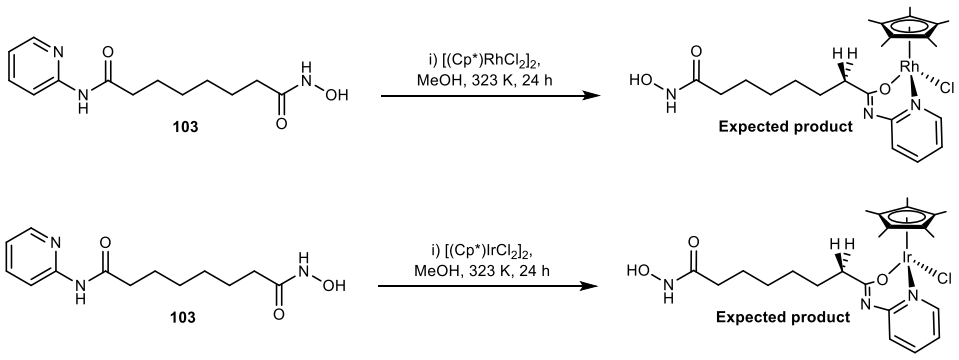

*Figure 50: Expected rhodium(III) and iridium(III) complexes upon reaction of their dimer precursors with **103**.*

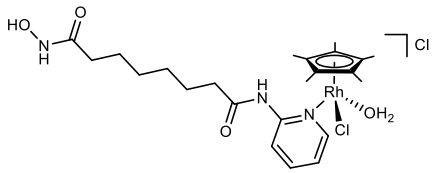

116

Figure 51: Rhodium(III) suspected mass spectrometric adduct, ***116****.*

The identity of the iridium(III) complex proved even more ambiguous since the mass spectrometric data revealed a molecular ion peak at *m/z* 745.46, with an isotope pattern supporting two iridium atoms as part of the complex. No complex has yet been fitted to the data to suggest a suitable molecular formula, however, the ^{1}H NMR spectrum shows evidence of a monodentate mode of **103** coordination. Again, elemental analysis must be exploited to elucidate the identity of this complex, especially with the likelihood of mass spectrometric adducts complicating the analysis.

2.3.4 Histone deacetylase enzyme inhibition assay

With ruthenium complexes **105**-**115** in hand, it was hoped to conduct a general HDAC inhibition assay, as well as HDAC1 specific assays, to investigate any structure-activity relationships across the ruthenium(II) complexes synthesised. Complexes **107**-**115** required purification through high-performance liquid chromatography (HPLC) due to the limited supply of dichloride ruthenium(II) dimer precursors, but unfortunately, the time constraints of the project did not allow for HPLC purification of the complexes prior to the HDAC assay, hence, only p-cymene capped complex **105** and benzene-capped complex **106** were tested for activity in a generic HDAC inhibition assay. The results of the general assay are shown in Figure 53.

.

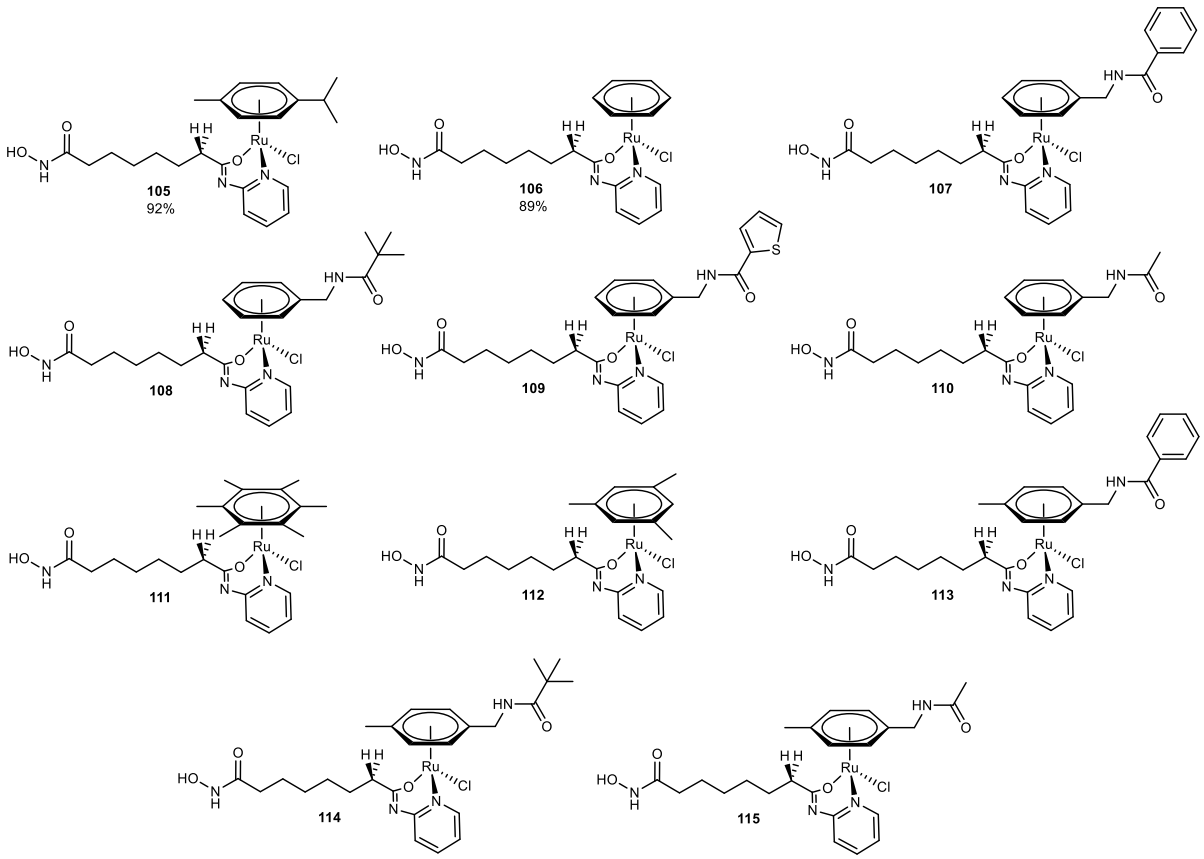

*Figure 52: Library of 11 new ruthenium(II) complexes, **105-115**, incorporating SAHA analogue, **103**.*

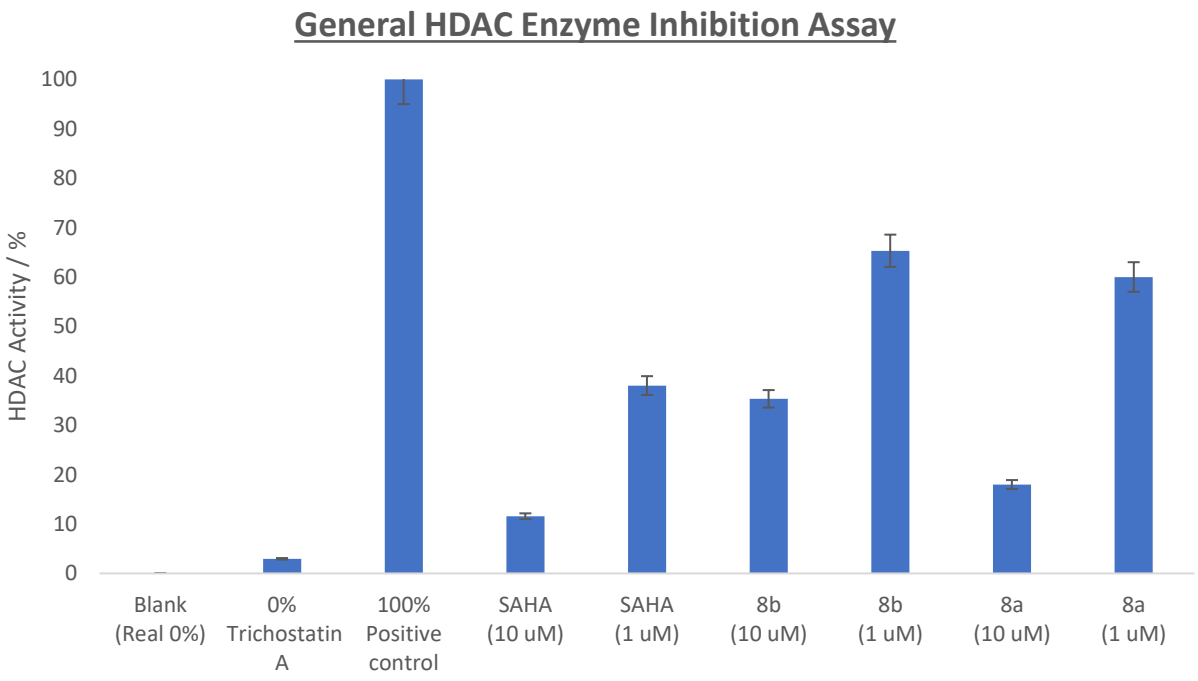

*Figure 53: Two-point general HDAC inhibition assay results at concentrations 10 μM and 1 μM for SAHA (**47**), **106** and **105**.*

It is evident that neither **105** nor **106** show HDAC inhibition that is an improvement on the clinically approved SAHA. However, the inhibition properties of **105** appear improved to that of **106**, particularly at the higher concentration of 10 μM, suggesting that the alkyl substituents on the arene ring of **105** influence the binding of the inhibitor to the HDAC enzyme. This result highlights the importance of testing the other Ru complexes in the library to determine whether any of the capping arenes lead to improved activity. Although the results for **106** may seem disappointing, this complex was synthesised to investigate its HDAC1 isoform selectivity compared to **105**, where these studies are currently in progress for the ruthenium(II) library shown in Figure 52.

3 | CONCLUSIONS & FUTURE WORK

At the outset, this project was designed to harness the synergies between SAHA-based HDAC inhibitors and copper(II) complexes, to develop a dual-action HDAC inhibitor library. As the project developed, it became desirable to synthesise a library of piano stool ruthenium(II) complexes in attempt to design more selective HDAC inhibitors, due to the evidence that selectivity towards specific HDAC isoforms can improve the overall therapeutic effect.

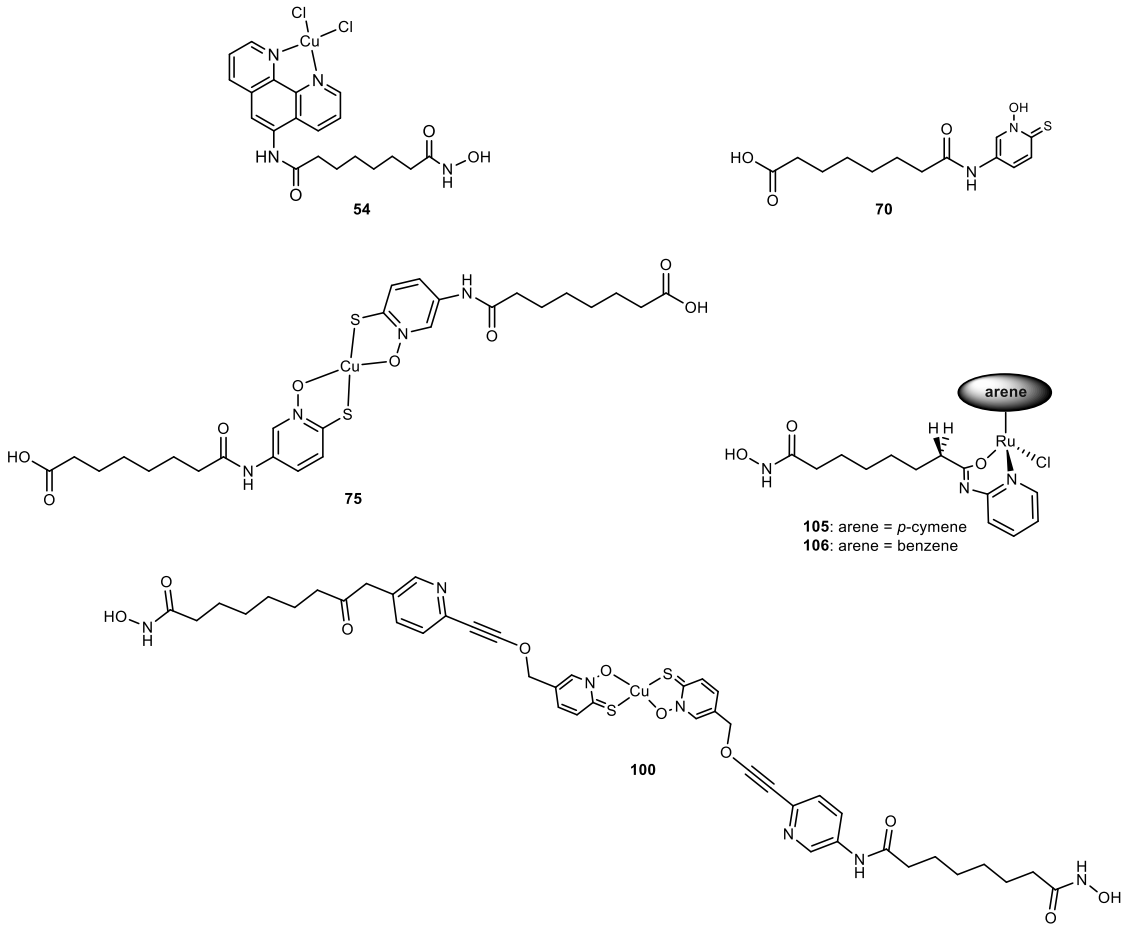

Figure 54: Summary of the key compounds discussed in this report.

A successful example of a dual-action copper(II) HDAC inhibitor was synthesised, namely dichloro(N^{20}-hydroxy-N^{11}-(1,10-phenanthrolin-5-yl)octanediamide)copper(II) (**54**) (Figure 54). Complex **54** was shown to possess enhanced HDAC inhibitory properties compared to SAHA, with an IC_{50} = 0.32 ± 0.02 µM compared to IC_{50} = 0.70 ± 0.05 µM for SAHA (**47**). Further studies are needed to explore if such complex is selective to specific HDAC isoforms, since this was not able to be investigated in the project timescale.

Control studies using the ligand **48** and $CuCl_2$ alone support the fact that the synergistic effects of copper(II) and the SAHA functionality in **54** lead to the enhanced inhibitory potency, however,

the underlying reason is largely unexplored. The rationale behind incorporating copper(II) was to harness its DNA targeting and ROS generating properties, therefore, cell cytotoxicity assays must be completed to see if copper(II) inclusion has the intended effect.

Paramagnetic NMR and IR spectroscopy studies successfully elucidated the ligand chemoselectivity of **54**, but the conclusive coordination environment of **54** remains unclear since the suspected chloride ligands are not present in the detected mass spectrometric adducts.

Although we have sufficient evidence to suggest that copper(II) is bound via the 1,10-phenthroline head group, there is still little information to support the true coordination environment of copper(II) in **54**. Electron Paramagnetic Resonance (EPR) is a well-established analytical technique to probe species with unpaired electrons. The technique is analogous to NMR spectroscopy, but the spins excited in the presence of a magnetic field are those of the electrons instead of the atomic nuclei. The larger magnetic moment of an electron compared to a nucleus also results in a greater population difference between the energy levels probed in the experiment, leading to this technique being approximately 1,000 times more sensitive than NMR spectroscopy. EPR spectroscopy has been routinely used for investigation of square planar copper(II) complexes, with interesting studies conducted in both solution and solid states. Although not carried out yet for complex **54**, solution state EPR could be used in future to provide useful information to show how many nitrogen and chlorine atoms are surrounding the copper(II) centre through the distinct splitting pattern of the EPR signal.

Most excitingly, the anisotropy associated with the J-coupling and chemical shift values, termed hyperfine coupling and g-value in EPR, respectively, show distinct correlations for copper(II) square planar complexes in the solid state. These correlations, which are a result of the orientation dependence of the hyperfine and g-values, can be used to identify the atoms coordinating the copper(II) centre. Such experiment would have proved very useful in the analysis of **54** since anisotropic EPR experiments would have elucidated the electronic environment of **54** and will be carried out in future work.

As additional future work, a subset of X-ray Absorption (XAS) spectroscopy, Extended X-ray Absorption Fine Structure (EXAFS), is another technique that can provide information on the identity of the atoms coordinating a metal centre - provided the coordinating atoms have a molecular weight larger than ^{7}Li. The basis of this technique involves an ionisation process in which an X-ray beam is applied to an atom, copper(II) in the case of **54**, which causes ejection of

a core electron. The ejected photoelectron is considered a wave, which interacts with nearby atoms, treated as point scatterers, in which these atoms scatter back the photoelectron wave, where constructive and destructive interference between the back scattered waves gives a unique pattern in the X-ray absorption spectrum, that can be interpreted to give the identity of the nearby atoms. A typical XAS spectrum in shown in Figure 55, where the EXAFS region would reveal which atoms are coordinating the copper(II) centre for **54** since ^{14}N and $^{35/37}Cl$ are sufficiently high in relative atomic mass to cause this back scattering phenomenon.

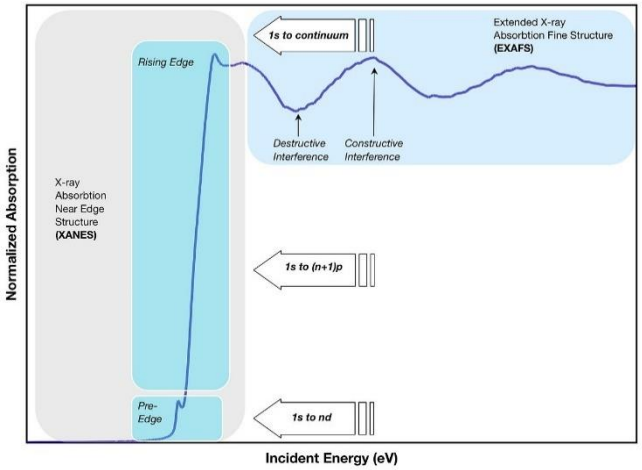

Figure 55: Generic X-ray absorption spectrum displaying the XANES and EXAFS region.[118]

As suggested in **Section *2.1.3***, EXAFS and solution/solid-state EPR would provide valuable insights into the copper(II) coordination sphere, although, evaluating a plethora of crystallisation techniques to gain suitable crystals for X-ray crystallographic analysis would provide the greatest information. This would also be valuable to see if the unusual solution-state alkyl conformation for **48** discussed in **Section *2.1.1*** is preserved in the solid-state/**54**.

Owing to the impressive anticancer activity, likely due to Cu(I)/Cu(II) redox activity, a pyrithione copper(II) HDAC inhibitor target was then pursued. Difficulties in these experiments were a result of extremely low yields of **70** and the inherent instability of the pyrithione moiety to the alkyl linker. Despite this, complex **75** was synthesised which has a similar structure to target **72**, but conversion of the carboxylic acid group to a hydroxamic acid could not be achieved since **75** was poorly soluble in all suitable solvents (see **Section *2.2.1***).

The inherent instability of the pyrithione moiety to the alkyl linker became notoriously challenging when it was attempted to use the pyrithione ligand itself as an HDAC zinc-binding group, due to previous reports of excellent HDAC inhibition with pyrithione zinc-bindng groups.

Sonogashira cross-coupling and 'click' reactions were attempted routes in expanding the copper(II) HDAC inhibitor library to synthesise **83**/**89** and **100**, respectively. The 'click' route was problematic due to the failure in incorporating a suitable leaving group to subsequently install the required azide functionality.

Further investigations into the Sonogashira reactions reported in **Section *2.2.4*** would be of value since cross-coupling the ligands prior to copper(II) complex formation could result in successful synthesis of **100**. In addition to this, cross-coupling reactions are especially sensitive to reaction conditions and require significant optimisation which was not plausible to investigate in detail at the time of this research.

The project progressed to design selective ruthenium(II) piano-stool HDAC inhibitors due to the HDAC1 selectivity shown for *p*-cymene ruthenium(II) complex, **105**. This synthetic route proved successful where 11 new ruthenium(II) piano stool complexes were synthesised as shown in Figure 52, although only **105** and **106** were purified. The time in which these complexes were synthesised resulted in general HDAC testing of **106** only. Studies are currently ongoing to quantify the general and selective HDAC inhibition of these new complexes. Exploring a structure-activity-relationship will be essential in tuning the design of such complexes and developing a novel, potent and selective HDAC inhibitor. The reaction of the ruthenium dimer with **103** to form the ruthenium(II) piano stool complex is overall very successful - expansion of the precursor dimer library should be pursued to continue building upon this exciting library ruthenium(II) piano stool complexes.

Overall, this project provides valuable insights into the challenges of synthesising copper(II) dual-action HDAC inhibitors and demonstrates the value in the inclusion of copper(II) once the target is achieved. The HDAC1 selectivity of **105** provides a promising future for the rest of the ruthenium(II) piano stool library.

4 | EXPERIMENTAL

4.1 General methods

Commercially available reagents were purchased from Merck Life-sciences, Fluorochem and Fischer Scientific and were used as received from suppliers. Solvents were laboratory reagent grade and dried using an appropriate drying agent when required. Reactions requiring anhydrous conditions were carried out under an atmosphere of dry nitrogen using Schlenk-line techniques. Thin-layer chromatography was carried out on silica plates (Merck 5554) or neutral alumina plates (Merck Art 5550) and visualised under UV (254/365 nm) irradiation. NMR spectra (^{1}H, ^{13}C {^{1}H}) were recorded on Bruker Advance (III)-400 spectrometer (^{1}H at 400.130 MHz, ^{13}C {^{1}H} at 100.613 MHz), or a Varian VNMRS-600 spectrometer (^{1}H at 600.130 MHz, ^{13}C {^{1}H} at 150.903 MHz). Spectra were recorded at 295K in commercially available deuterated solvents and referenced internally to the residual solvent proton resonances. Electrospray, Atmospheric Pressure and high-resolution mass spectrometry were performed using SQD and QToF mass spectrometer with Acquity UPLC.

4.2 Histone deacetylase inhibition assay procedure

Sigma-Aldrich fluorometric HDAC assay kit components (https://www.sigmaaldrich.com/GB/en/product/sigma/cs1010) were first diluted to appropriate concentrations using the supplied assay buffer, with the well contents summarised in Table 3. The known inhibitor, Trichostatin A (TSA), was used as the 0% HDAC activity control and no inhibitor was used for the 100% HDAC activity control. The candidate inhibitors were dosed at 10 µM and 1 µM concentrations. Nuclear extract from human cervical cancer (HeLa) cells was used as the HDAC source. The substrate utilised was a substituted peptide with an acetylated lysine residue with a bound fluorescent group, which later developed to a fluorophore. Following the mixing of the buffer, HeLA extract, inhibitor and substrate, in separate triplicate wells, the 96 well plate was incubated at 37 °C for 30 minutes. Subsequently, developer was added to each well and left to act on the deacetylated substrate at room temperature for an additional 15 minutes. Deacetylation by the HDAC enzymes sensitised the substrate to the developer, which consequently generated a fluorophore. Relative fluorescence emission intensity was measured using a Synergy H4 Fluorescence Plate Reader (λ_{ex} = 360 nm, λ_{em} = 460 nm). Average fluorescence values were calculated from the experimental triplicate repeats.

$$HDAC\ Activity\ (\%) = \frac{F_{sample} - F_{blank}}{F_{100\%} - F_{blank}}$$

Equation 1: Formula used to calculate % HDAC activity with F_{sample} = fluorescence of the tested inhibitor, F_{blank} = fluorescence of the blank and $F_{100\,\%}$ = fluorescence of the positive control.

Table 3: Volumes in µL of the HDAC assay well contents.

	Buffer	HeLa Extract	Inhibitor	Substrate	Developer
Blank	50	-	-	50	15
0 % (TSA)	50	5	5	50	15
100 % (control)	45	5	-	50	15
Inhibitor	40	5	5	50	15

In order to investigate the candidate inhibitors' potency through IC_{50} curves, the methodology outlined above was followed, with a larger range of concentrations investigated as outlined in **Section *2.1.4***. Each concentration for each inhibitor was performed in triplicates on a 96 well plate. IC_{50} values were calculated from the x-axis value at 50% enzyme activity. A more positive intercept reveals a larger IC_{50} value, which means a requirement for a greater concentration of the inhibitor to get 50 % inhibition, signifying lower potency, as explained in **Section *2.1.4***.

4.3 General method for High Performance Liquid Chromatography purification

The samples were purified using an InterChim PuriFlash purification system equipped with a Waters XBridge C18 (19 x 100 mm, 5um). Separation was achieved using gradient elution at a flow rate of 17 ml/min starting with 10% water with 0.1% methanol, 90% DCM to 100% DCM over 10 minutes then held at 100% DCM for 5 minutes. A diode array detector monitored the absorption of the eluent and fractions were collected when a threshold of 5 mAU was achieved at 260 nm.

4.4 Synthetic methods

Methyl 8-((1,10-phenanthrolin-5-yl)amino)-8-oxooctanoate (53)

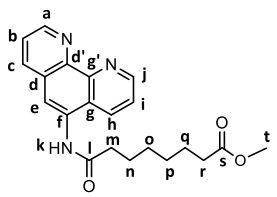

53

1,10-Phenanthrolin-5-amine (**52**) (300 mg, 0.82 mmol), methyl 8-chloro-8-oxooctanoate (**117**) (0.17 mL, 1.16 mmol) and 4-dimethylaminopyridine (**118**) (30 mg, 0.25 mmol) were dissolved in DMF (6 mL) and stirred for 16 h at room temperature under an inert atmosphere. The volume of solution was reduced under vacuum by 80% and the solution added dropwise to a stirring

solution of Et_2O (20 mL), where upon cooling the solution to 198 K, an orange precipitate formed. The remaining solution was decanted and the orange precipitate dissolved in $CHCl_3$ (10 mL) and washed with H_2O (3 x 20 mL). The organic layer was separated, concentrated under reduced pressure, and dried under high vacuum to afford the *title compound* as an orange oil (26 mg, 44%).

δ_H (400 MHz, MeOD) 9.14 (1H, dd, $^3J_{HH}$ = 4.34 Hz, ^4J = 1.63 Hz, H^j), 9.07 (1H, dd, $^3J_{HH}$ = 4.32 Hz, $^4J_{HH}$ = 1.72 Hz, H^a), 8.58 (1H, dd, $^3J_{HH}$ = 8.41 Hz, $^4J_{HH}$ = 1.63 Hz, H^h), 8.44 (1H, dd, $^3J_{HH}$ = 8.16 Hz, $^4J_{HH}$ = 1.72 Hz, H^c), 8.11 (1H, s, H^e), 7.84 (1H, dd, $^3J_{HH}$ = 8.41 Hz, $^3J_{HH}$ = 4.34 Hz, H^i), 7.78 (1H, dd, $^3J_{HH}$ = 8.16 Hz, ^3J = 4.32 Hz, H^b), 3.68 (3H, s, H^t), 2.63 (2H, t, $^3J_{HH}$ = 7.48 Hz, H^m), 2.39 (2H, t, $^3J_{HH}$ = 7.40, H^r), 1.85 (2H, m, H^n), 1.70 (2H, m, H^q), 1.50 (4H, m, $H^{o/p}$); ^{13}C NMR data for this compound is published[99]; *m/z* (ESI HRMS$^+$) 366.1821 $[M + H]^+$ ($C_{21}H_{24}N_3O_3$ requires 366.1818).

N^{20}-Hydroxy-N^{11}-(1,10-phenanthrolin-5-yl)octanediamide (48)

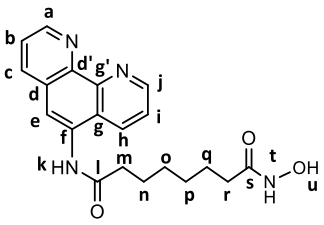

48

Methyl 8-((1,10-phenanthrolin-5-yl)amino)-8-oxooctanoate (**53**) (50 mg, 0.14 mmol) was suspended in methanol : 50% hydroxylamine solution (1:1, 7 mL) and 1M NaOH solution was added (0.5 mL) to pH 11. The mixture was stirred at 343 K for 0.5 h and left to cool to room temperature before the solution was neutralised to pH 7 by addition of 1 M HCl (approx. 10 mL). A precipitate formed on standing which was collected via filtration and dried under vacuum to give the *title compound (**48**)* as a beige solid (14 mg, 28%).

δ_H (400 MHz, DMSO-d_6) 10.35 (1H, s, H^u), 10.10 (1H, s, H^k), 9.13 (1H, dd, $^3J_{HH}$ = 4.1 Hz, $^4J_{HH}$ = 1.5, H^j), 9.04 (1H, dd, $^3J_{HH}$ = 4.3 Hz, $^4J_{HH}$ = 1.7 Hz, H^a), 8.67 (1H, s, H^t), 8.60 (1H, dd, $^3J_{HH}$ = 8.3 Hz, $^4J_{HH}$ = 1.5 Hz, H^h), 8.46 (1H, dd, $^3J_{HH}$ = 8.2 Hz, $^4J_{HH}$ = 1.7 Hz, H^c), 8.18 (1H, s, H^e), 7.84 (1H, dd, $^3J_{HH}$ = 8.3 Hz, 4.1 Hz, H^i), 7.74 (1H, dd, $^3J_{HH}$ = 8.2 Hz, $^3J_{HH}$ = 4.3 Hz, H^b), 2.53 (2H, t, $^3J_{HH}$ = 7.5 Hz, H^m), 1.97 (2H, t, $^3J_{HH}$ = 7.3 Hz, H^r), 1.69 (2H, m, H^n), 1.53 (2H, m, H^q), 1.39 (2H, m, H^o), 1.32 (2H, m, H^p); δ_C (100 MHz, DMSO-d_6) 172.86 (C^l), 169.49 (C^s), 150.41 (C^j), 149.85 (C^a), 146.22 (C^g), 144.35 (C^f), 132.24 (C^h), 136.29 (C^c), 128.59 (C^d), 125.22 ($C^{d'/g'}$), 120.56 (C^e), 123.35 (C^i), 124.04 (C^b), 36.46 (C^m), 32.84 (C^r),

25.63 (C^n), 25.56 (C^q), 25.56 (C^o), 25.63 (C^p); *m/z* (ESI HRMS$^+$) 367.1764 $[M + H]^+$ ($C_{20}H_{23}N_4O_3$ requires 367.1770).

Dichloro(N^{20}-Hydroxy-N^{11}-(1,10-phenanthrolin-5-yl)octanediamide)copper (II) (54)

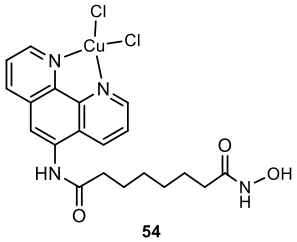

54

N^{20}-Hydroxy-N^{11}-(1,10-phenanthrolin-5-yl)octanediamide (**48**) (30 mg, 0.08 mmol) was suspended in methanol (8 mL) and added dropwise to a stirring solution of copper(II) chloride dihydrate (**28**) (11 mg, 0.04 mmol) in methanol (2 mL) and left stirring at room temperature for 2 h. The solvent was removed under reduced pressure and purified via High Performance Liquid Chromatography (HPLC) under the conditions described in **4.3**, to afford the *title complex* as a dark green solid (11 mg, 27%).

ν_{max}/cm^{-1} 3100br (NH), 2900br (OH), 1650vs and 1540vs (CO) *m/z* (ESI HRMS$^+$) 428.0906 $[M-H-2Cl]^+$ ($C_{20}H_{21}N_4O_3$ ^{63}Cu requires 428.0910).

Methyl 8-[(2-bromopyridin-3-yl)amino]-8-oxooctanoate (68)

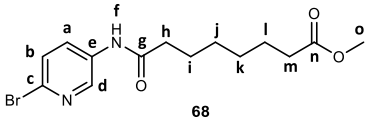

68

5-Amino-2-bromopyridine (**67**) (200 mg, 1.16 mmol), methyl 8-chloro-8-oxooctanoate (**117**) (0.16 mL, 1.16 mmol) and triethylamine (0.16 mL, 1.16 mmol) were dissolved in dry DCM (5 mL) and stirred for 16 h at room temperature under an inert atmosphere. The dark brown reaction mixture was diluted with DCM (10 mL) and washed with H_2O (3 x 15 mL). The organic layer was extracted and dried over $MgSO_4$, filtered and the solvent removed under reduced pressure to give a dark brown solid. The product was purified via column chromatography on silica (DCM : 3% MeOH) to produce the *title compound* as a light brown solid (406 mg, 51%).

δ_H (400 MHz, acetone-d_6) 8.59 (1H, d, $^4J_{HH}$ = 2.8 Hz, H^d), 8.12 (1H, dd, $^3J_{HH}$ = 8.6 Hz, $^4J_{HH}$ = 2.8 Hz, H^a), 7.53 (1H, d, $^3J_{HH}$ = 8.6 Hz, H^b), 3.61 (3H, s, H^o), 2.42 (2H, t, $^3J_{HH}$ = 7.4 Hz, H^h), 2.31 (2H, t, $^3J_{HH}$ =

7.4 Hz, H^m), 1.69 (2H, m, H^i), 1.60 (2H, m, H^l), 1.37 (4H, m, $H^{j/k}$); δ_C (100 MHz, acetone-d_6) 173.20 (C^n), 171.21 (C^g), 140.78 (C^d), 135.08 (C^c), 134.02 (C^e), 129.09 (C^a), 127.66 (C^b), 50.43 (C^o), 36.49 (C^h), 33.31 (C^m), 28.61 ($C^{j/k}$), 24.89 (C^i), 24.58 (C^l); *m/z* (ESI HRMS$^+$) 343.0671 $[M+H]^+$ ($C_{14}H_{20}N_2O_3{}^{79}Br$ requires 343.0657).

Methyl 8-[(2-bromopyridin-3-yl-N-oxide)amino]-8-oxooctanoate (69)

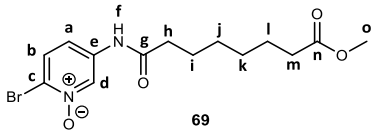

69

To a solution of methyl 8-[(2-bromopyridin-3-yl)amino]-8-oxooctanoate (**68**) (200 mg, 0.58 mmol) in DCM (15 ml) at 273 K, trifluoroacetic anhydride (0.16 mL, 1.17 mmol) was added dropwise. This was followed by the addition of urea hydrogen peroxide (110 mg, 1.17 mmol) at 273 K with stirring. The reaction mixture was allowed to warm to the room temperature and stirred at 308 K for 16 h. The reaction was quenched with a saturated aqueous solution of $Na_2S_2O_3$ (5 mL) and saturated aqueous solution of $NaHCO_3$ (20 mL) and the mixture extracted with DCM (3 x 15 mL). The organic layers were combined, dried over $MgSO_4$, filtered and the solvent evaporated under reduced pressure. The product was purified by column chromatography on silica (DCM : 0.6 % MeOH) to produce the *title compound* as a white solid (129 mg, 62%).

δ_H (400 MHz, acetone-d_6) 9.08 (1H, d, $^4J_{HH}$ = 2.2 Hz, H^d), 7.71 (1H, d, $^3J_{HH}$ = 9.0 Hz, H^b), 7.35 (1H, dd, $^3J_{HH}$ = 9.0 Hz, $^4J_{HH}$ = 2.2 Hz, H^a), 3.61 (3H, s, H^o), 2.42 (2H, t, $^3J_{HH}$ = 7.4 Hz, H^h), 2.31 (2H, t, $^3J_{HH}$ = 7.4 Hz, H^m), 1.69 (2H, m, H^i), 1.60 (2H, m, H^l), 1.37 (4H, m, $H^{j/k}$); δ_C (100 MHz, acetone-d_6) 173.17 (C^n), 171.86 (C^g), 137.92 (C^c), 131.48 (C^e), 131.39 (C^d), 129.83 (C^b), 115.82 (C^a), 50.43 (C^o), 36.47 (C^h), 33.31 (C^m), 28.58 ($C^{j/k}$), 24.83 (C^i), 24.45 (C^l); *m/z* (ESI HRMS$^+$) 358.0274 $[M+H]^+$ ($C_{14}H_{20}{}^{79}BrN_2O_4$ requires 359.0529).

8-((1-Hydroxy-6-thioxo-1,6-dihydropyridin-3-yl)amino)-8-oxooctanoic acid (73)

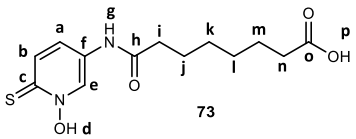

73

Methyl 8-[(2-bromopyridin-3-yl-N-oxide)amino]-8-oxooctanoate (**69**) (100 mg, 0.28 mmol) and potassium iodide (70 mg, 0.45 mmol) were added to a saturated aqueous solution of $NaSH.H_2O$ (5 mL) under stirring. The orange reaction mixture was allowed to stir for 48 h at room temperature. Upon reaction completion as indicated by TLC, the reaction mixture was cooled to 273 K, and slowly quenched with 4 M HCl (approx. 25 mL) and extracted with ethyl acetate (3 x 10 mL). The organic layers were combined, washed with saturated $NaHCO_3$ (15 mL) and brine (20 mL) sequentially, then dried over $MgSO_4$, filtered and the solvent evaporated under reduced pressure to give the *title compound* as a yellow solid which was used in subsequent steps without further purification solid (10 mg, 12%).

δ_H (400 MHz, DMSO-d_6) 10.37 (1H, br, H^d), 8.96 (1H, d, $^4J_{HH}$ = 1.9 Hz, H^e), 7.46 (1H, d, $^3J_{HH}$ = 9.1 Hz, H^b), 7.39 (1H, dd, $^3J_{HH}$ = 9.1 Hz, $^4J_{HH}$ = 1.9 Hz, H^a), 2.32 (2H, t, $^3J_{HH}$ = 7.4 Hz, H^i), 2.19 (2H, t, $^3J_{HH}$ = 7.3 Hz, H^n), 1.56 (2H, m, H^j), 1.49 (2H, m, H^m), 1.39 (4H, m, $H^{k/l}$); δ_C (100 MHz, DMSO-d_6) 175.23 (C^o), 172.43 (C^h), 135.88 (C^c), 130.01 (C^e), 129.77 (C^f), 122.24 (C^b), 118.36 (C^a), 36.57 (C^i), 34.01 (C^n), 28.64 ($C^{k/l}$), 25.05 (C^j), 24.69 (C^m); *m/z* (ESI HRMS$^+$) 299.1110 $[M+H]^+$ ($C_{13}H_{19}N_2O_4S$ requires 299.1066).

(8-((1-Hydroxy-6-thioxo-1,6-dihydropyridin-3-yl)amino)-8-oxooctanoic acid)$_2$copper(II) (75)

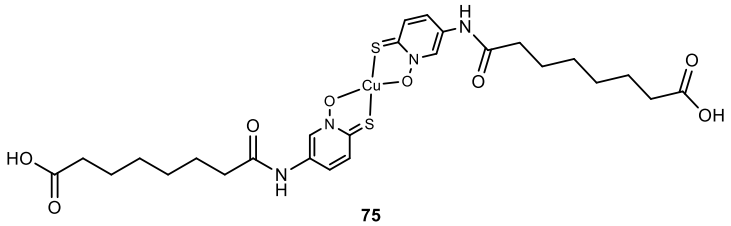

75

To a solution of 8-((1-hydroxy-6-thioxo-1,6-dihydropyridin-3-yl)amino)-8-oxooctanoic acid (**73**) (15 mg, 0.050 mmol) in DMF (5 mL), a solution of copper chloride dihydrate (4.30 mg, 0.025) in DMF (2 mL) was added dropwise. The reaction mixture was stirred for 1 h, where upon reaction completion as indicated by TLC, removal of the solvent under reduced pressure yielded the *title complex* as a dark green solid which is currently awaiting purification via HPLC (13 mg, 76%).

m/z (ESI HRMS$^+$) 658.1169 $[M+H]^+$ ($C_{26}H_{35}CuN_4O_8S_2$ requires 658.1192).

N^1-(6-Bromopyridin-3-yl)-N^8-hydroxyoctanediamide (81)

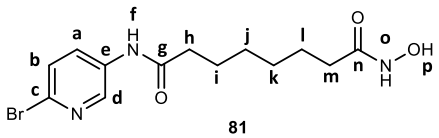

81

Methyl 8-[(2-bromopyridin-3-yl)amino]-8-oxooctanoate (**68**) (50 mg, 0.15 mmol) was dissolved in methanol : 50% hydroxylamine solution (1:1, 5 mL) and 1M NaOH solution was added (0.5 mL) to pH 11. The mixture was stirred at 338 K for 2 h and left to cool to room temperature before the solution was neutralised to pH 7 by addition of 1 M HCl (10 mL). The reaction mixture was cooled to 273 K where a precipitate formed which was collected via filtration and dried under vacuum to give the *title compound* as a beige solid (7 mg, 14%).

δ_H (400 MHz, MeOD) 8.55 (1H, d, $^4J_{HH}$ = 2.7 Hz, H^d), 7.98 (1H, dd, $^3J_{HH}$ = 8.7 Hz, $^4J_{HH}$ = 2.7 Hz, H^a), 7.52 (1H, d, $^3J_{HH}$ = 8.7 Hz, H^b), 2.37 (2H, t, $^3J_{HH}$ = 7.4 Hz, H^h), 2.08 (2H, t, $^3J_{HH}$ = 7.4 Hz, H^m), 1.68 (2H, m, H^i), 1.61 (2H, m, H^l), 1.41 (4H, m, $H^{j/k}$); δ_C (100 MHz, MeOD) 173.50 (C^g), 171.48 (C^n), 140.76 (C^d), 135.56 (C^c), 134.21 (C^e), 129.97 (C^a), 127.84 (C^b), 36.18 (C^h), 32.19 (C^m), 28.31 ($C^{j/k}$), 25.07 (C^i), 24.91 (C^l); *m/z* (ESI HRMS$^+$) 344.0604 $[M+H]^+$ ($C_{13}H_{19}{}^{79}BrN_3O_3$ requires 344.0610).

Methyl 8-oxo-8-(p-tolylamino)octanoate (85)

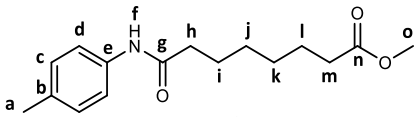

85

p-Toluidine (**84**) (100 mg, 0.93 mmol), methyl 8-chloro-8-oxooctanoate (**117**) (0.13 mL, 0.93 mmol) and triethylamine (0.13 mL, 0.93 mmol) were dissolved in dry DCM (5 mL) and stirred for 16 h at room temperature under an inert atmosphere. The colourless reaction mixture was diluted with DCM (10 mL) and washed with H_2O (3 x 15 mL). The organic layer was extracted and dried over $MgSO_4$, filtered and the solvent removed under reduced pressure to give a white solid. The product was purified via column chromatography on silica (DCM : 3 % MeOH) to produce the *title compound* as a white solid (288 mg, 56%).

δ_H (400 MHz, acetone-d_6) 7.53 (2H, d, $^3J_{HH}$ = 8.4 Hz, H^d), 7.08 (2H, d, $^3J_{HH}$ = 8.4 Hz, H^c), 3.61 (3H, s, H^o), 2.62 (3H, s, H^a), 2.33 (2H, t, $^3J_{HH}$ = 7.3 Hz, H^h), 2.29 (2H, t, $^3J_{HH}$ = 7.4 Hz, H^m), 1.67 (2H, m, H^i), 1.59 (2H, m, H^l), 1.36 (4H, m, $H^{j/k}$); δ_C (100 MHz, acetone-d_6) 173.15 (C^n), 170.65 (C^g), 137.14 (C^b), 132.03 (C^e), 128.91 (C^c), 119.04 (C^d), 50.52 (C^o), 19.82 (C^a), 36.68 (C^h), 33.31 (C^m), 28.56 ($C^{j/k}$), 25.15 (C^i), 24.53 (C^l); *m/z* (ESI HRMS$^+$) 278.1753 $[M+H]^+$ ($C_{16}H_{23}NO_3$ requires 278.1756).

Methyl 8-oxo-8-(pyridin-2-ylamino)octanoate (102)

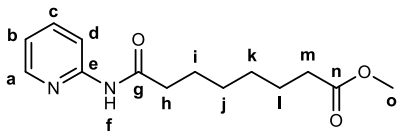

102

Methyl 8-chloro-8-oxooctanoate (**117**) (227 mg, 1.10 mmol), 2-aminopyridine (104 mg, 1.10 mmol) and 4-dimethylaminopyridine (0.018 g, 0.15 mmol) were dissolved in dry DMF (5 mL) and stirred under a nitrogen atmosphere at room temperature for 3 h. The solution was concentrated under reduced pressure, then diluted with H_2O (35 mL) where the product was extracted using DCM (3 x 25 mL). The organic layers were combined, dried over $MgSO_4$, filtered and the solvent evaporated under reduced pressure to yield a clear oil. The crude product was purified by column chromatography on silica (DCM : MeOH 2%) to yield the *title compound* as a white solid (104 mg, 36%).

δ_H (400 MHz, MeOD) 8.29 (1H, dd, $^3J_{HH}$ = 4.9 Hz, $^4J_{HH}$ = 0.9 Hz, H^a), 8.11 (1H, d, $^3J_{HH}$ = 8.4 Hz, H^d), 7.77 (1H, ddd, $^3J_{HH}$ = 8.4 Hz, 7.3 Hz, $^4J_{HH}$ = 1.9 Hz, H^c), 7.10 (1H, ddd, $^3J_{HH}$ = 7.4 Hz, 5.0 Hz, $^4J_{HH}$ = 1.1 Hz, H^b), 5.51 (1H, s, H^f), 3.66 (3H, s, H^o), 2.45 (2H, t, J = 7.5 Hz, H^h), 2.33 (2H, t, J = 7.4 Hz, H^m), 1.71 (2H, p, J = 7.4 Hz, H^i), 1.63 (2H, p, J = 7.4 Hz, H^l), 1.40 (4H, m, $H^{j/k}$); *m/z* (ESI HRMS$^+$) 265.1541 $[M+H]^+$ ($C_{14}H_{21}N_2O_3$ requires 265.1552).

N^2-hydroxy-N^{11}-(pyridin-2-yl)octanediamide (103)

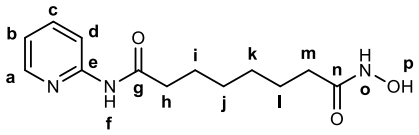

103

Methyl 8-oxo-8-(pyridine-2-yl-amino)octanoate (**102**) (56 mg, 0.21 mmol) was suspended in MeOH : 50% hydroxylamine solution (1:1, 6 mL), and NaOH was added (0.5 mL, 1M) until a pH of 11 was reached. The mixture was stirred for 2 h at 338 K, then neutralised to pH 7 by addition of 1M HCl (approx. 20.5 mL). The precipitate that formed on cooling was cold filtered and dried under vacuum, to give the *title compound* as a white solid (47 mg, 86%).

δ_H (400 MHz, MeOD) δ 8.29 (1H, dd, $^3J_{HH}$ = 5.0 Hz, $^4J_{HH}$ = 2.0 Hz, H^a), 8.08 (1H, dd, $^3J_{HH}$ = 8.4 Hz, $^4J_{HH}$ = 1.0 Hz, H^d), 7.79 (1H, ddd, $^3J_{HH}$ = 8.4 Hz, 7.4 Hz, $^4J_{HH}$ = 2.0 Hz, H^c), 7.12 (1H, ddd, $^3J_{HH}$ = 7.4 Hz, 5.0 Hz, $^4J_{HH}$ = 1.0 Hz, H^b), 2.46 (2H, t, $^3J_{HH}$ = 7.5 Hz, H^h), 2.11 (2H, t, $^3J_{HH}$ = 7.4 Hz, H^m), 1.73 (2H, p, $^3J_{HH}$ = 7.5 Hz, H^i), 1.64 (2H, p, $^3J_{HH}$ = 7.4 Hz, H^l), 1.41 (4H, m, $H^{j/k}$); δ_C (100 MHz, MeOD) 173.68 (C^g), 171.52

(C^{n}), 151.42 (C^{e}), 146.86 (C^{a}), 138.55 (C^{c}), 119.48 (C^{b}), 114.32 (C^{d}), 36.32 (C^{h}), 32.25 (C^{m}), 28.40 (C^{j}), 28.37 (C^{k}), 25.12 (C^{l}), 24.94 (C^{i}); *m/z* (ESI HRMS^{+}) 266.1519 $[M+H]^{+}$ ($C_{13}H_{20}N_3O_3$ requires 266.1505).

(η^6-p-Cymene)(N^2-hydroxy-N^{11}-(pyridine-2-yl)octanediamide)ruthenium(II) chloride (105)

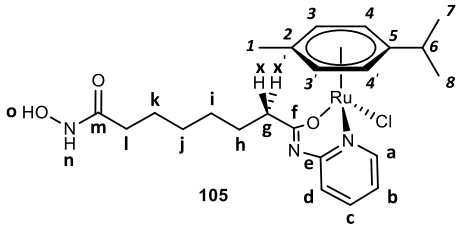

N^2-Hydroxy-N^{11}-(pyridine-2-yl)octanediamide (**103**) (38 mg, 0.14 mmol) and dichloro(η^6-*p*-cymene)ruthenium(II)-dimer (46 mg, 0.07 mmol) were dissolved in dry methanol (5 mL) and stirred under a nitrogen atmosphere for 16 h at 323 K. The solvent was removed under reduced pressure to give an orange solid and subsequently dissolved in DCM : MeOH (3:1, 1 ml) and cooled in an acetone/dry ice bath. The product was recrystalised via the dropwise addition of Et_2O (4 ml), where the suspension was filtered and the resulting solid was washed with cold Et_2O (2 ml) and dried under vacuum to give the *title compound* as an orange solid (40 mg, 92%).

δ_H (400 MHz, MeOD) 8.99 (1H, dd, $^3J_{HH}$ = 6.0 Hz, , $^4J_{HH}$ =1.6 Hz, H^a), 8.31 (1H, br, H^o), 8.09 (1H, ddd, $^3J_{HH}$ = 8.1 Hz, 6.0 Hz, $^4J_{HH}$ =1.4 Hz, H^c), 7.59 (1H, br, H^n), 7.42 (1H, ddd, $^3J_{HH}$ = 8.1 Hz, 7.4 Hz, $^4J_{HH}$ = 1.6 Hz, H^b), 7.27 (1H, dd, $^3J_{HH}$ = 7.4 Hz, $^4J_{HH}$ = 1.4 Hz, H^d), 5.93 (1H, m, $H^{3'}$), 5.89 (1H, m, H^3), 5.67 (2H, m, $H^{4/4'}$), 2.90 (1H, sept, $^3J_{HH}$ = 7.0 Hz, H^6), 2.68 (1H, m, $H^{x'}$), 2.64 (1H, m, H^x), 2.21 (3H, s, H^1), 2.13 (2H, td, $^3J_{HH}$ = 7.2 Hz, $^4J_{HH}$ = 1.5 Hz, H^l), 1.79 (2H, m, H^h), 1.66 (2H, m, H^k), 1.42 (4H, m, $H^{i/j}$), 1.30 (6H, dd, $^3J_{HH}$ = 7.0 Hz, $^4J_{HH}$ = 1.3 Hz, $H^{7/8}$); δ_C (100 MHz, MeOD) 177.67 (C^f), 171.46 (C^m), 155.54 (C^a), 147.43 (C^e), 141.39 (C^c), 122.35 (C^b), 115.39 (C^d), 103.64 (C^5), 100.20 (C^2), 84.76 ($C^{3'}$), 83.82 (C^3), 81.15 ($C^{4'}$), 80.94 (C^4), 35.94 (C^g), 32.13 (C^l), 30.92 (C^6), 28.08 (C^j), 28.06 (C^i), 24.92 (C^k), 24.65 (C^h), 21.45 (C^7), 20.64 (C^8), 17.15 (C^1); *m/z* (ESI HRMS^{+}) 494.1527 $[M-Cl]^{+}$ ($C_{23}H_{32}N_3O_3$ ^{96}Ru requires 494.1520).

(η^6-Benzene)(N^2-hydroxy-N^{11}-(pyridine-2-yl)octanediamide)ruthenium(II) chloride (106)

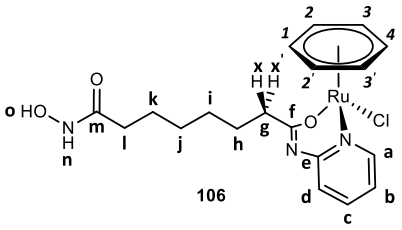

N^2-Hydroxy-N^{11}-(pyridine-2-yl)octanediamide (**103**) (40 mg, 0.15 mmol) and dichloro(η^6-benzene)ruthenium(II)-dimer (38 mg, 0.075 mmol) were dissolved in dry MeOH (5 mL) and stirred under a nitrogen atmosphere for 16 h at 323 K. The solvent was removed under reduced pressure to give an orange solid and subsequently dissolved in DCM : MeOH (3:1, 1 ml) and cooled in an acetone/dry ice bath. The product was recrystalised via the dropwise addition of Et_2O (4 ml), where the suspension was filtered and the resulting solid was washed with cold Et_2O (2 ml) and dried under vacuum to give the *title compound* as a brown solid (63 mg, 89 %).

δ_H (400 MHz, MeOD) 9.10 (1H, dd, $^3J_{HH}$ = 6.0 Hz, $^4J_{HH}$ = 1.6 Hz, H^a), 8.09 (1H, ddd, $^3J_{HH}$ = 7.9 Hz, 6.7 Hz, $^4J_{HH}$ = 1.6 Hz, H^c), 7.40 (1H, ddd, $^3J_{HH}$ = 6.7 Hz, 6.0 Hz, $^4J_{HH}$ = 1.2 Hz, H^b), 7.22 (1H, dd, $^3J_{HH}$ = 7.9 Hz, $^4J_{HH}$ = 1.2 Hz, H^d), 6.04 (6H, s, H^{1-4}), 2.69 (1H, m, $H^{x'}$), 2.61 (1H, m, H^x), 2.13 (2H, td, $^3J_{HH}$ = 7.4 Hz, $^4J_{HH}$ = 2.6 Hz, H^l), 1.80 (2H, m, H^h), 1.67 (2H, m, H^k), 1.45 (4H, m, $H^{i/j}$); δ_C (100 MHz, MeOD) 177.78 (C^f), 171.79 (C^m), 155.75 (C^a), 147.50 (C^e), 141.39 (C^c), 122.05 (C^b), 115.36 (C^d), 84.72 (C^{1-4}), 35.84 (C^g), 32.12 (C^l), 28.29 ($C^{i/j}$), 25.15 (C^k), 24.81 (C^h); *m/z* (ESI HRMS$^+$) 444.0854 $[M-Cl]^+$ ($C_{19}H_{24}N_3O_3$ ^{96}Ru requires 444.0860).

(η^6-N-benzylbenzamide)(N^2-hydroxy-N^{11}-(pyridine-2-yl)octanediamide)ruthenium(II) chloride (107)

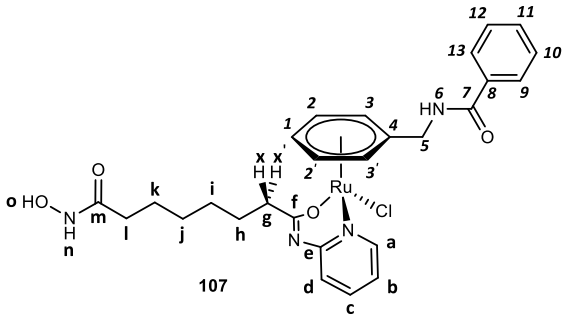

107

N^2-Hydroxy-N^{11}-(pyridine-2-yl)octanediamide (**103**) (14 mg, 0.052 mmol) and dichloro(η^6-*N*-benzylbenzamide)ruthenium(II)-dimer (20 mg, 0.026 mmol were dissolved in dry methanol (5 mL) and stirred under a nitrogen atmosphere for 16 h at 323 K. The solvent was removed under reduced pressure to give the crude product as a brown solid (23 mg).

δ_H (400 MHz, MeOD) δ_H (400 MHz, MeOD) 8.92 (1H, dd, $^3J_{HH}$ = 6.1 Hz, $^4J_{HH}$ = 1.6 Hz, H^a), 7.93 (1H, ddd, $^3J_{HH}$ = 7.5 Hz, 6.9 Hz, $^4J_{HH}$ = 1.6 Hz, H^c), 7.75 (2H, d, $^3J_{HH}$ = 8.0 Hz, $H^{9/13}$), 7.50 (1H, t, $^3J_{HH}$ = 6.3 Hz, H^{11}), 7.41 (2H, dd, $^3J_{HH}$ = 8.0 Hz, $^3J_{HH}$ = 6.3 Hz, $H^{10/12}$), 7.26 (1H, ddd, $^3J_{HH}$ = 6.9 Hz, 6.1 Hz, $^4J_{HH}$ = 1.4 Hz, H^b), 7.12 (1H, dd, $^3J_{HH}$ = 7.5 Hz, $^4J_{HH}$ = 1.4 Hz, H^d), 5.94 (2H, m, $H^{2/2'}$), 5.62 (2H, m, $H^{3/3'}$), 4.49 (2H, s, H^5), 2.60 (1H, m, $H^{x'}$), 2.54 (1H, m, H^x), 2.06 (2H, td, $^3J_{HH}$ = 7.2 Hz, $^4J_{HH}$ = 2.6 Hz, H^l), 1.69 (2H, m, H^h), 1.61 (2H, m, H^k), 1.35 (4H, m, $H^{i/j}$); δ_C (100 MHz, MeOD) 177.28 (C^f), 168.28 (C^m), 161.52 (C^7),

155.39 (C^{a}), 147.36 (C^{e}), 141.11 (C^{c}), 134.22 (C^{8}), 131.73 (C^{11}), 128.78 (C^{d}), 128.15 ($C^{10/12}$), 126.93 ($C^{9/13}$), 121.98 (C^{b}), 102.30 (C^{4}), 87.63 (C^{1}), 86.59 ($C^{2/2'}$), 80.11 ($C^{3/3'}$), 39.94 (C^{5}), 35.92 (C^{g}), 32.08 (C^{l}), 28.09 ($C^{i/j}$), 24.96 (C^{k}), 24.42 (C^{h}); *m/z* (ESI HRMS^{+}) 577.1384 $[M\text{-}Cl]^{+}$ ($C_{27}H_{31}N_4O_4$ ^{96}Ru requires 577.1388).

(η⁶-N-benzylpivalamide)(N²-hydroxy-N¹¹-(pyridine-2-yl)octanediamide)ruthenium(II) chloride (108)

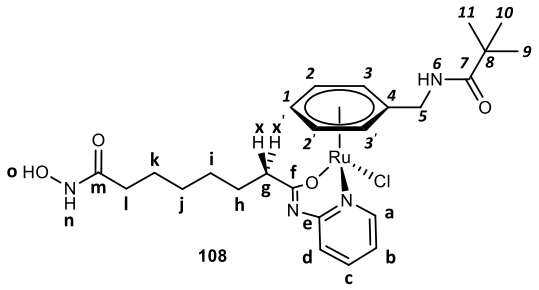

N^{2}-Hydroxy-N^{11}-(pyridine-2-yl)octanediamide (**103**) (14 mg, 0.055 mmol) and dichloro(η⁶-*N*-benzylpivalamide)ruthenium(II)-dimer (20 mg, 0.028 mmol) were dissolved in dry methanol (5 mL) and stirred under a nitrogen atmosphere for 16 h at 323 K. The solvent was removed under reduced pressure to give the crude product as a brown solid (20 mg).

δ_H (400 MHz, MeOD) 9.04 (1H, dd, $^{3}J_{HH}$ = 6.0 Hz, $^{4}J_{HH}$ = 1.5 Hz, H^{a}), 8.04 (1H, ddd, $^{3}J_{HH}$ = 7.9 Hz, 7.4 Hz, $^{4}J_{HH}$ = 1.5 Hz, H^{c}), 7.35 (1H, ddd, $^{3}J_{HH}$ = 7.4 Hz, 6.0 Hz, $^{4}J_{HH}$ = 1.3 Hz, H^{b}), 7.22 (1H, dd, $^{3}J_{HH}$ = 7.9 Hz, $^{4}J_{HH}$ = 1.3 Hz, H^{d}), 6.03 (1H, m, H^{2}), 6.01 (1H, m, $H^{2'}$), 5.94 (1H, t, $^{3}J_{HH}$ = 5.6 Hz, H^{1}), 5.86 (1H, m, $H^{3'}$), 5.77 (1H, m, H^{3}), 4.36 (2H, s, H^{5}), 2.69 (1H, m, $H^{x'}$), 2.59 (1H, m, H^{x}), 2.14 (2H, td, $^{3}J_{HH}$ = 7.4 Hz, $^{4}J_{HH}$ = 2.8 Hz, H^{l}), 1.77 (2H, m, H^{h}), 1.63 (2H, m, H^{k}), 1.39 (4H, m, $H^{i/j}$), 1.21 (9H, s, $H^{9\text{-}11}$); δ_C (100 MHz, MeOD) 180.36 (C^{7}), 177.61 (C^{f}), 171.54 (C^{m}), 155.73 (C^{a}), 147.40 (C^{e}), 141.45 (C^{c}), 122.15 (C^{b}), 115.63 (C^{d}), 101.34 (C^{4}), 87.08 ($C^{2'}$), 86.77 (C^{2}), 81.04 (C^{3}), 80.81 (C^{1}), 81.04 ($C^{3'}$), 40.35 (C^{5}), 39.54 (C^{8}), 35.96 (C^{g}), 32.05 (C^{l}), 28.11 ($C^{i/j}$), 26.40 ($C^{9\text{-}11}$), 25.02 (C^{k}), 24.86 (C^{h}); *m/z* (ESI HRMS^{+}) 557.1702 $[M\text{-}Cl]^{+}$ ($C_{25}H_{35}N_4O_4$ ^{96}Ru requires 557.1740).

(η⁶-N-benzylthiophene-2-carboxamide)(N²-hydroxy-N¹¹-(pyridine-2-yl)octanediamide)ruthenium(II) chloride (109)

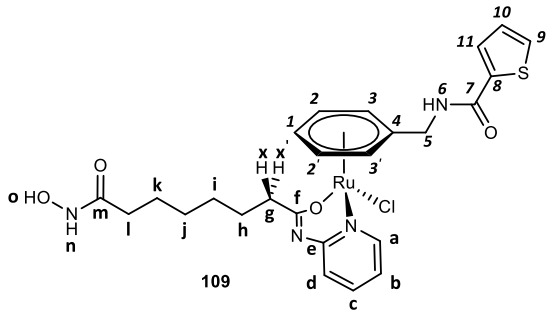

N^2-Hydroxy-N^{11}-(pyridine-2-yl)octanediamide (**103**) (14 mg, 0.053 mmol) and dichloro(η^6-*N*-benzylthiophene-2-carboxamide)ruthenium(II)-dimer (20 mg, 0.026 mmol) were dissolved in dry methanol (5 mL) and stirred under a nitrogen atmosphere for 16 h at 323 K. The solvent was removed under reduced pressure to give the crude product as a brown solid (18 mg).

δ_H (400 MHz, MeOD) 9.04 (1H, dd, $^3J_{HH}$ = 5.9 Hz, $^4J_{HH}$ = 1.4 Hz, H^a), 7.99 (1H, ddd, $^3J_{HH}$ = 8.4 Hz, 7.3 Hz, $^4J_{HH}$ = 1.4 Hz, H^c), 7.53 (1H, m, H^9) 7.31 (1H, ddd, $^3J_{HH}$ = 7.3 Hz, 5.9 Hz, $^4J_{HH}$ = 1.7 Hz, H^b), 7.29 (1H, dd, $^3J_{HH}$ = 8.4 Hz, $^4J_{HH}$ = 1.7 Hz, H^d), 7.22 (1H, m, H^{11}), 7.18 (1H, m, H^{10}), 6.01 (2H, m, $H^{2/2'}$), 5.97 (1H, m, H^1), 5.95 (2H, m, $H^{3/3'}$), 4.52 (2H, s, H^5), 2.65 (1H, m, $H^{x'}$), 2.56 (1H, m, H^x), 2.20 (2H, m, H^l), 1.74 (2H, m, H^h), 1.61 (2H, m, H^k), 1.38 (4H, m, $H^{i/j}$); δ_C (100 MHz, MeOD) 177.40 (C^f), 168.74 (C^m), 168.67 (C^7), 155.59 (C^a), 147.28 (C^e), 141.28 (C^c), 131.25 (C^9), 129.72 (C^8), 128.11 (C^{11}), 127.36 (C^{10}), 126.76 (C^d), 122.14 (C^b), 42.95 (C^5), 35.91 (C^g), 34.77 (C^l), 28.06 ($C^{i/j}$), 25.00 (C^k), 24.65 (C^h); *m/z* (ESI HRMS$^+$) 583.0991 $[M\text{-}Cl]^+$ ($C_{25}H_{29}N_4O_4\ ^{96}RuS$ requires 583.1038).

(η^6-N-benzylacetamide)(N^2- hydroxy-N^{11}-(pyridine-2-yl)octanediamide)ruthenium(II) chloride (110)

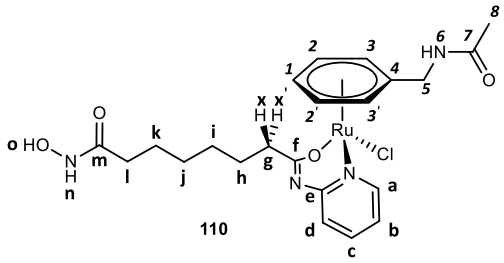

110

N^2-Hydroxy-N^{11}-(pyridine-2-yl)octanediamide (**103**) (17 mg, 0.065 mmol) and dichloro(η^6-*N*-benzylacetamide)ruthenium(II)-dimer (20 mg, 0.031 mmol) were dissolved in dry methanol (5 mL) and stirred under a nitrogen atmosphere for 16 h at 323 K. The solvent was removed under reduced pressure to give the crude product as a brown solid (29 mg).

δ_H (400 MHz, MeOD) 9.04 (1H, dd, $^3J_{HH}$ = 5.7 Hz, $^4J_{HH}$ = 1.5 Hz, H^a), 8.04 (1H, ddd, $^3J_{HH}$ = 8.3 Hz, 7.7 Hz, $^4J_{HH}$ = 1.5 Hz, H^c), 7.35 (1H, ddd, $^3J_{HH}$ = 7.7 Hz, 5.7 Hz, $^4J_{HH}$ = 1.7 Hz, H^b), 7.21 (1H, dd, $^3J_{HH}$ = 8.3 Hz, $^4J_{HH}$ = 1.7 Hz, H^d), 6.04 (1H, m, H^2), 6.00 (1H, m, $H^{2'}$), 5.92 (1H, m, $H^{3'}$), 5.89 (1H, m, H^3), 5.81 (1H, t, $^3J_{HH}$ = 4.9 Hz, H^1), 4.33 (2H, s, H^5), 2.69 (1H, m, $H^{x'}$), 2.59 (1H, m, H^x), 2.25 (2H, m, H^l), 1.77 (2H, m, H^h), 1.63 (2H, m, H^k), 1.40 (4H, m, $H^{i/j}$), 1.24 (3H, s, H^8); δ_C (100 MHz, MeOD) 177.61 (C^f), 172.40 (C^m), 164.97 (C^7), 155.67 (C^a), 147.42 (C^e), 141.40 (C^c), 126.77 (C^d), 122.19 (C^b), 100.98 (C^4), 86.99 ($C^{2/2'}$), 81.01 (C^3), 80.77 ($C^{3'}$), 79.99 (C^1), 40.02 (C^5), 35.97 (C^g), 34.87 (C^l), 28.49 (C^8), 28.07 ($C^{i/j}$), 25.00 (C^k), 24.59 (C^h); *m/z* (ESI HRMS$^+$) 515.1227 $[M\text{-}Cl]^+$ ($C_{22}H_{29}N_4O_4\ ^{96}Ru$ requires 515.1231).

(η⁶-Hexamethylbenzene)(N²-hydroxy-N¹¹-(pyridine-2-yl)octanediamide)ruthenium(II) chloride (111)

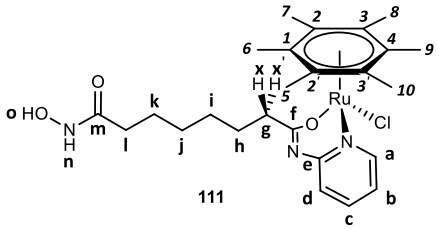

111

N^2-Hydroxy-N^{11}-(pyridine-2-yl)octanediamide (**103**) (16 mg, 0.062 mmol) and dichloro(η⁶-hexamethylbenzene)ruthenium(II)-dimer (20 mg, 0.030 mmol) were dissolved in dry methanol (5 mL) and stirred under a nitrogen atmosphere for 16 h at 323 K. The solvent was removed under reduced pressure to give the crude product as a brown solid (33 mg).

δ_H (400 MHz, MeOD) 8.40 (1H, dd, $^3J_{HH}$ = 5.9 Hz, $^4J_{HH}$ = 1.6 Hz, H^a), 8.04 (1H, ddd, $^3J_{HH}$ = 7.9 Hz, 6.7 Hz, $^4J_{HH}$ = 1.6 Hz, H^c), 7.42 (1H, ddd, $^3J_{HH}$ = 6.7 Hz, 5.9 Hz, $^4J_{HH}$ = 1.2 Hz, H^b), 7.27 (1H, dd, $^3J_{HH}$ = 7.9 Hz, $^4J_{HH}$ = 1.2 Hz, H^d), 2.73 (1H, m, $H^{x'}$), 2.69 (1H, m, H^x), 2.06 (2H, m, H^l), 2.04 (18H, s, $H^{5\text{-}10}$), 1.75 (2H, m, H^h), 1.61 (2H, m, H^k), 1.37 (4H, m, $H^{i/j}$); δ_C (100 MHz, MeOD) 178.26 (C^f), 171.42 (C^m), 153.87 (C^a), 147.59 (C^e), 141.11 (C^c), 122.33 (C^b), 114.73 (C^d), 92.41 ($C^{1\text{-}4}$), 36.64 (C^g), 32.04 (C^l), 27.96 ($C^{i/j}$), 24.80 (C^k), 24.39 (C^h); *m/z* (ESI HRMS⁺) 556.2120 $[M\text{-}Cl]^+$ ($C_{27}H_{40}N_3O_3\,{}^{96}Ru$ requires 556.2114).

(η⁶-Mesitylene)(N²-hydroxy-N¹¹-(pyridine-2-yl)octanediamide)ruthenium(II) chloride (112)

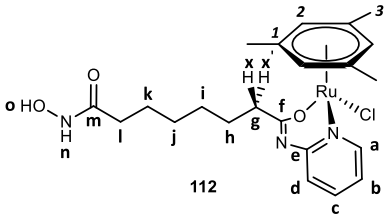

112

N^2-Hydroxy-N^{11}-(pyridine-2-yl)octanediamide (**103**) (18 mg, 0.071 mmol) and dichloro(η⁶-mesitylene)ruthenium(II)-dimer (20 mg, 0.035 mmol) were dissolved in dry methanol (5 mL) and stirred under a nitrogen atmosphere for 16 h at 323 K. The solvent was removed under reduced pressure to give the crude product as a brown solid (33 mg).

δ_H (400 MHz, MeOD) 8.86 (1H, dd, $^3J_{HH}$ = 5.6 Hz, $^4J_{HH}$ = 1.1 Hz, H^a), 8.04 (1H, ddd, $^3J_{HH}$ = 7.0 Hz, 6.8 Hz, $^4J_{HH}$ = 1.1 Hz, H^c), 7.40 (1H, ddd, $^3J_{HH}$ = 6.8 Hz, 5.6 Hz, $^4J_{HH}$ = 1.0 Hz, H^b), 7.28 (1H, dd, $^3J_{HH}$ = 7.0 Hz, $^4J_{HH}$ = 1.0 Hz, H^d), 5.41 (3H, s, H^2), 2.71 (1H, m, $H^{x'}$), 2.70 (1H, m, H^x), 2.09 (2H, m, H^l), 2.07 (9H, s, H^3), 1.75 (2H, m, H^h), 1.61 (2H, m, H^k), 1.36 (4H, m, $H^{i/j}$); δ_C (100 MHz, MeOD) 177.77 (C^f), 171.44

(C^{m}), 155.63 (C^{a}), 147.57 (C^{e}), 141.15 (C^{c}), 122.44 (C^{b}), 114.80 (C^{d}), 104.70 (C^{1}), 76.00 (C^{2}), 36.24 (C^{g}), 32.05 (C^{l}), 27.94 ($C^{i/j}$), 24.87 (C^{k}), 24.49 (C^{h}), 17.09 (C^{3}); *m/z* (ESI HRMS^{+}) 514.1654 $[M\text{-}Cl]^{+}$ ($C_{24}H_{34}N_3O_3\,^{96}Ru$ requires 514.1645).

(η⁶-N-(4-Methylbenzyl)benzamide)(N²-hydroxy-N¹¹-(pyridine-2-yl)octanediamide)ruthenium(II) chloride (113)

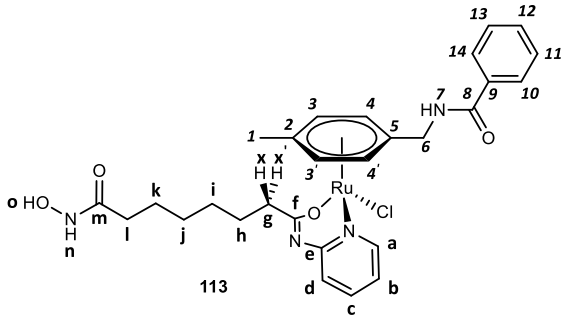

N^{2}-Hydroxy-N^{11}-(pyridine-2-yl)octanediamide (**103**) (15 mg, 0.053 mmol) and dichloro(η⁶-*N*-(4-methylbenzyl)benzamide)ruthenium(II)-dimer (20 mg, 0.027 mmol) were dissolved in dry methanol (5 mL) and stirred under a nitrogen atmosphere for 16 h at 323 K. The solvent was removed under reduced pressure to give the crude product as a brown solid (40 mg).

δ_H (400 MHz, MeOD) 8.98 (1H, d, $^{3}J_{HH}$ = 5.6 Hz, H^{a}), 7.93 (1H, dd, $^{3}J_{HH}$ = 7.5 Hz, 6.5 Hz, H^{c}), 7.81 (2H, d, $^{3}J_{HH}$ = 7.6 Hz, $H^{10/14}$), 7.53 (1H, t, $^{3}J_{HH}$ = 6.7 Hz, H^{12}), 7.44 (2H, dd, $^{3}J_{HH}$ = 7.6 Hz, $^{3}J_{HH}$ = 6.7 Hz, $H^{11/13}$), 7.28 (1H, dd, $^{3}J_{HH}$ = 6.5 Hz, 5.6 Hz, H^{b}), 7.12 (1H, dd, $^{3}J_{HH}$ = 7.5 Hz, H^{d}), 6.03 (2H, m, $H^{3/3'}$), 5.66 (2H, m, $H^{4/4'}$), 4.53 (2H, s, H^{6}), 2.60 (1H, m, $H^{x'}$), 2.53 (1H, m, H^{x}), 2.21 (3H, s, H^{1}), 2.08 (2H, td, $^{3}J_{HH}$ = 7.2 Hz, $^{4}J_{HH}$ = 2.6 Hz, H^{l}), 1.69 (2H, m, H^{h}), 1.60 (2H, m, H^{k}), 1.35 (4H, m, $H^{i/j}$); δ_C (100 MHz, MeOD) 177.21 (C^{f}), 168.30 (C^{m}), 162.47 (C^{8}), 155.44 (C^{a}), 147.31 (C^{e}), 141.16 (C^{c}), 134.26 (C^{9}), 131.79 (C^{12}), 128.70 (C^{d}), 128.14 ($C^{11/13}$), 126.93 ($C^{10/14}$), 122.08 (C^{b}), 102.33 (C^{5}), 93.62 (C^{2}), 86.57 ($C^{3/3'}$), 80.13 ($C^{4/4'}$), 39.85 (C^{6}), 35.92 (C^{g}), 32.09 (C^{l}), 28.07 ($C^{i/j}$), 24.95 (C^{k}), 24.47 (C^{h}), 17.38 (C^{1}); *m/z* (ESI HRMS^{+}) 592.1626 $[M\text{-}Cl]^{+}$ ($C_{28}H_{34}N_4O_4\,^{96}Ru$ requires 592.1624).

(η⁶-N-(4-Methylbenzyl)pivalamide)(N²-hydroxy-N¹¹-(pyridine-2-yl)octanediamide)ruthenium(II) chloride (114)

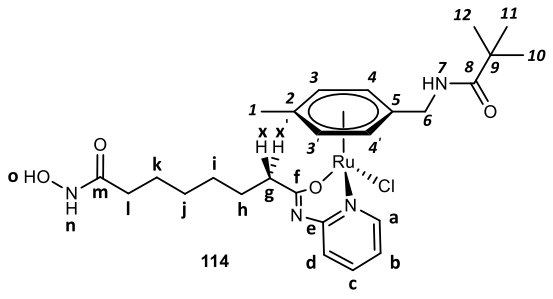

N^2-Hydroxy-N^{11}-(pyridine-2-yl)octanediamide (**103**) (20 mg, 0.066 mmol) and dichloro(η^6-*N*-(4-methylbenzyl)pivalamide)ruthenium(II)-dimer (20 mg, 0.033 mmol) were dissolved in dry methanol (5 mL) and stirred under a nitrogen atmosphere for 16 h at 323 K. The solvent was removed under reduced pressure to give the crude product as a brown solid (20 mg).

δ_H (400 MHz, MeOD) 8.97 (1H, dd, $^3J_{HH}$ = 6.0 Hz, $^4J_{HH}$ = 1.3 Hz, H^a), 8.04 (1H, ddd, $^3J_{HH}$ = 8.1 Hz, 7.8 Hz, $^4J_{HH}$ = 1.3 Hz, H^c), 7.37 (1H, ddd, $^3J_{HH}$ = 7.8 Hz, 6.0 Hz, $^4J_{HH}$ = 1.1 Hz, H^b), 7.23 (1H, dd, $^3J_{HH}$ = 8.1 Hz, $^4J_{HH}$ = 1.1 Hz, H^d), 5.87 (2H, m, $H^{3/3'}$), 5.72 (2H, m, $H^{4/4'}$), 4.33 (2H, s, H^6), 2.70 (1H, m, $H^{x'}$), 2.61 (1H, m, H^x), 2.17 (3H, s, H^1), 2.10 (2H, m, H^l), 1.77 (2H, m, H^h), 1.63 (2H, m, H^k), 1.39 (4H, m, $H^{i/j}$), 1.16 (9H, s, H^{10-12}); δ_C (100 MHz, MeOD) 180.20 (C^8), 177.52 (C^f), 171.48 (C^m), 155.52 (C^a), 147.39 (C^e), 141.35 (C^c), 122.17 (C^b), 115.66 (C^d), 100.11 (C^5), 94.65 (C^2), 85.03 ($C^{3/3'}$), 81.70 ($C^{4/4'}$), 39.78 (C^9), 39.74 (C^6), 35.95 (C^g), 32.04 (C^l), 28.05 ($C^{i/j}$), 26.28 (C^{10-12}), 24.98 (C^k), 24.75 (C^h), 17.08 (C^1); *m/z* (ESI HRMS$^+$) 572.1940 $[M\text{-}Cl]^+$ ($C_{26}H_{38}N_4O_4$ ^{96}Ru requires 572.1938).

(η^6-N-(4-Methylbenzyl)acetamide)(N^2-hydroxy-N^{11}-(pyridine-2-yl)octanediamide)ruthenium(II) chloride (115)

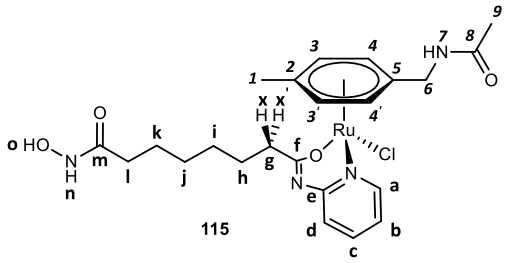

N^2-Hydroxy-N^{11}-(pyridine-2-yl)octanediamide (**103**) (18 mg, 0.060 mmol) and dichloro(η^6-*N*-(4-methylbenzyl)acetamide)ruthenium(II)-dimer (20 mg, 0.030 mmol) were dissolved in dry methanol (5 mL) and stirred under a nitrogen atmosphere for 16 h at 323 K. The solvent was removed under reduced pressure to give the crude product as a brown solid (24 mg).

δ_H (400 MHz, MeOD) 9.07 (1H, dd, $^3J_{HH}$ = 6.0 Hz, $^4J_{HH}$ = 1.2, H^a), 8.00 (1H, ddd, $^3J_{HH}$ = 8.1 Hz, 7.7 Hz, $^4J_{HH}$ = 1.2 Hz, H^c), 7.31 (1H, ddd, $^3J_{HH}$ = 7.7 Hz, 6.0 Hz, $^4J_{HH}$ = 1.9 Hz, H^b), 7.26 (1H, dd, $^3J_{HH}$ = 8.1 Hz, $^4J_{HH}$ = 1.9 Hz, H^d), 6.10 (1H, m, H^3), 6.05 (1H, m, $H^{3'}$), 5.92 (1H, m, $H^{4'}$), 5.86 (1H, m, H^4), 4.33 (2H, s, H^6), 2.70 (1H, m, $H^{x'}$), 2.59 (1H, m, H^x), 2.26 (2H, m, H^l), 2.15 (3H, s, H^1), 1.79 (2H, m, H^h), 1.61 (2H, m, H^k), 1.39 (4H, m, $H^{i/j}$), 1.21 (3H, s, H^9); δ_C (100 MHz, MeOD) 177.58 (C^f), 172.42 (C^m), 165.73 (C^8), 155.67 (C^a), 141.35 (C^e), 141.30 (C^c), 126.68 (C^d), 122.11 (C^b),), 102.31 (C^1), 100.98 (C^5), 86.99 ($C^{3/3'}$), 81.01 (C^4), 80.77 ($C^{4'}$), 41.74 (C^6), 35.97 (C^g), 34.89 (C^l), 28.49 (C^9), 28.07 ($C^{i/j}$), 25.01 (C^k), 24.59 (C^h); *m/z* (ESI HRMS$^+$) 529.5943 $[M\text{-}Cl]^+$ ($C_{23}H_{32}N_4O_4$ ^{96}Ru requires 529.6028).

(η⁵-Cyclopentadienyl)(N²-hydroxy-N¹¹-(pyridine-2-yl)octanediamide)rhodium(III) chloride hydrate (116)

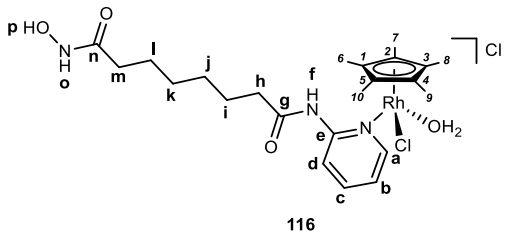

116

N^2-Hydroxy-N^{11}-(pyridine-2-yl)octanediamide (**103**) (48 mg, 0.16 mmol) and (pentamethylcyclopentadienyl)rhodium(III) dichloride dimer (47 mg, 0.08 mmol) were dissolved in dry methanol (5 mL) and stirred under a nitrogen atmosphere for 16 h at 323 K. The solvent was removed under reduced pressure to give a yellow solid. The solid was subsequently dissolved in DCM : MeOH (3:1, 1 ml) and cooled in an acetone/dry ice bath. The product was recrystalised via the dropwise addition of Et_2O (4 ml), where the suspension was filtered and the resulting solid was washed with cold Et_2O (2 ml) and dried under vacuum to give the *title complex* as a yellow solid (95 mg, 94%).

δ_H (400 MHz, MeOD) 8.53 (1H, dd, $^3J_{HH}$ = 5.8 Hz, $^4J_{HH}$ = 1.4 Hz, H^a), 8.11 (1H, ddd, $^3J_{HH}$ = 8.2 Hz, 7.7 Hz, $^4J_{HH}$ = 1.4 Hz, H^c), 7.50 (1H, ddd, $^3J_{HH}$ = 7.7 Hz, 5.8 Hz, $^4J_{HH}$ = 1.2 Hz, H^b), 7.31 (1H, dd, $^3J_{HH}$ = 8.2 Hz, $^4J_{HH}$ = 1.2 Hz, H^d), 2.70 (2H, t, $^3J_{HH}$ = 8.4 Hz, H^h), 2.12 (2H, t, $^3J_{HH}$ = 8.1 Hz, H^m), 1.66 (4H, m, $H^{i/l}$), 1.63 (15H, s, $H^{6\text{-}10}$), 1.42 (4H, m, $H^{j/k}$); δ_C (100 MHz, MeOD) 177.53 (C^g), 171.53 (C^n), 152.31 (C^a), 148.14 (C^e), 141.56 (C^c), 122.99 (C^b), 115.60 (C^d), 95.79 ($C^{1\text{-}5}$), 36.81 (C^h), 32.09 (C^m), 28.46 ($C^{j/k}$), 28.20 ($C^{i/l}$), 25.00 ($C^{6\text{-}10}$); *m/z* (ESI HRMS⁺) 571.1712 $[M]^+$ ($C_{24}H_{39}ClN_3O_4Rh$ requires 571.1685).

Other Compounds:

Copper(pyridine-2-thiolate-N-oxide)₂ (61)

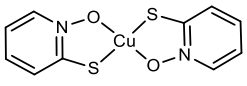

61

2-Mercaptopyridine N-oxide sodium salt (200 mg, 1.34 mmol) was dissolved in H_2O (4 ml). While stirring, a solution of copper sulfate dihydrate (114 mg, 0.67 mmol) in H_2O (4 ml) was added dropwise and the reaction mixture was stirred for 2 h. The green precipitate that formed was collected through filtration and washed with water and ethanol. The product was dried in vacuo to obtain the *title compound* as a light green solid (176 mg, 83%).

m/z (ESI HRMS⁺) 315.9393 $[M]^+$ ($C_{10}H_9N_2O_2S_2{}^{63}Cu$ requires 315.9401).

Methyl 8-oxo-8(phenylamino)octanoate (119)

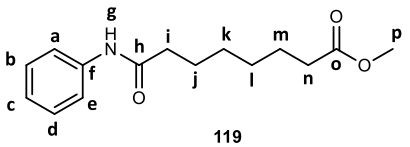

119

Methyl-8-chloro-8-oxooctanoate (**117**) (200 mg, 0.968 mmol), aniline (108 mg, 1.16 mmol) and triethylamine (0.117 g, 1.16 mmol) were dissolved in dry DCM (5 mL) and stirred at room temperature under an atmosphere of nitrogen for 2h. The solvent was removed under reduced pressure and the resultant oil was purified by column chromatography on silica (DCM : MeOH 0.5%), affording the *title compound* as a white solid (148 mg, 58%).

δ_H (400 MHz, MeOD) 7.56 (2H, m, $H^{a/e}$), 7.31 (2H, m, $H^{b/d}$), 7.09 (1H, tt, $^3J_{HH}$ = 7.3 Hz, $^4J_{HH}$ = 1.2 Hz, H^c), 3.66 (3H, s, H^p), 2.38 (2H, t, $^3J_{HH}$ = 7.0 Hz, H^i), 2.34 (2H, t, $^3J_{HH}$ = 7.6 Hz, H^n), 1.72 (2H, m, H^j), 1.65 (2H, m, H^m), 1.41 (4H, m, $H^{k/l}$); δ_C (100 MHz, MeOD) 174.51 (C^o), 173.17 (C^h), 138.46 (C^f), 128.46 ($C^{b/d}$), 123.86 (C^c), 119.95 ($C^{a/e}$), 50.66 (C^p), 36.43 (C^i), 33.25 (C^n), 28.55 ($C^{k/l}$), 25.36 (C^j), 24.48 (C^m) ; *m/z* (ESI HRMS$^+$) 264.1597 $[M+H]^+$ ($C_{15}H_{22}NO_3$ requires 264.1600).

N^2-hydroxy-N^{11}-phenyloctanediamide / suberoylanilide hydroxamic acid (SAHA) (47)

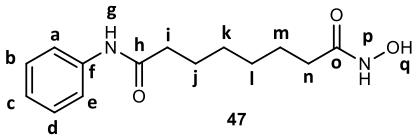

47

Methyl 8-oxo-8-(phenylamino)octanoate (**117**) (148 mg, 0.562 mmol) was suspended in MeOH: 50% hydroxylamine solution (1:1, 5 mL), and NaOH was added (0.5 mL, 1M) until a pH of 11 was reached. The mixture was stirred for 0.5 h and then neutralised to pH 7 by addition of 1M HCl (approx. 4.5 mL). A precipitate formed on standing, where the filtrate was decanted and the resulting solid dried under vacuum to give the *title compound* as a white solid (87 mg, 60%).

δ_H (400 MHz, MeOD) 7.66 (2H, m, $H^{a/e}$), 7.27 (2H, m, $H^{b/d}$), 7.01 (1H, tt, $^3J_{HH}$ = 7.40 Hz, $^4J_{HH}$ = 1.05 Hz, H^c), 2.41 (2H, t, $^3J_{HH}$ = 7.36 Hz, H^i), 2.36 (2H, t, $^3J_{HH}$ = 7.30 Hz, H^n), 1.68 (2H, m, H^j), 1.65 (2H, m, H^m), 1.41 (4H, m, $H^{k/l}$); δ_C (100 MHz, MeOD) δ_C (100 MHz, MeOD) 170.50 (C^o), 170.17 (C^h), 139.49 (C^f), 128.46 ($C^{b/d}$), 122.85 (C^c), 118.95 ($C^{a/e}$), 36.38 (C^i), 32.14 (C^n), 28.55 ($C^{k/l}$), 25.38 (C^j), 24.49 (C^m); *m/z* (ESI HRMS$^+$) 265.1560 $[M + H]^+$ ($C_{14}H_{21}N_2O_3$ requires 265.1552).

4.5 NMR spectra

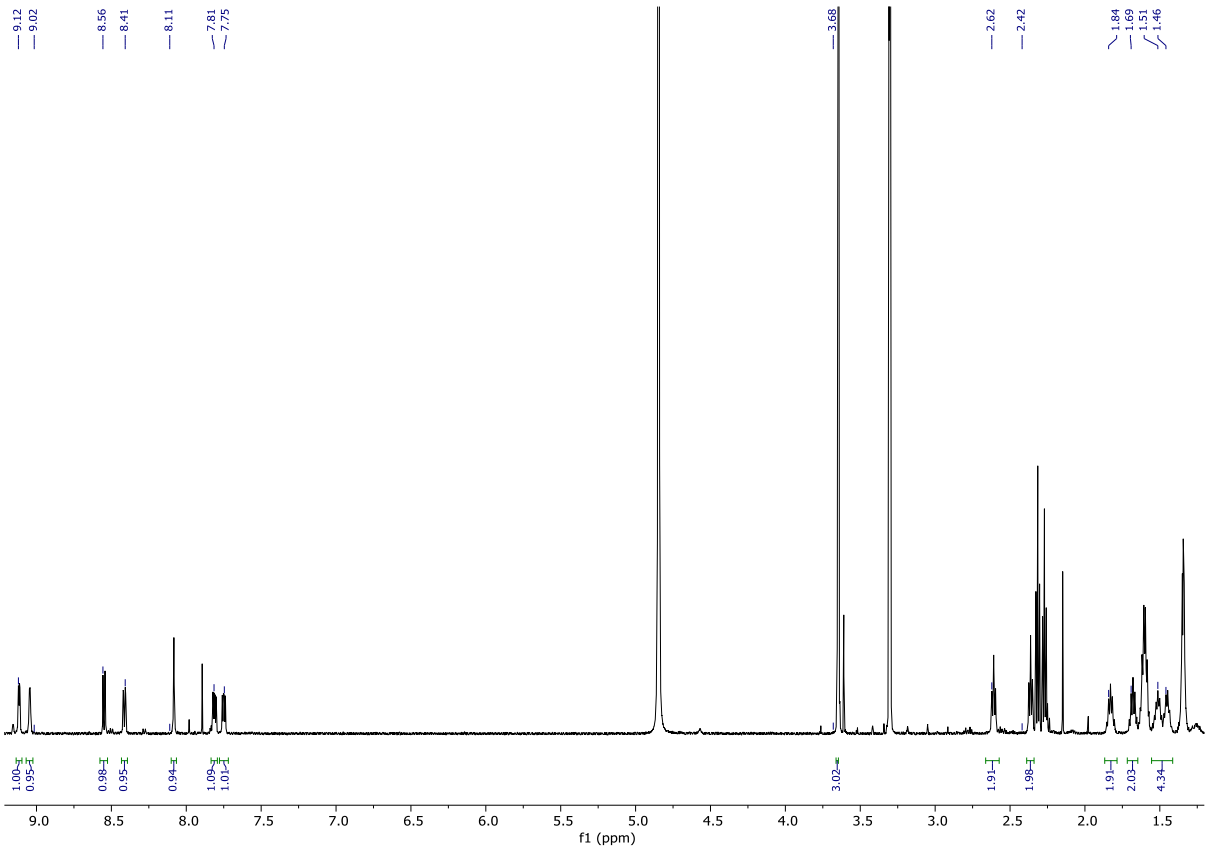

*Figure 56: ^{1}H NMR spectrum of **53** in MeOD.*

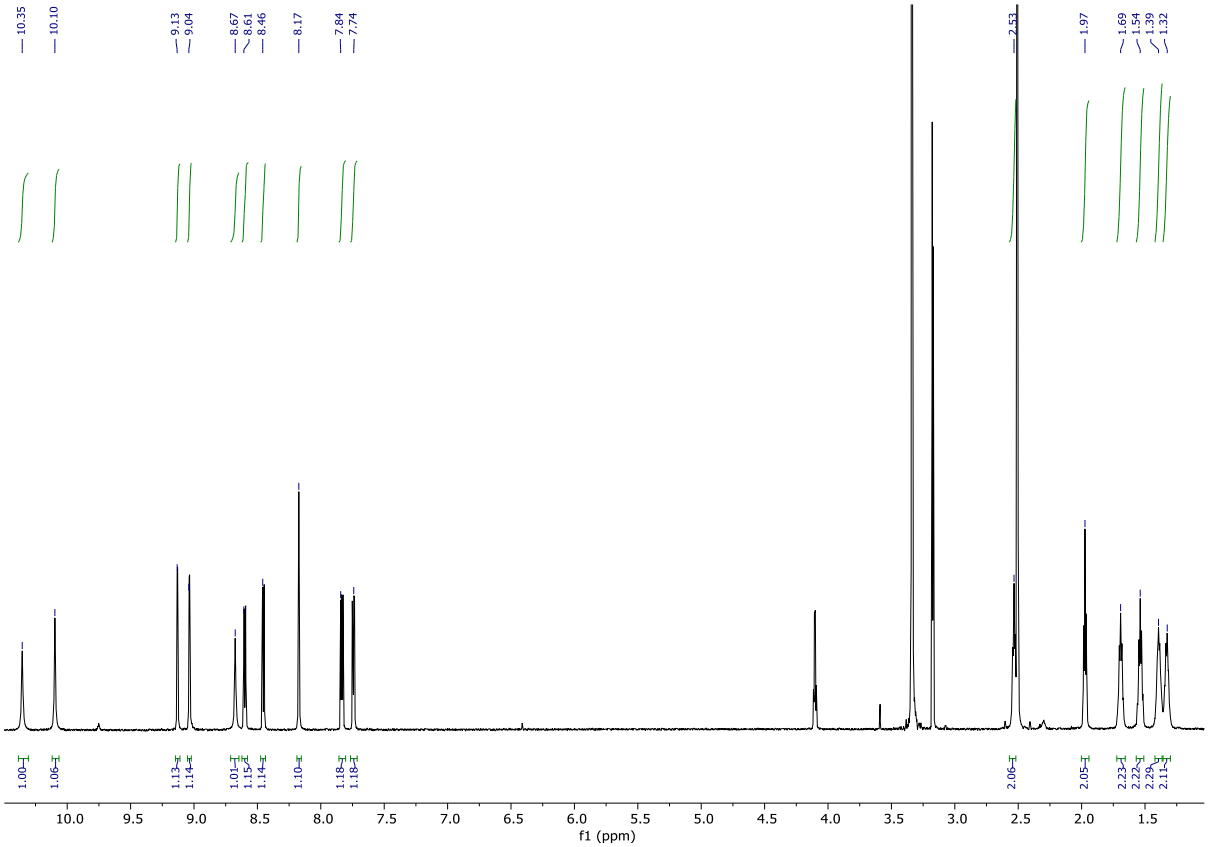

*Figure 57: ^{1}H NMR spectrum of **48** in DMSO-d_6.*

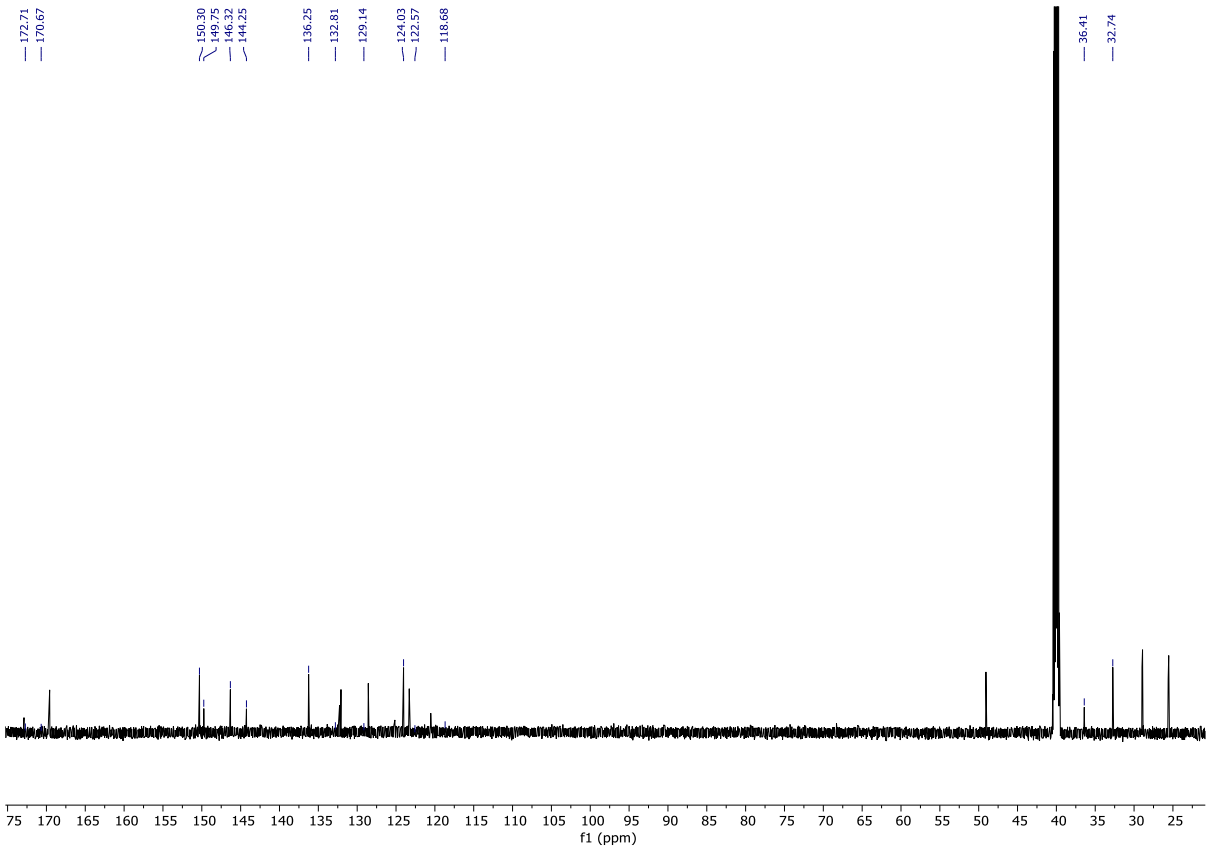

*Figure 58: ^{13}C NMR spectrum of **48** in DMSO-d_6.*

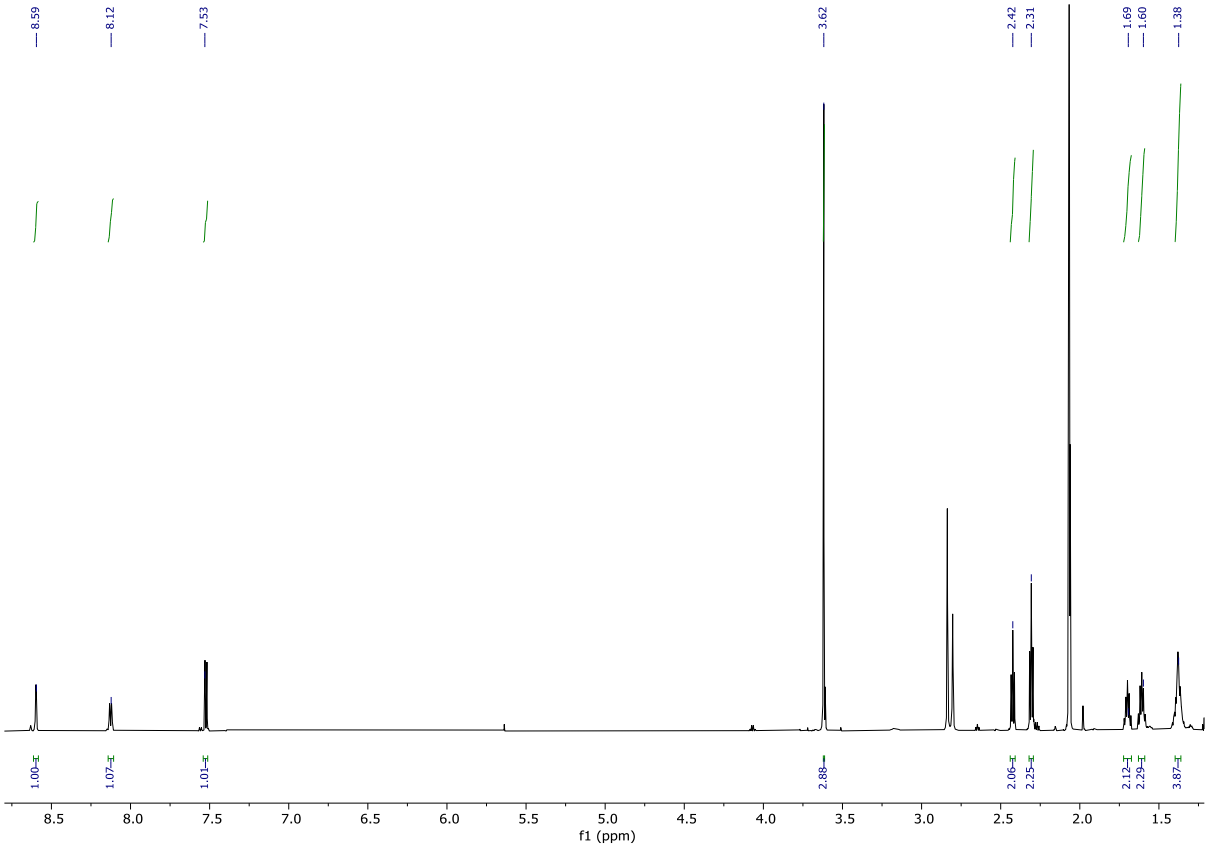

*Figure 59: ^{1}H NMR spectrum of **68** in acetone-d_6.*

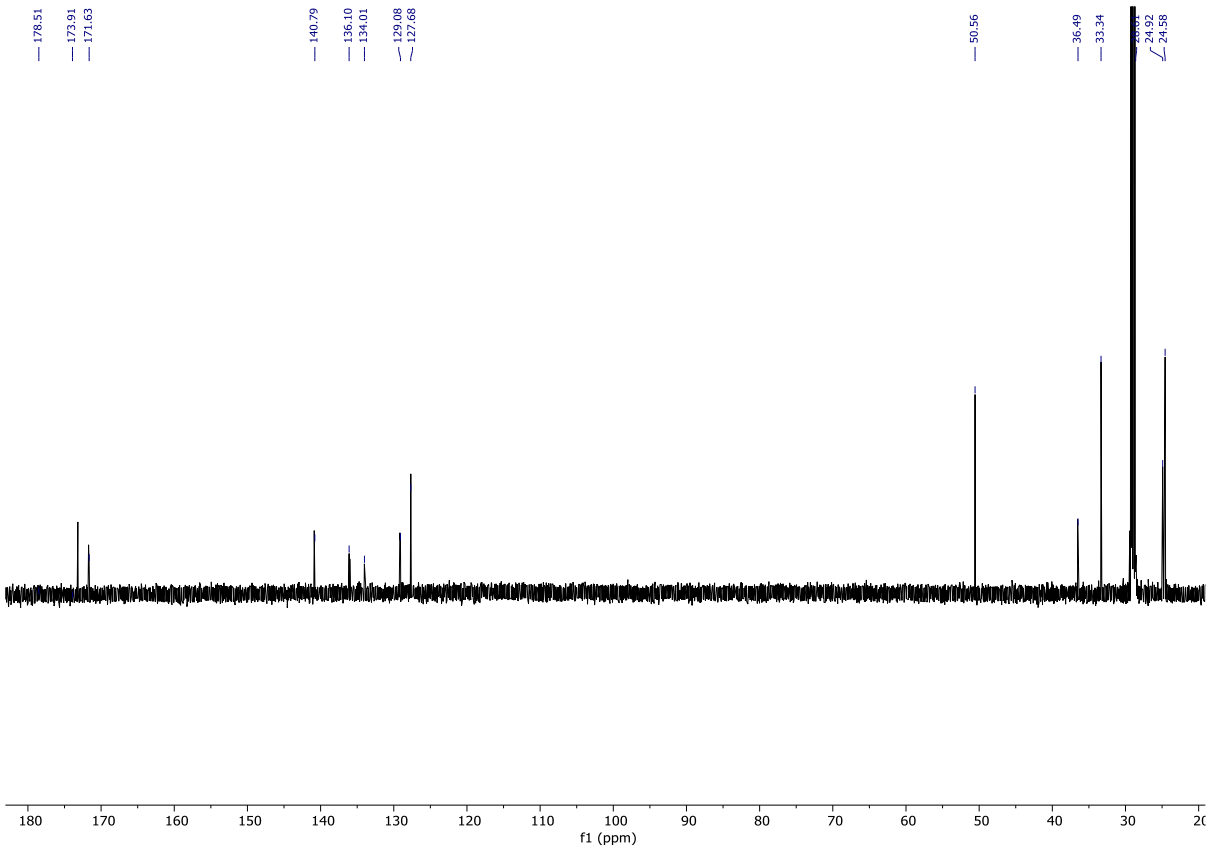

*Figure 60: ^{13}C NMR spectrum of **68** in acetone-d_6.*

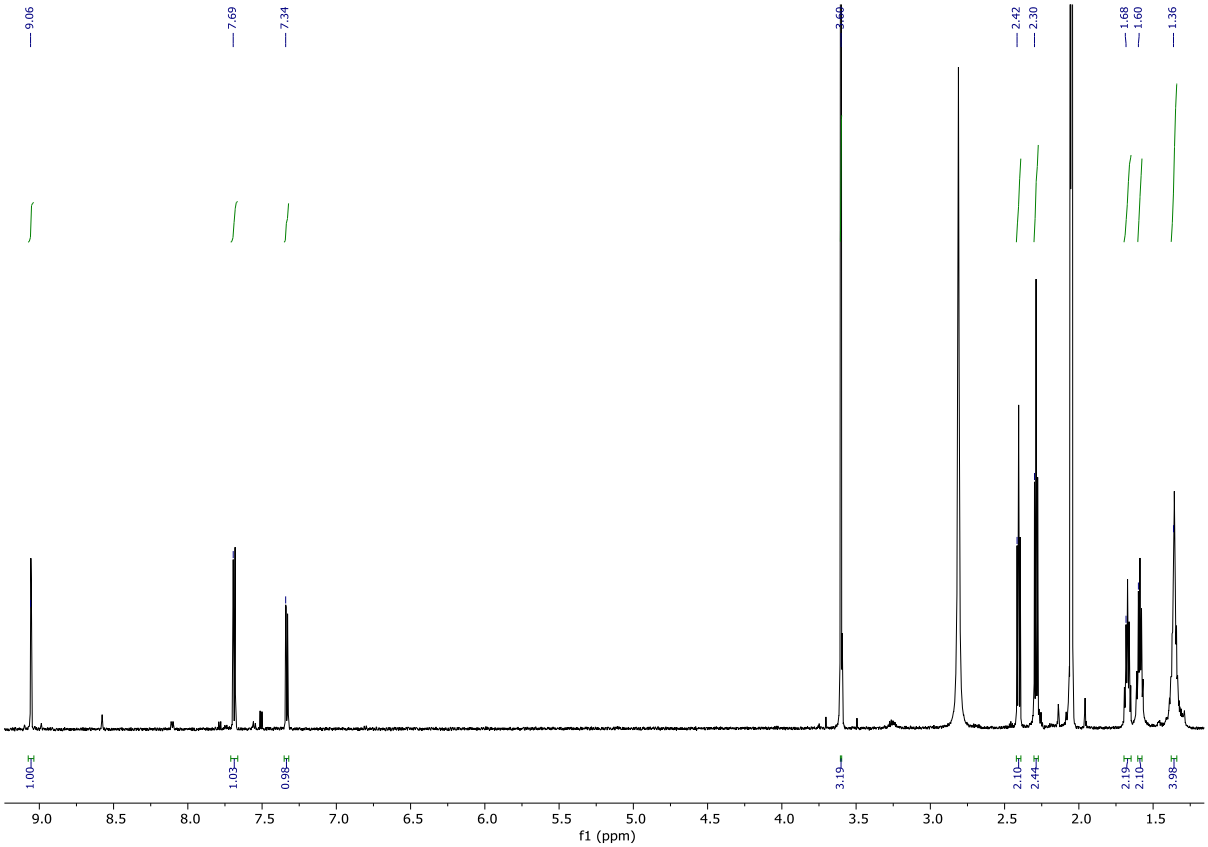

*Figure 61: ^{1}H NMR spectrum of **69** in acetone-d_6.*

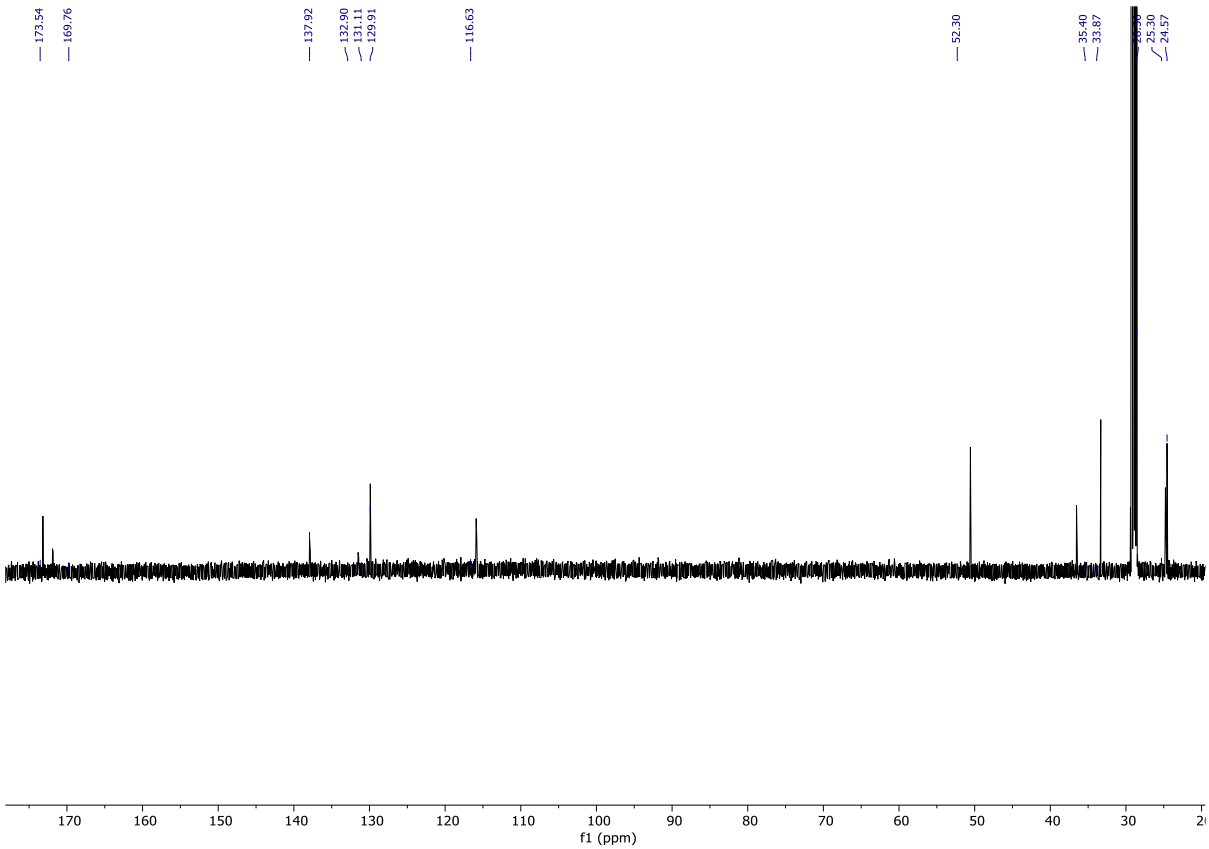

*Figure 62: ^{13}C NMR spectrum of **69** in acetone-d_6.*

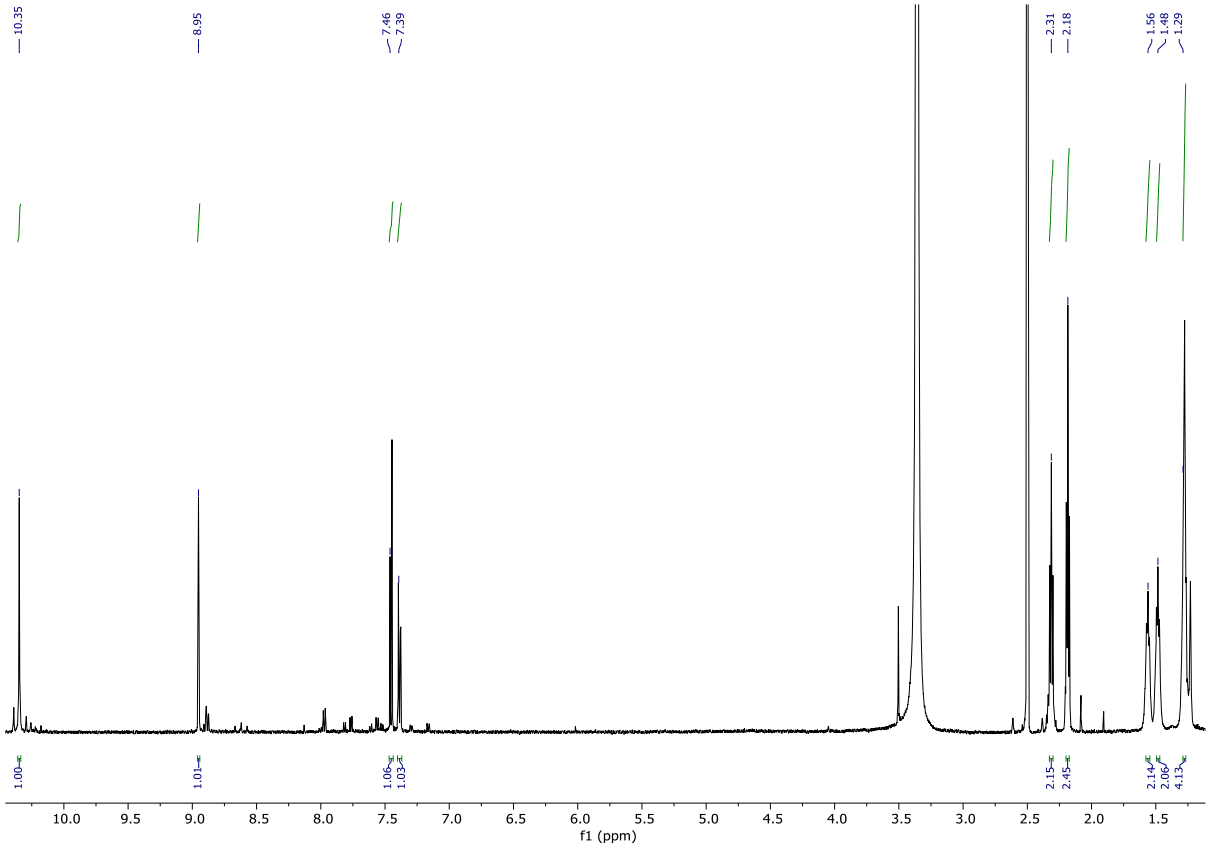

*Figure 63: ^{1}H NMR spectrum of **73** in DMSO-d_6.*

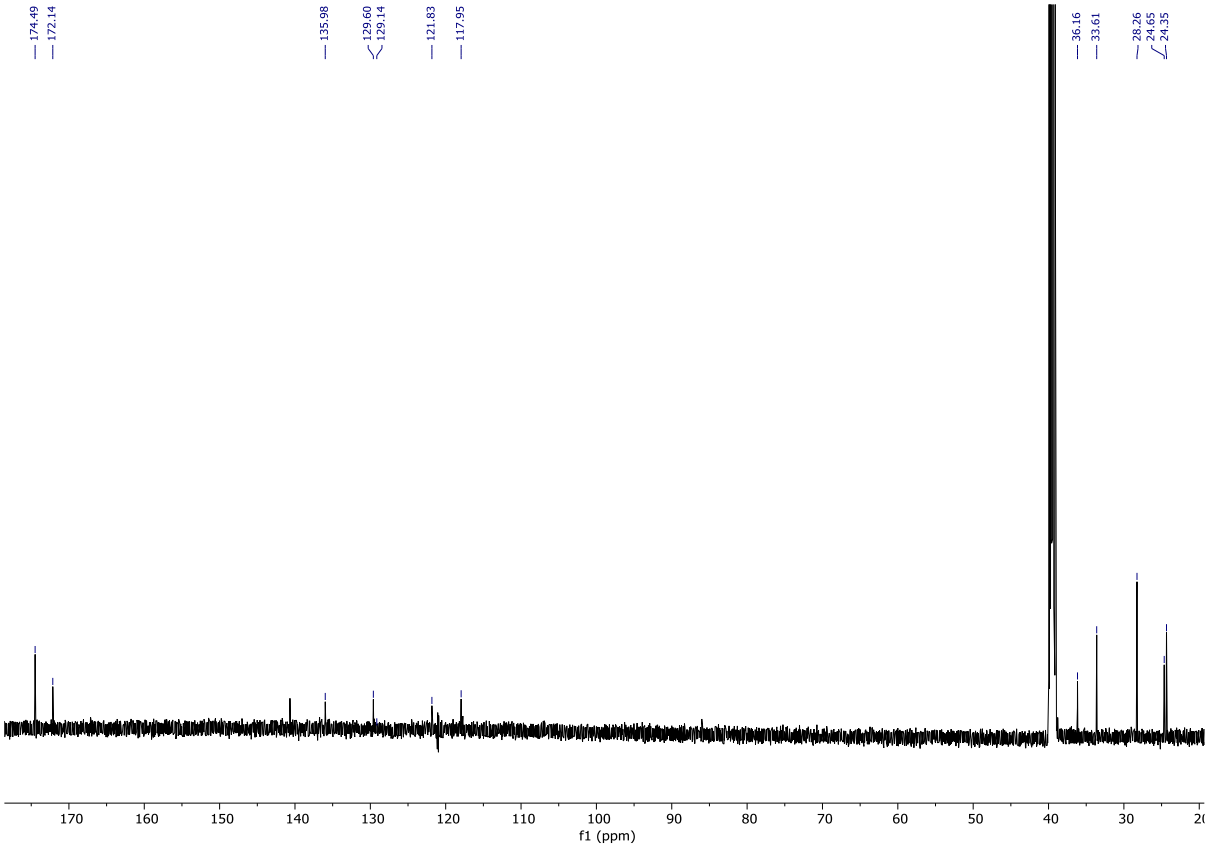

*Figure 64: ^{13}C NMR spectrum of **73** in DMSO-d_6.*

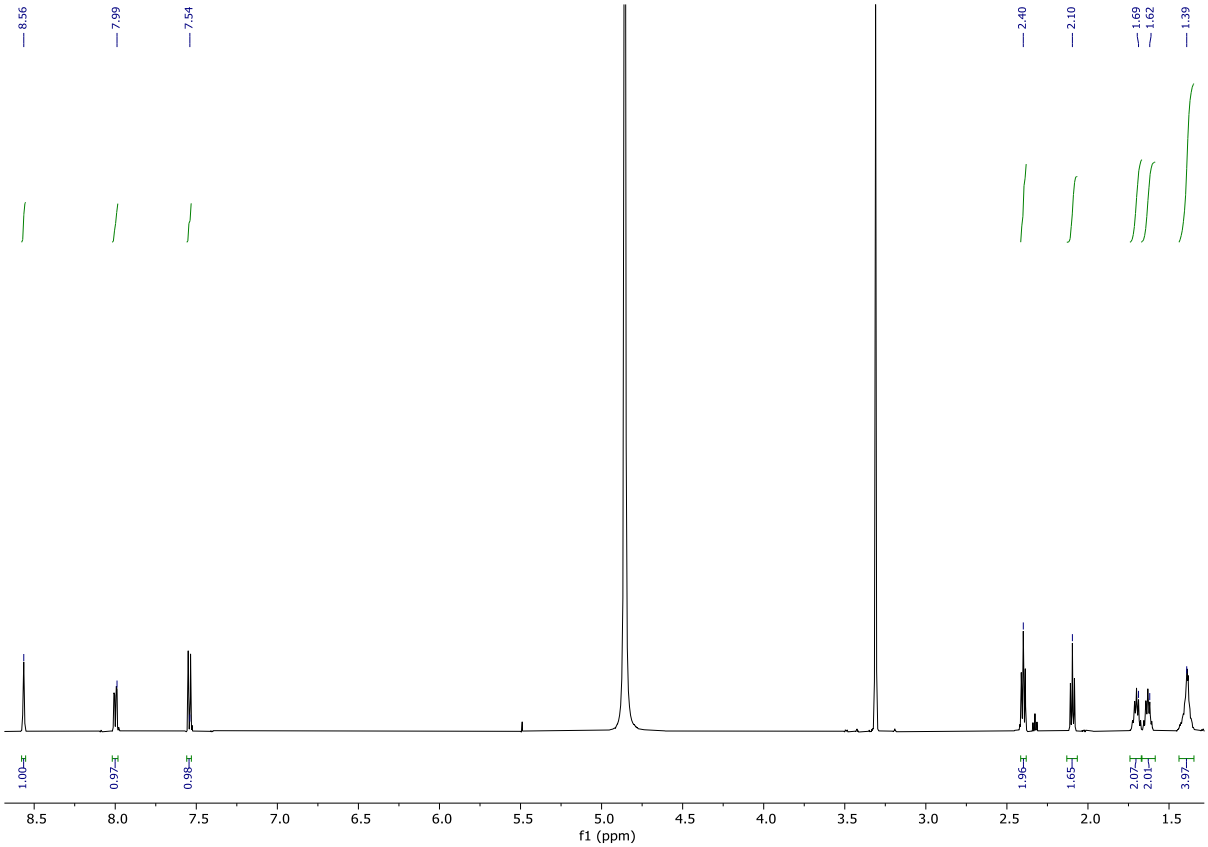

*Figure 65: ^{1}H NMR spectrum of **81** in MeOD.*

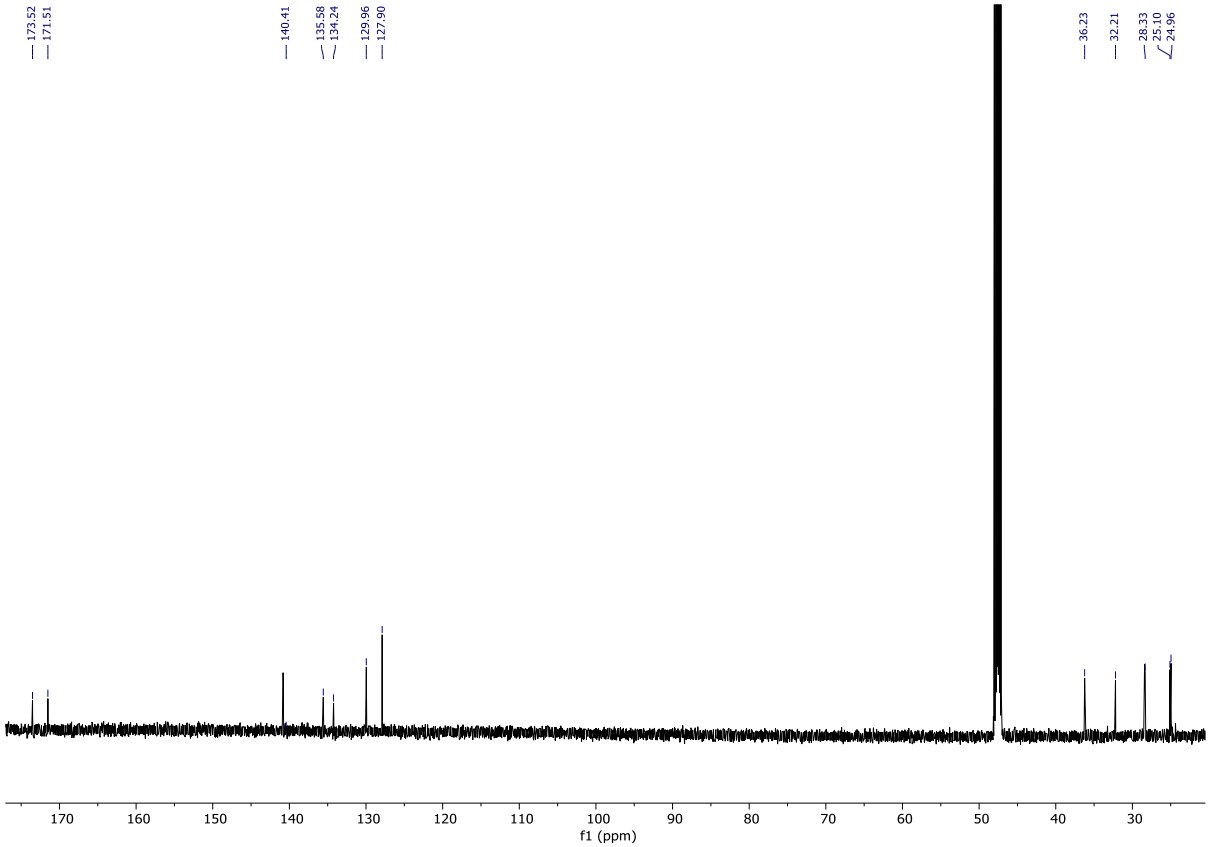

*Figure 66: ^{13}C NMR spectrum of **81** in MeOD.*

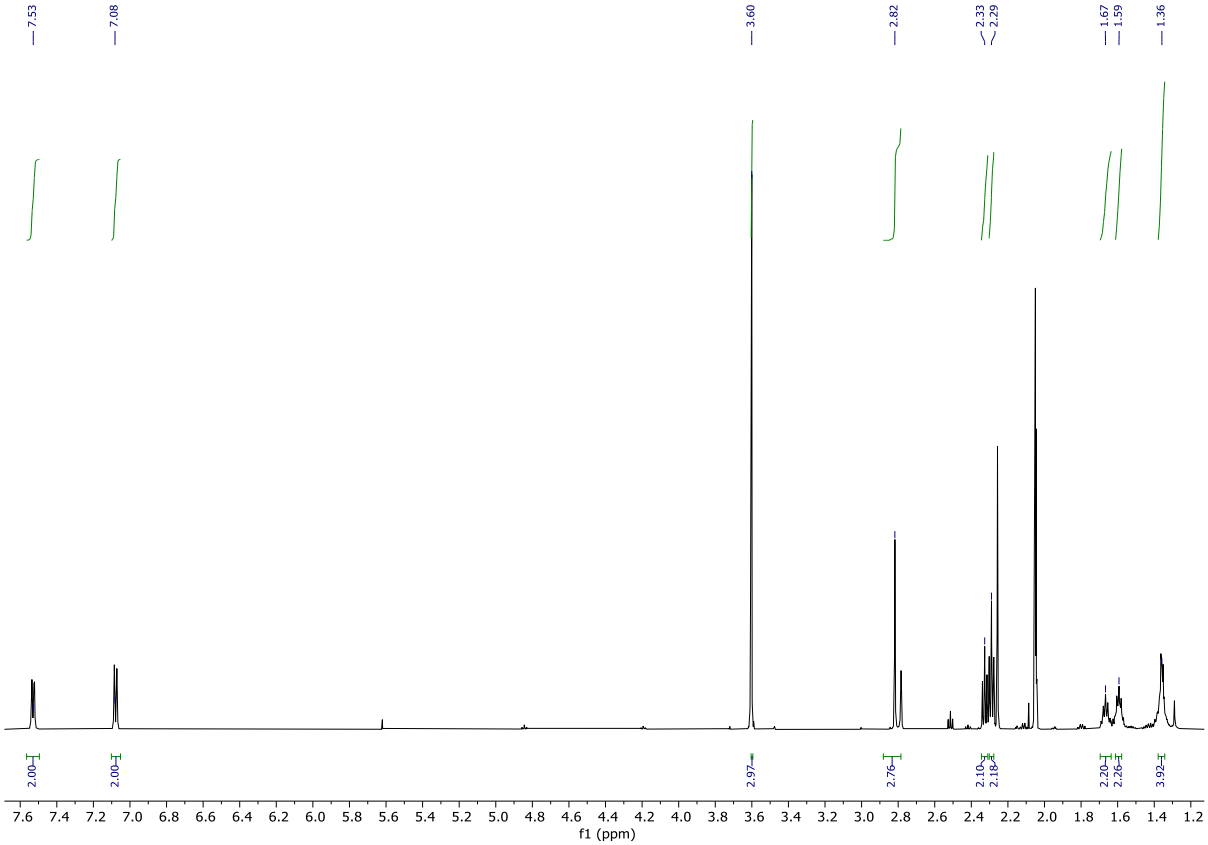

*Figure 67: ^{1}H NMR spectrum of **85** in acetone-d_6.*

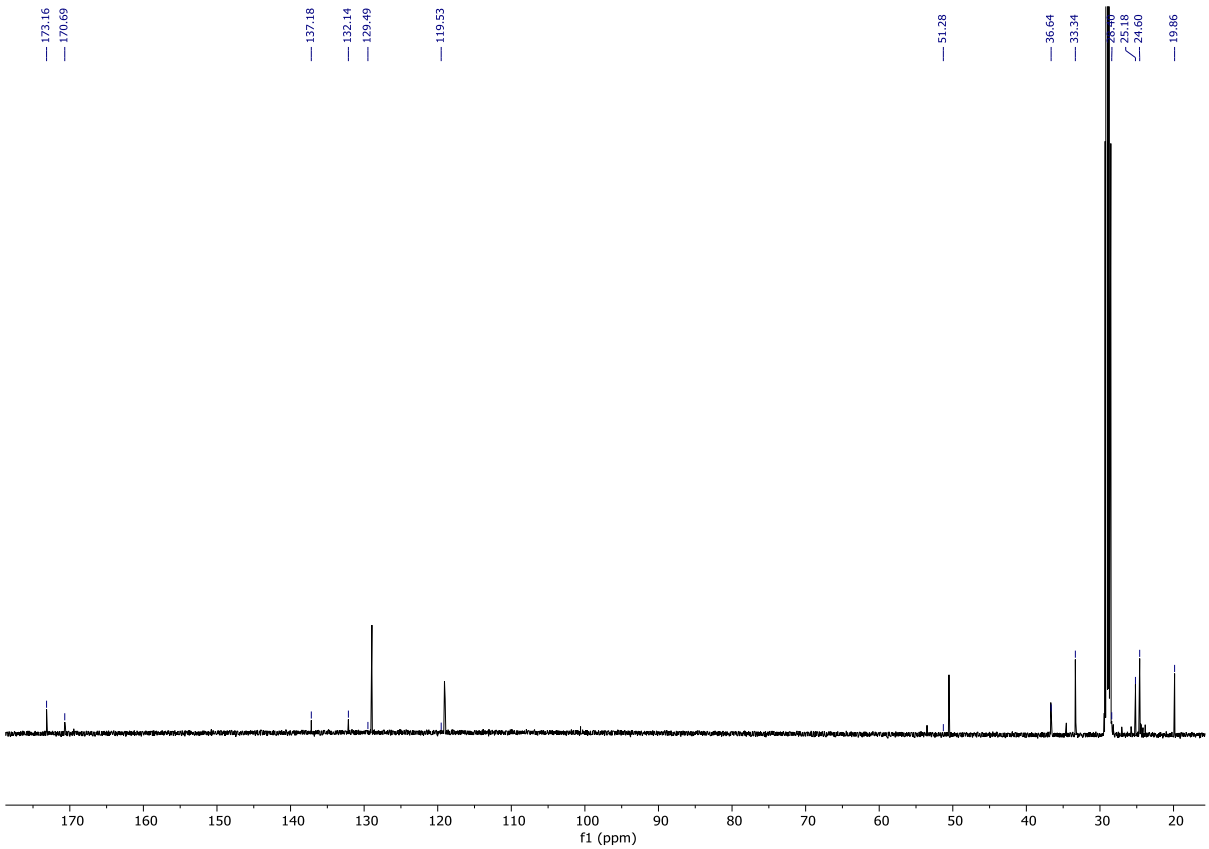

*Figure 68: ^{13}C NMR spectrum of **85** in acetone-d_6.*

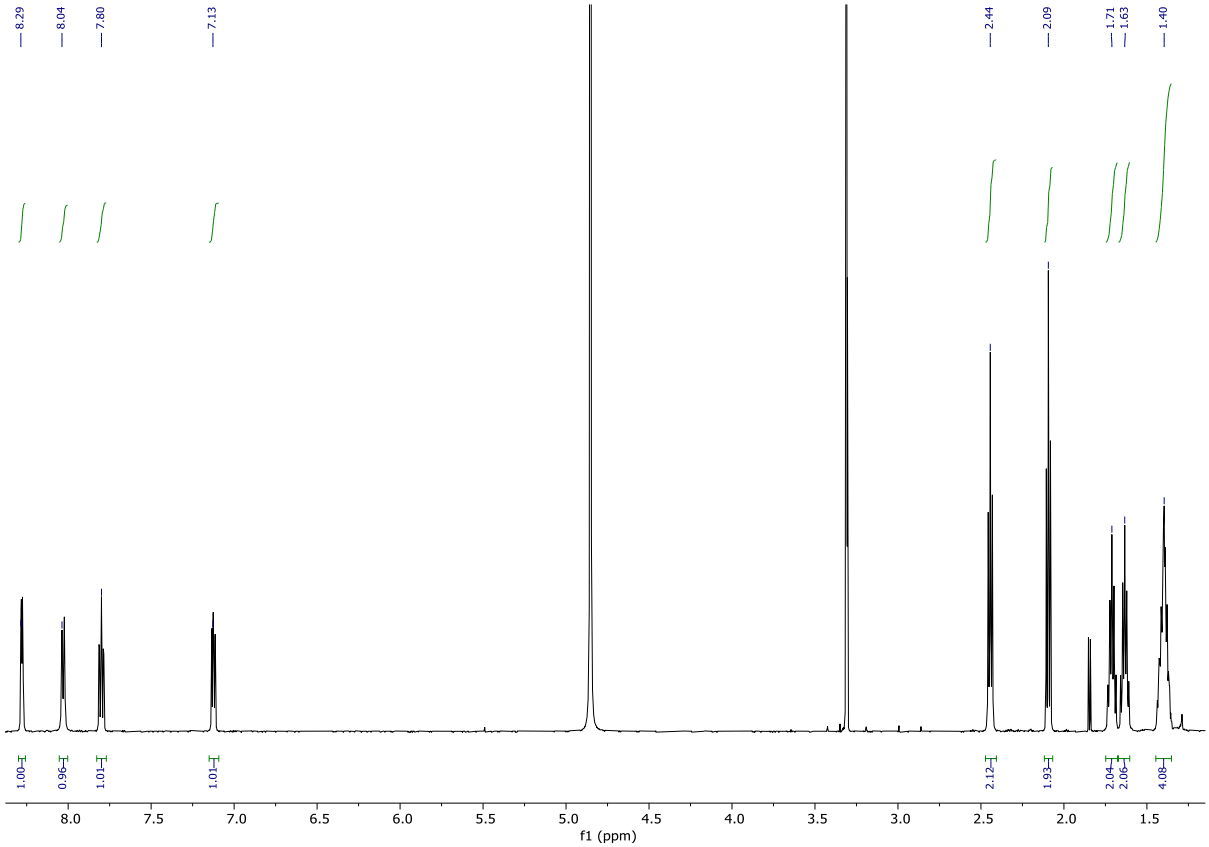

*Figure 69: ^{1}H NMR spectrum of **103** in MeOD.*

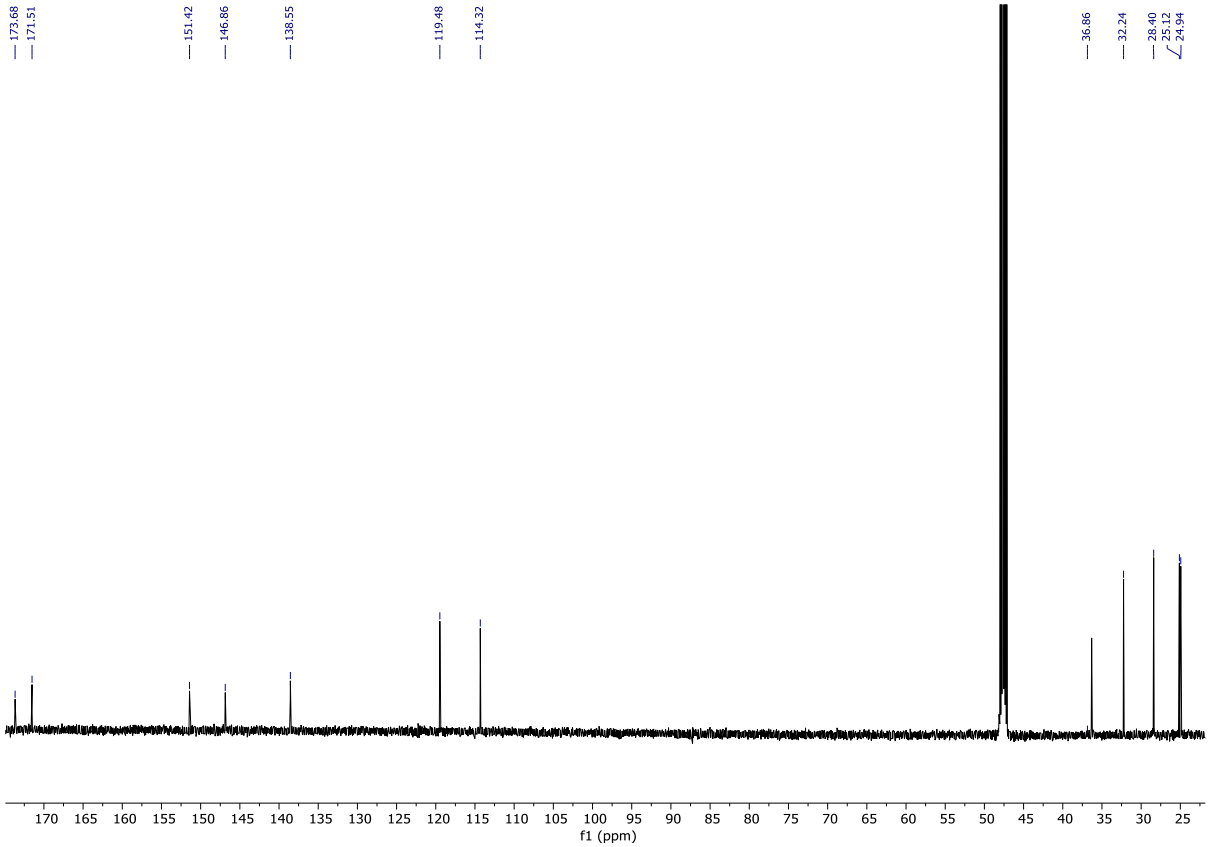

*Figure 70: ^{13}C NMR spectrum of **103** in MeOD.*

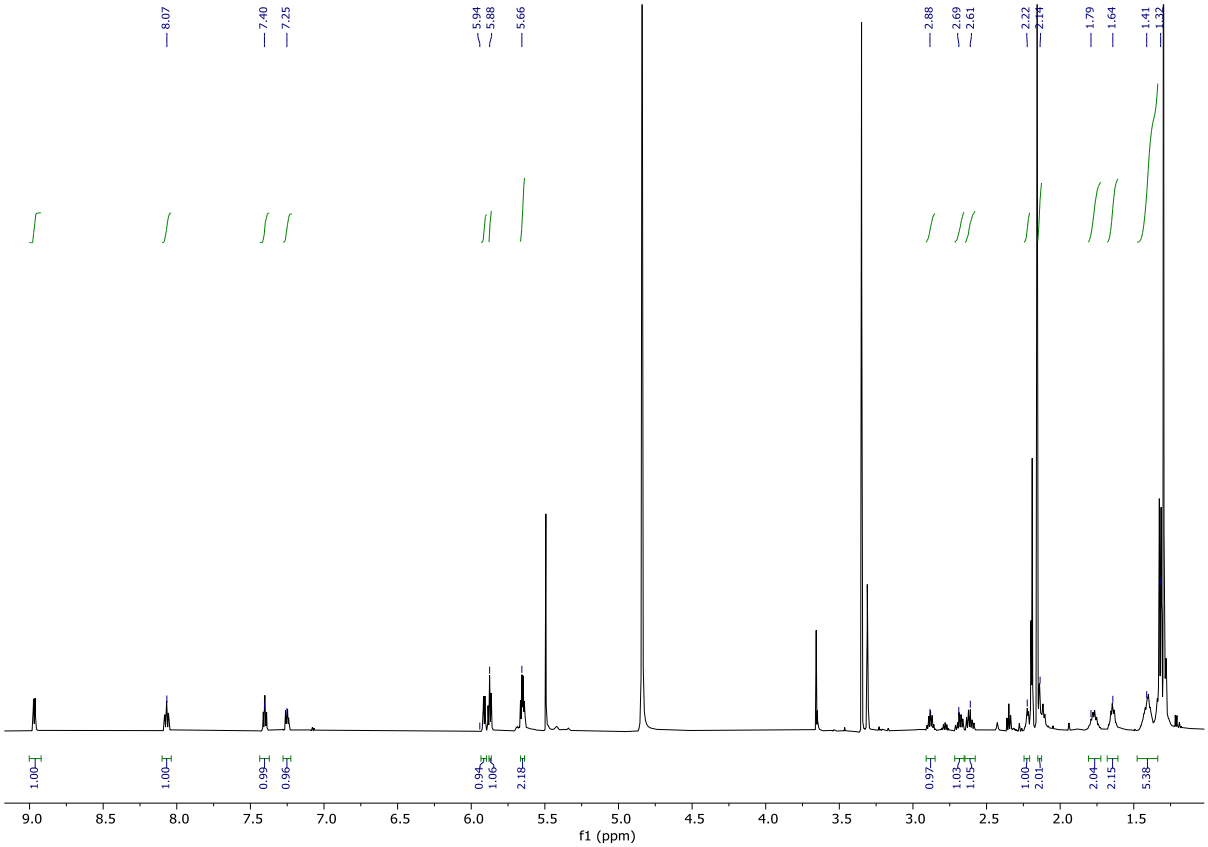

*Figure 71: ^{1}H NMR spectrum of **105** in MeOD.*

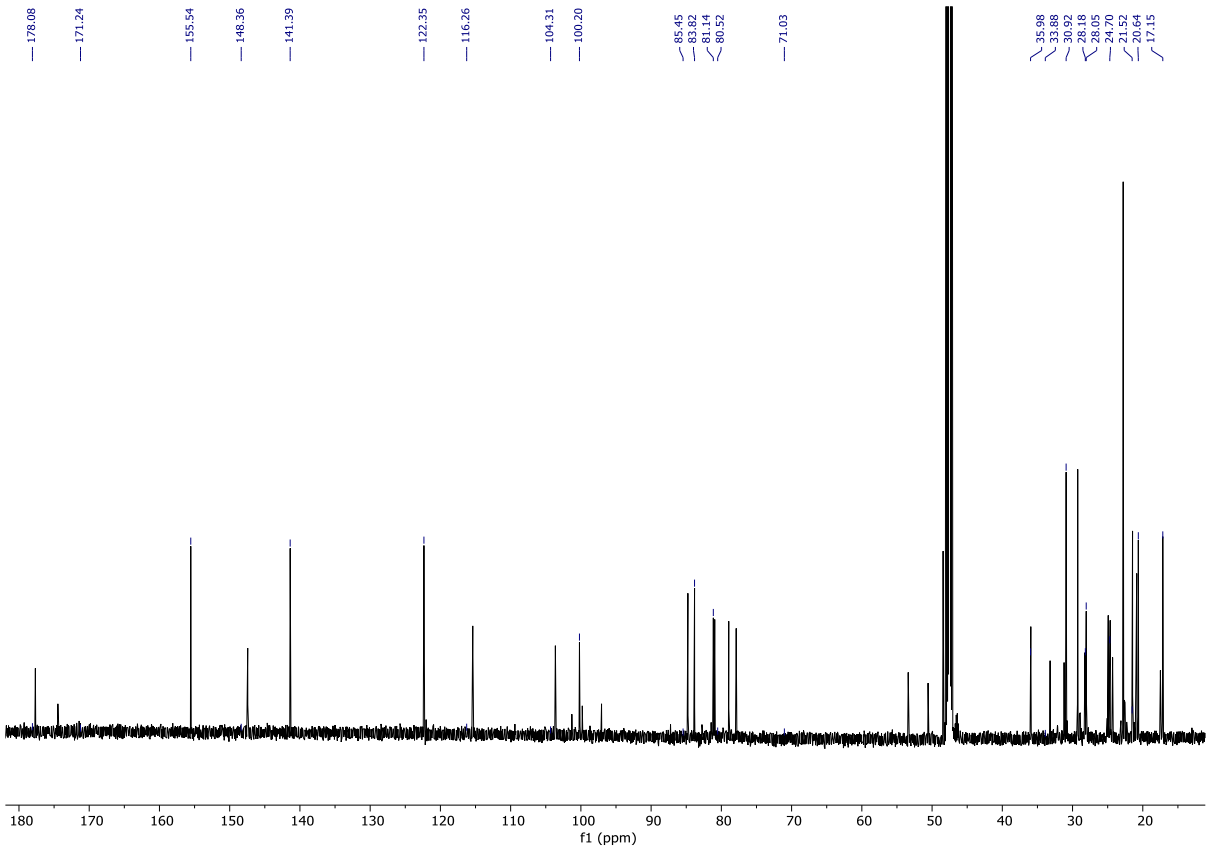

*Figure 72: ^{13}C NMR spectrum of **105** in MeOD.*

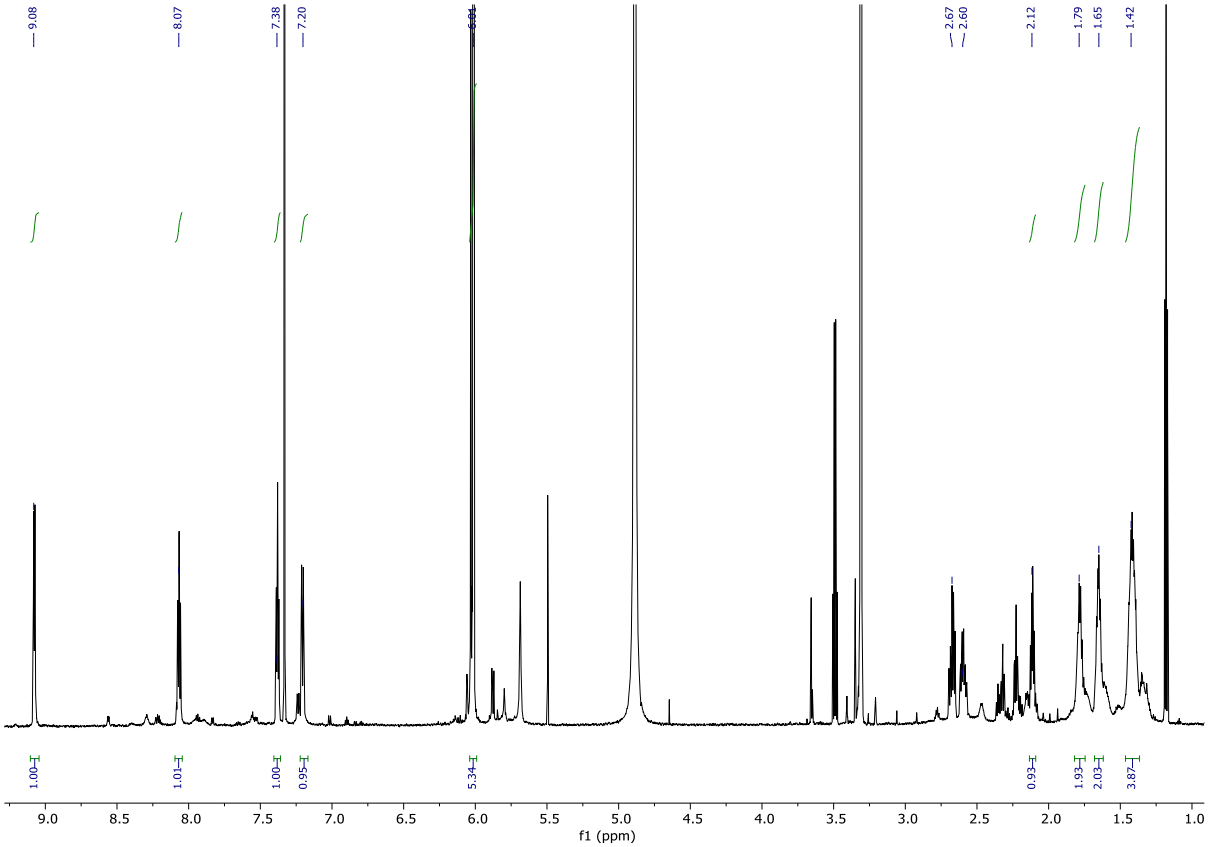

*Figure 73: ^{1}H NMR spectrum of **106** in MeOD.*

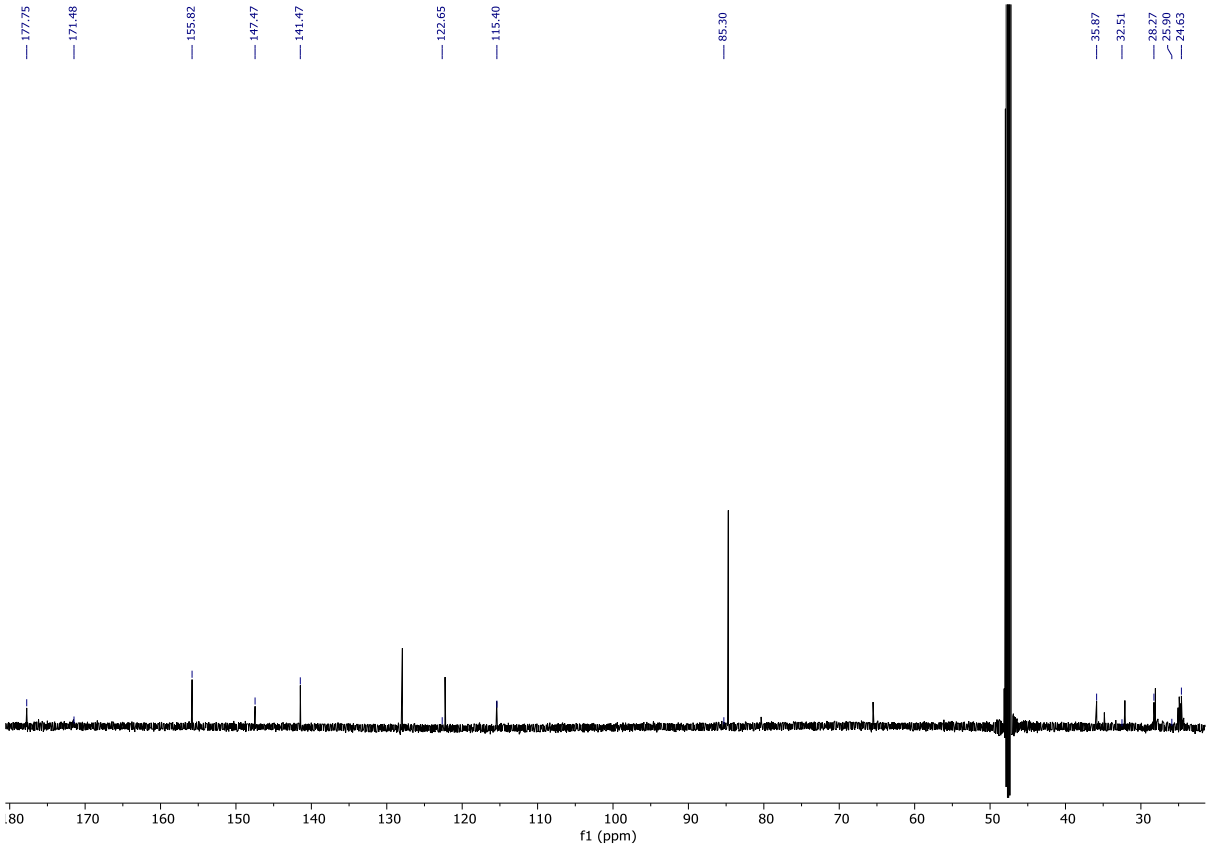

*Figure 74: ^{13}C NMR spectrum of **106** in MeOD.*

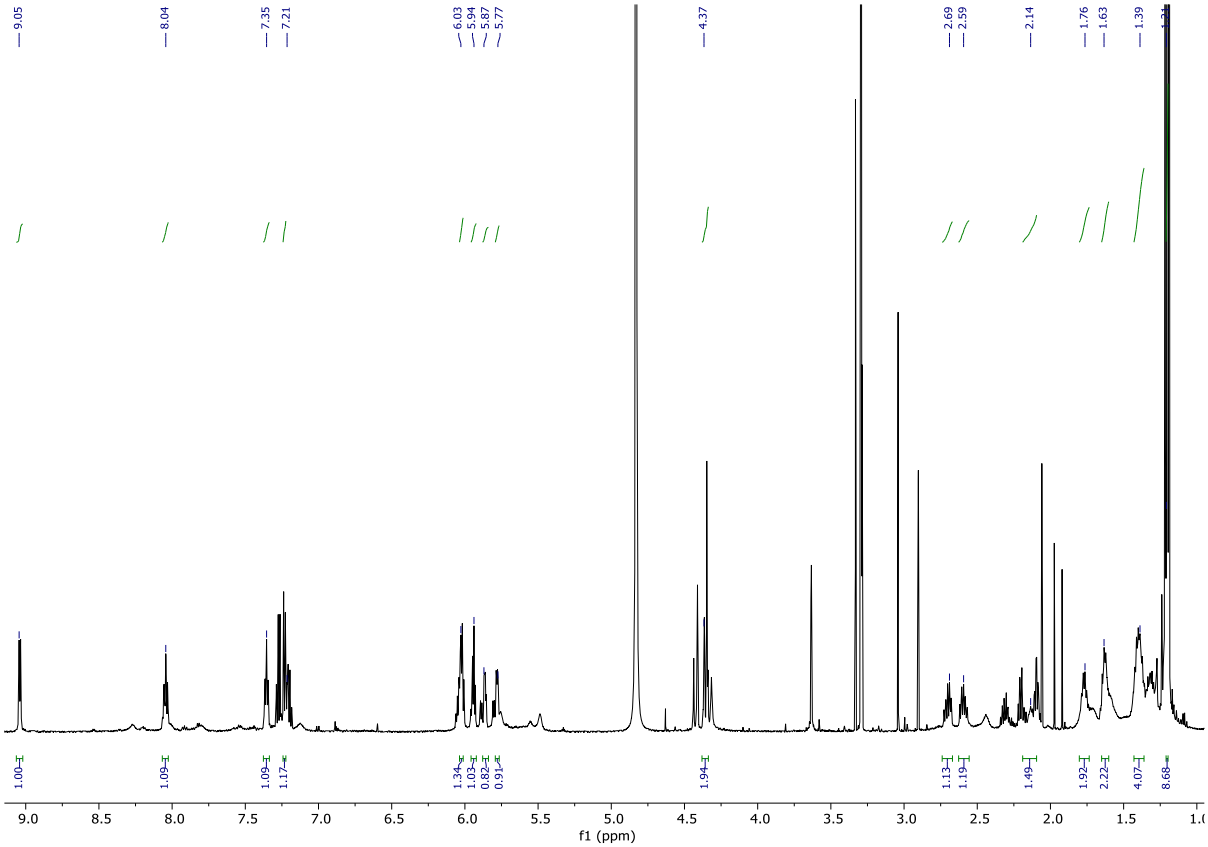

*Figure 75: ^{1}H NMR spectrum of **108** in MeOD.*

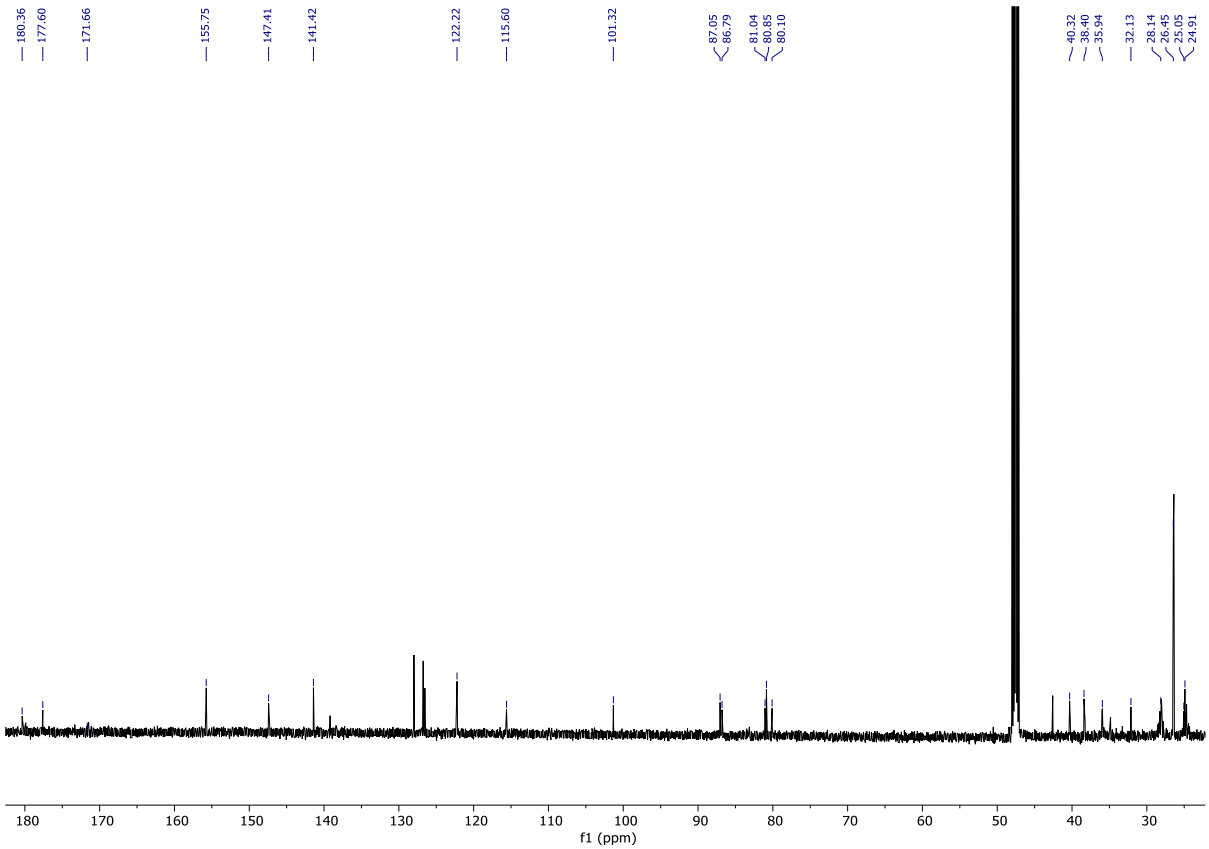

*Figure 76: ^{13}C NMR spectrum of **108** in MeOD.*

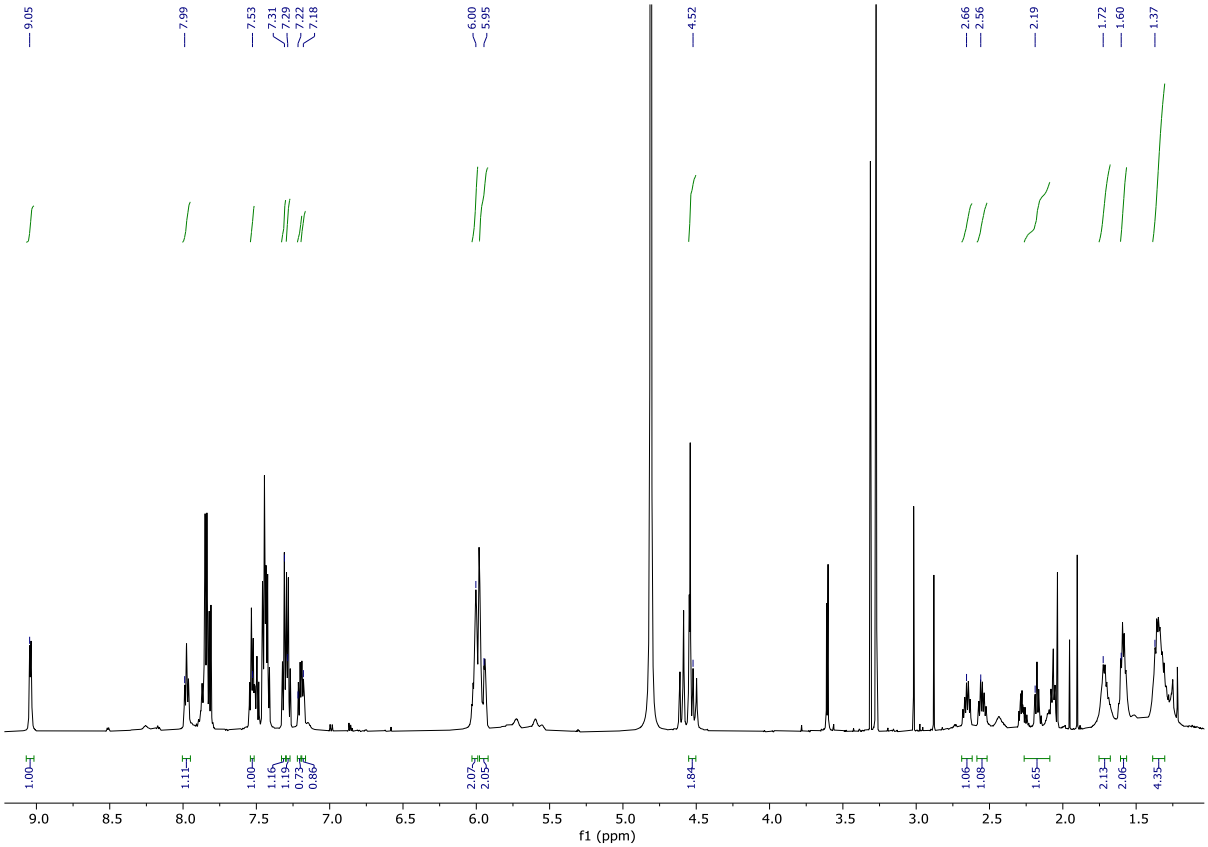

*Figure 77: ^{1}H NMR spectrum of **109** in MeOD.*

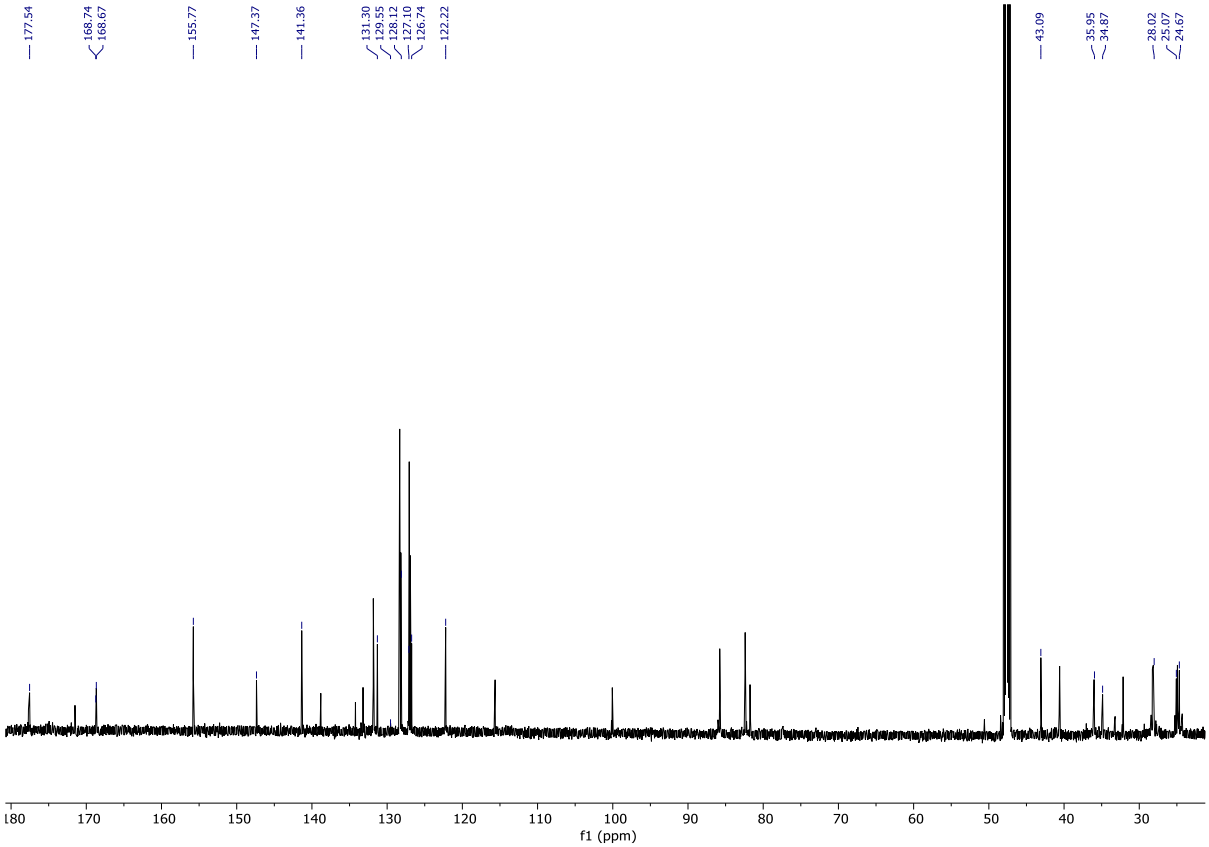

*Figure 78: ^{13}C NMR spectrum of **109** in MeOD.*

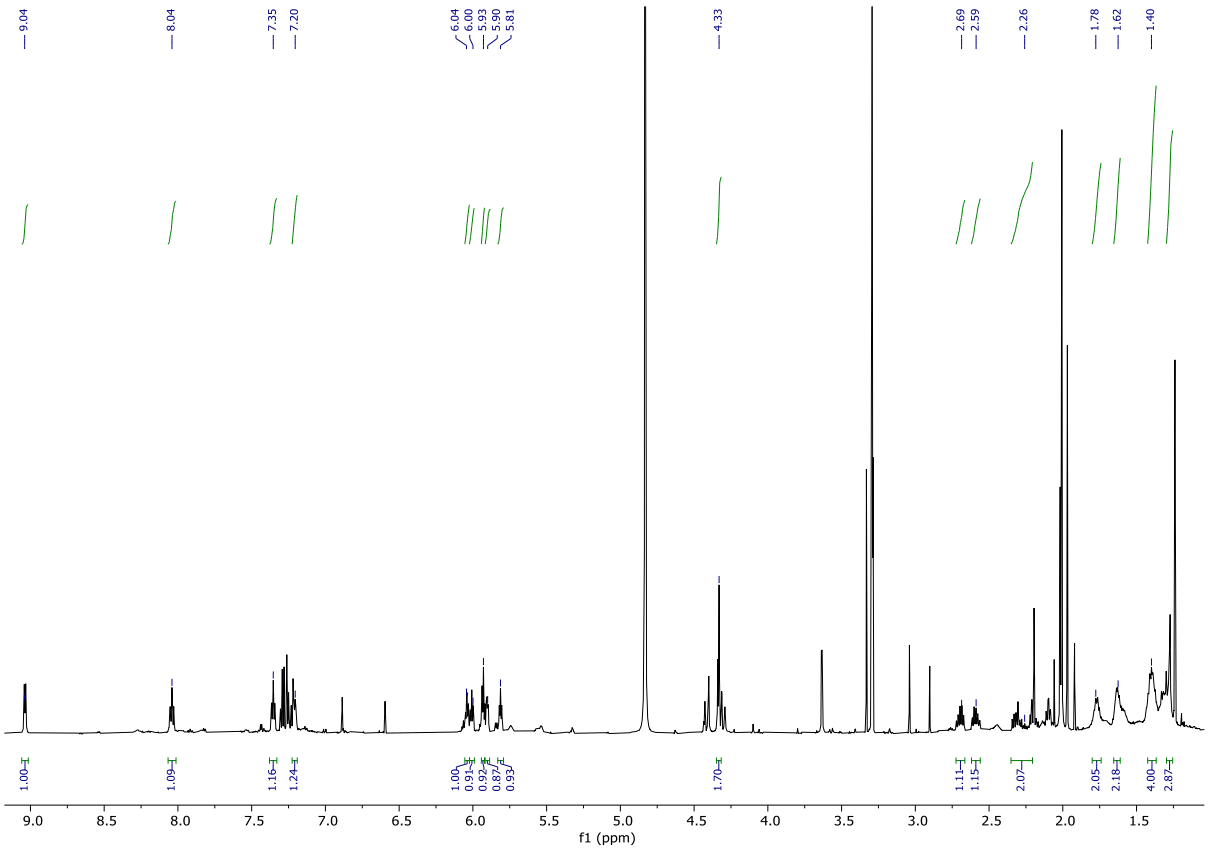

*Figure 79: ^{1}H NMR spectrum of **110** in MeOD.*

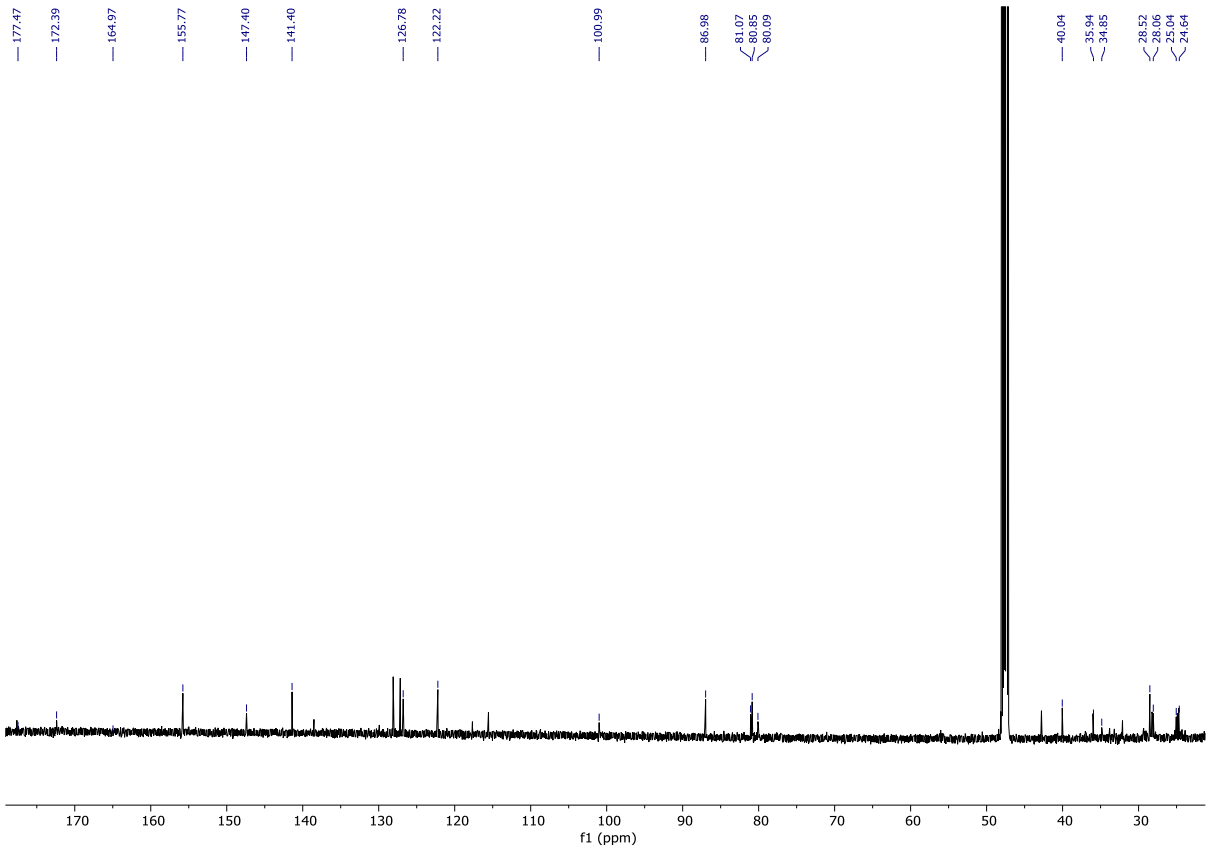

*Figure 80: ^{13}C NMR spectrum of **110** in MeOD.*

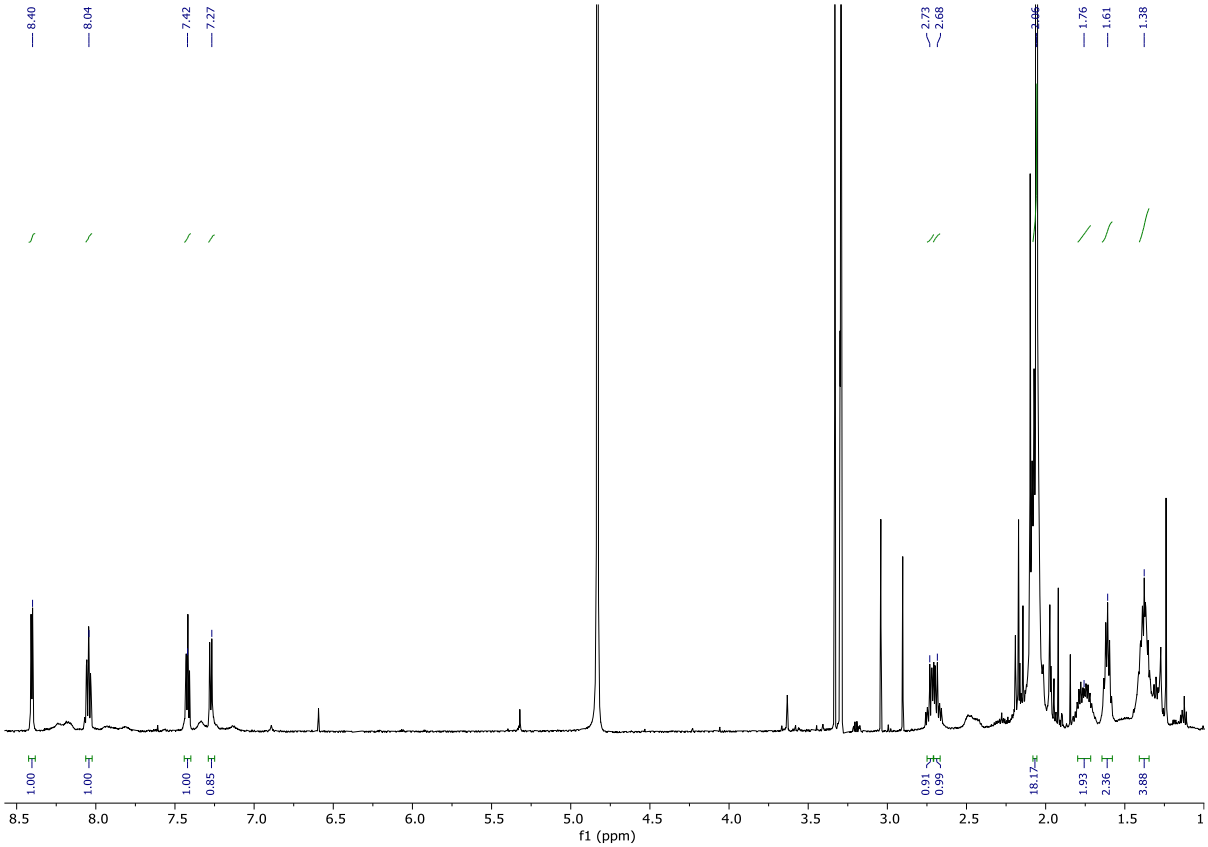

*Figure 81: ^{1}H NMR spectrum of **111** in MeOD.*

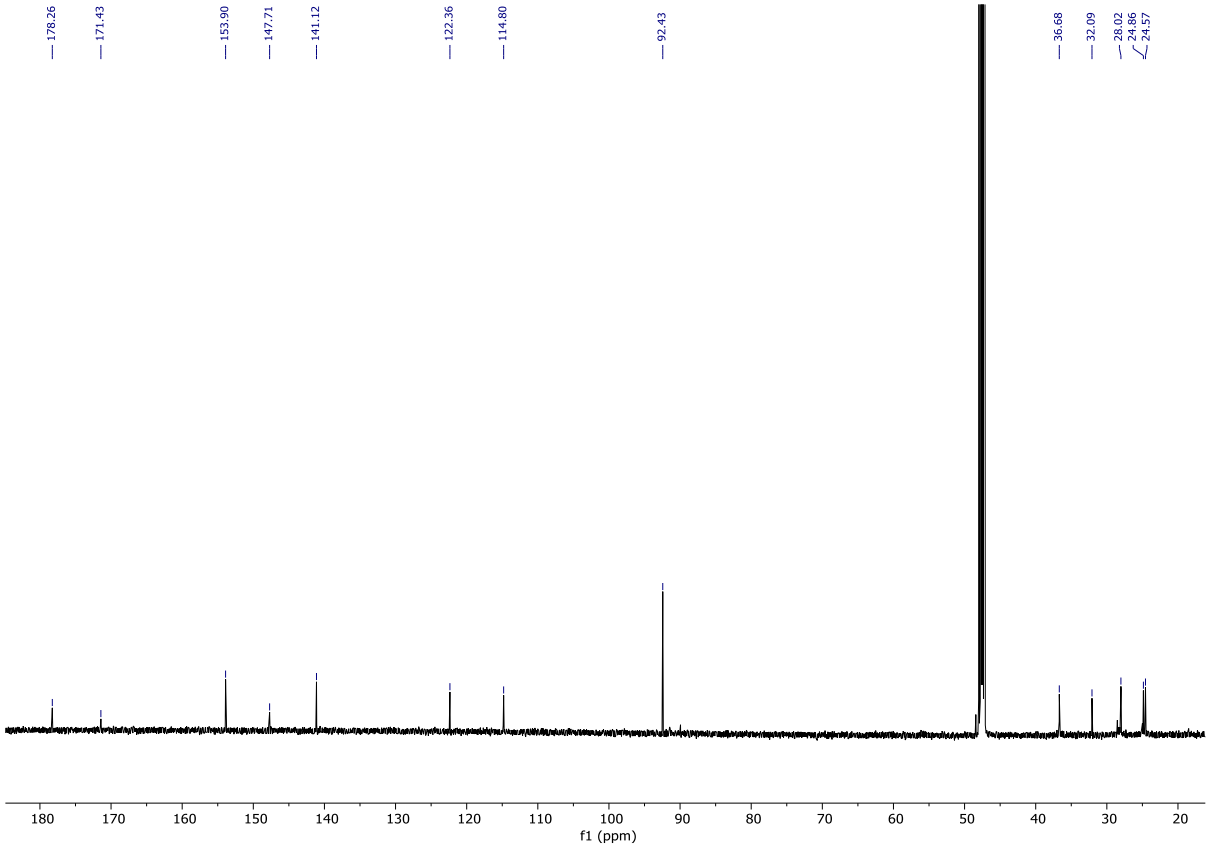

*Figure 82: ^{13}C NMR spectrum of **111** in MeOD.*

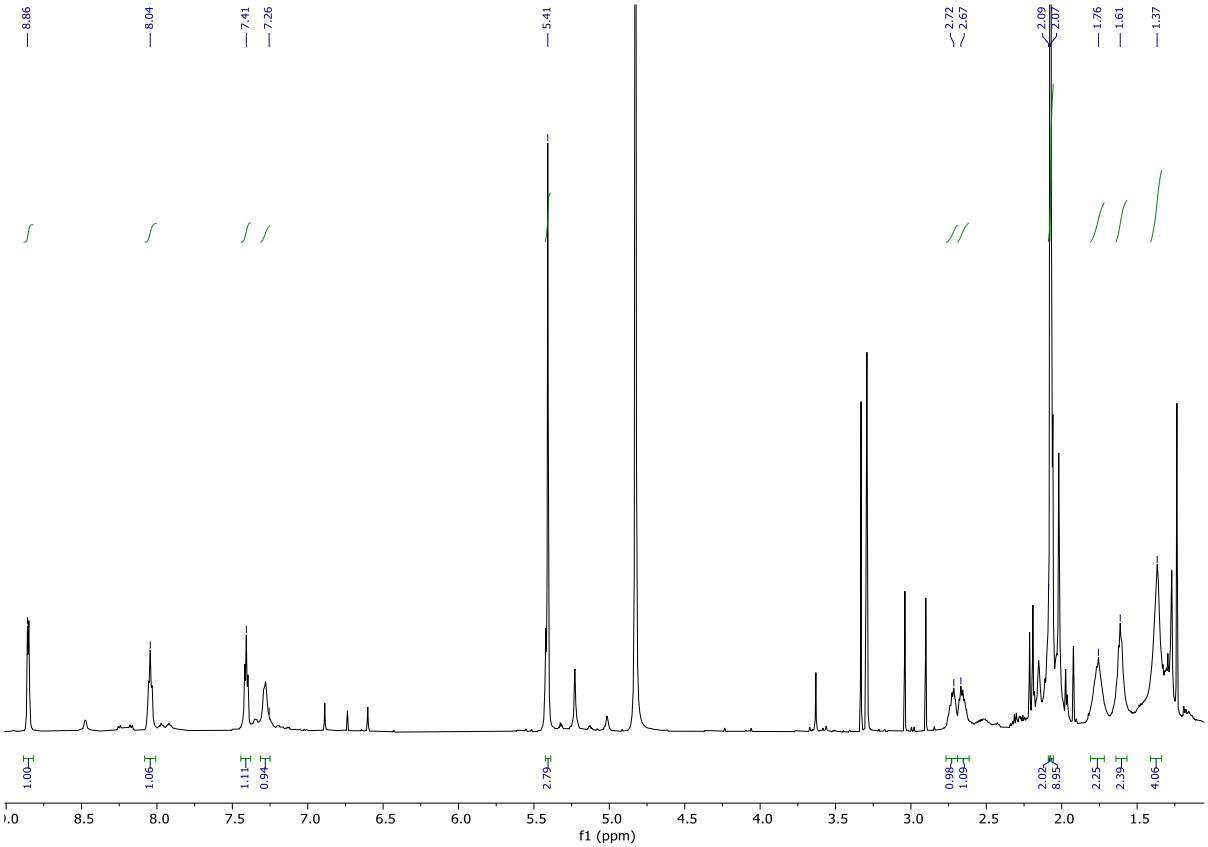

*Figure 83: ^{1}H NMR spectrum of **112** in MeOD.*

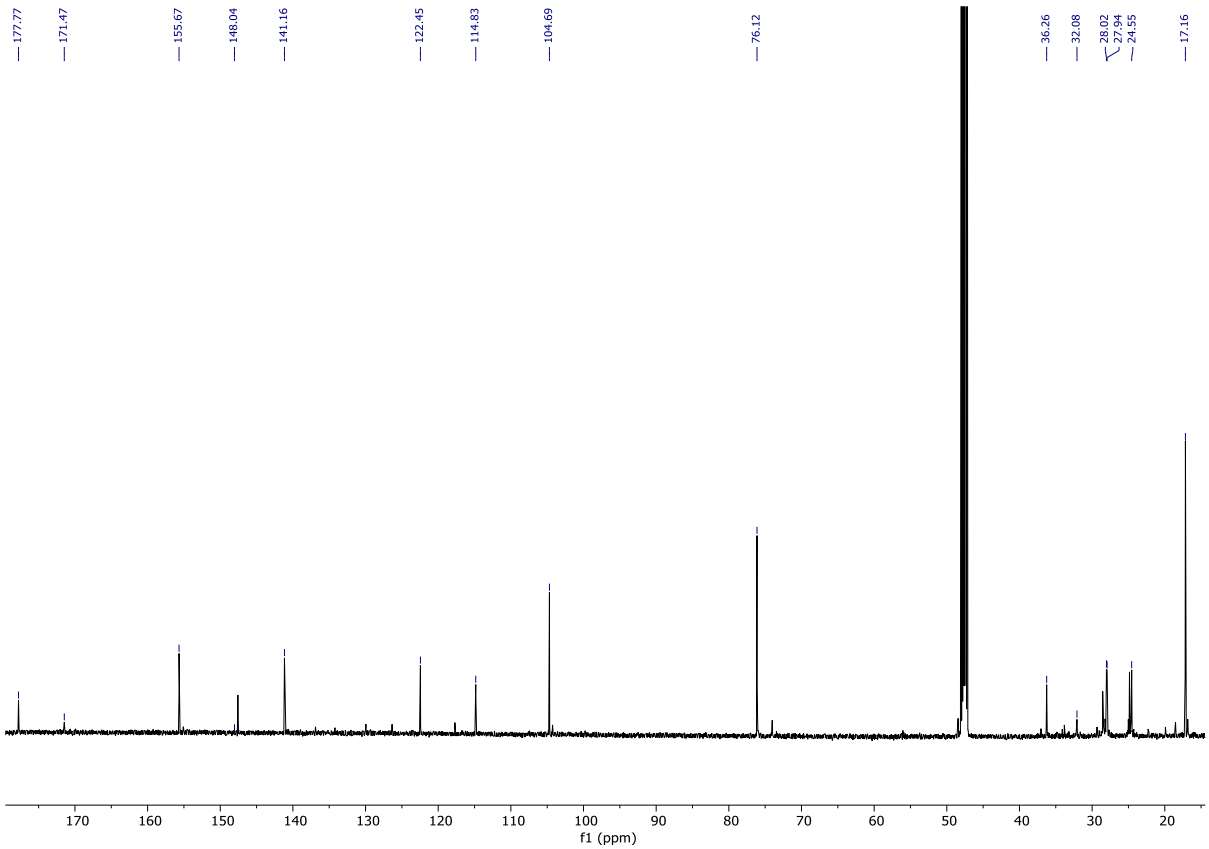

*Figure 84: ^{13}C NMR spectrum of **112** in MeOD.*

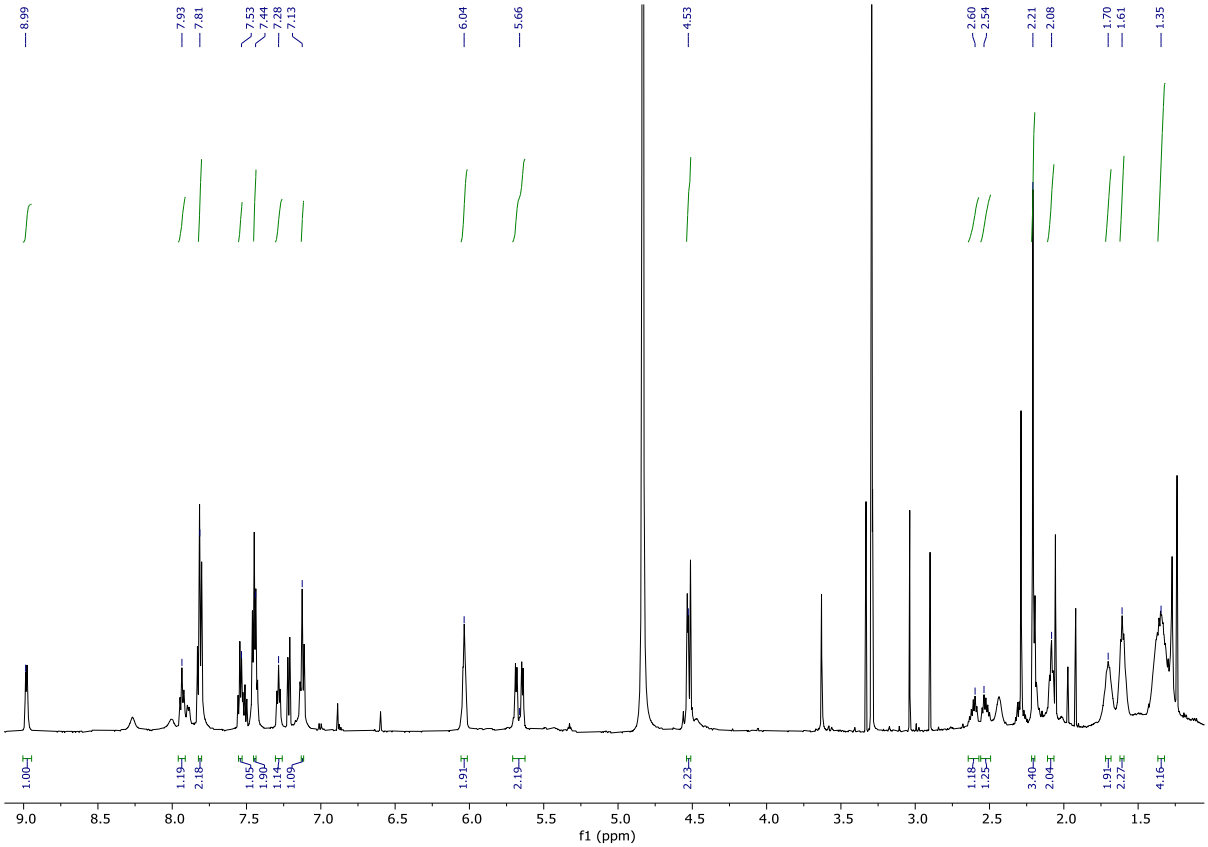

*Figure 85: ^{1}H NMR spectrum of **113** in MeOD.*

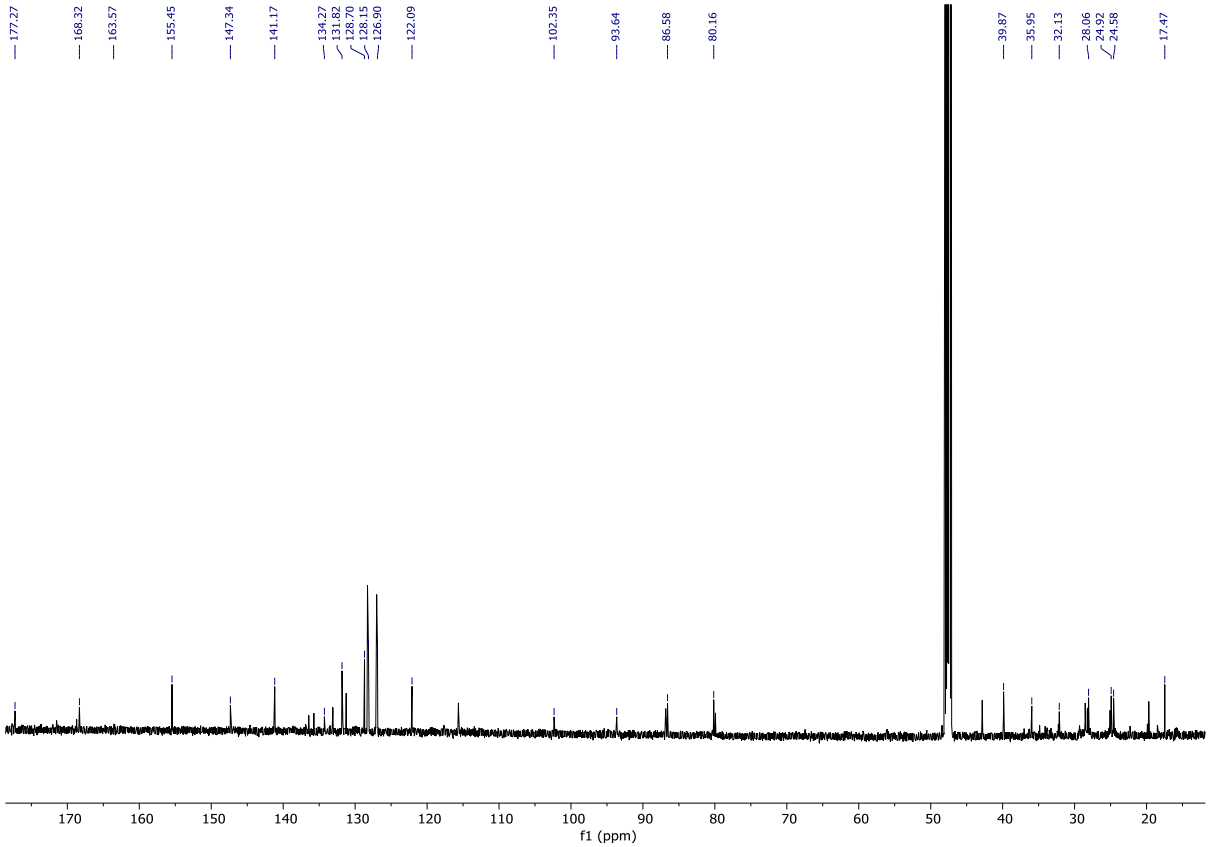

*Figure 86: ^{13}C NMR spectrum of **113** in MeOD.*

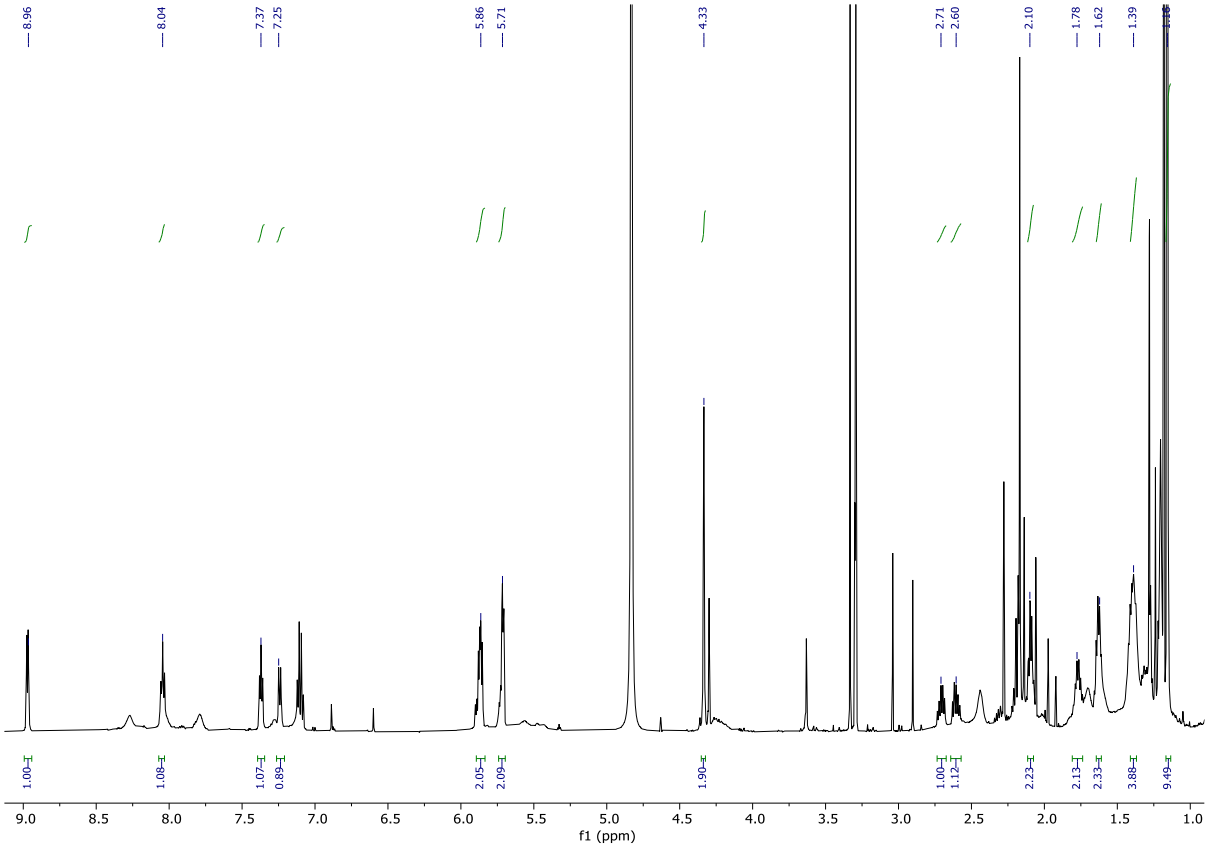

*Figure 87: ^{1}H NMR spectrum of **114** in MeOD.*

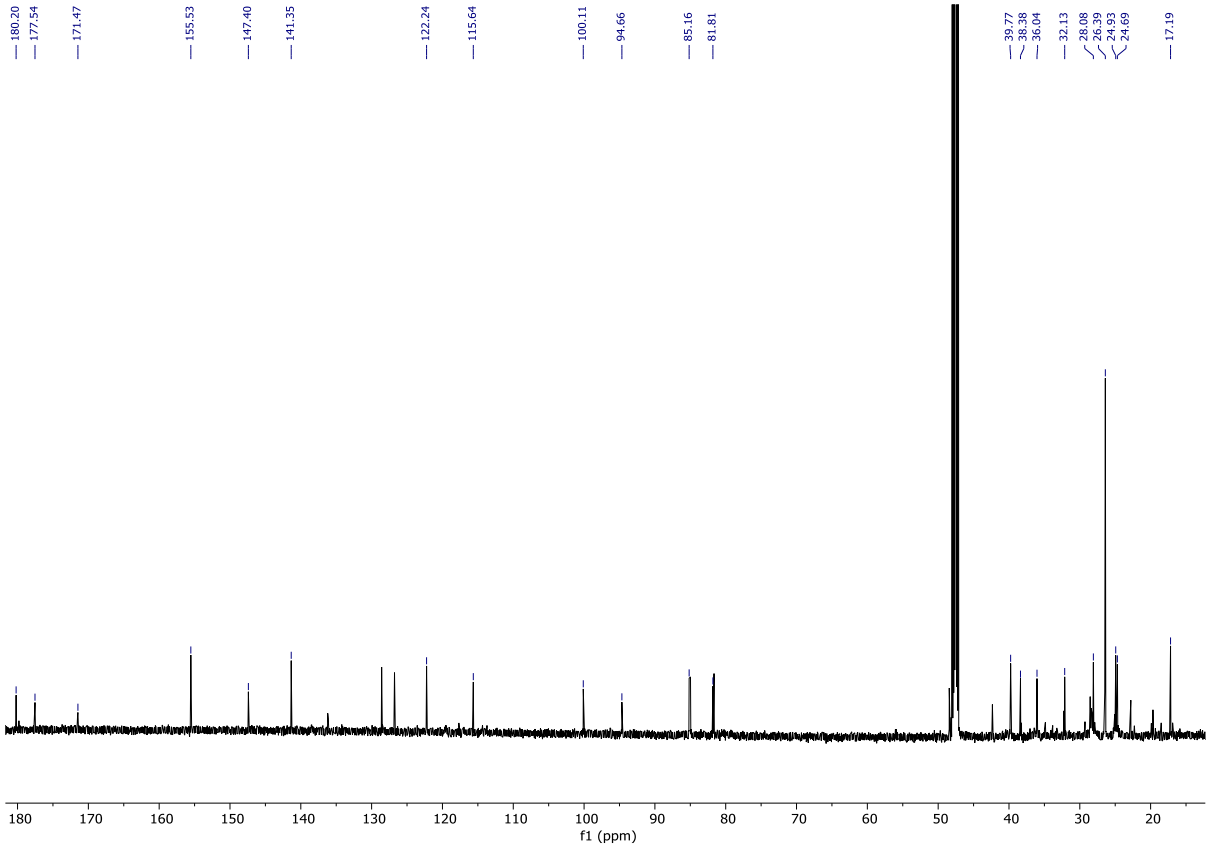

*Figure 88: ^{13}C NMR spectrum of **114** in MeOD.*

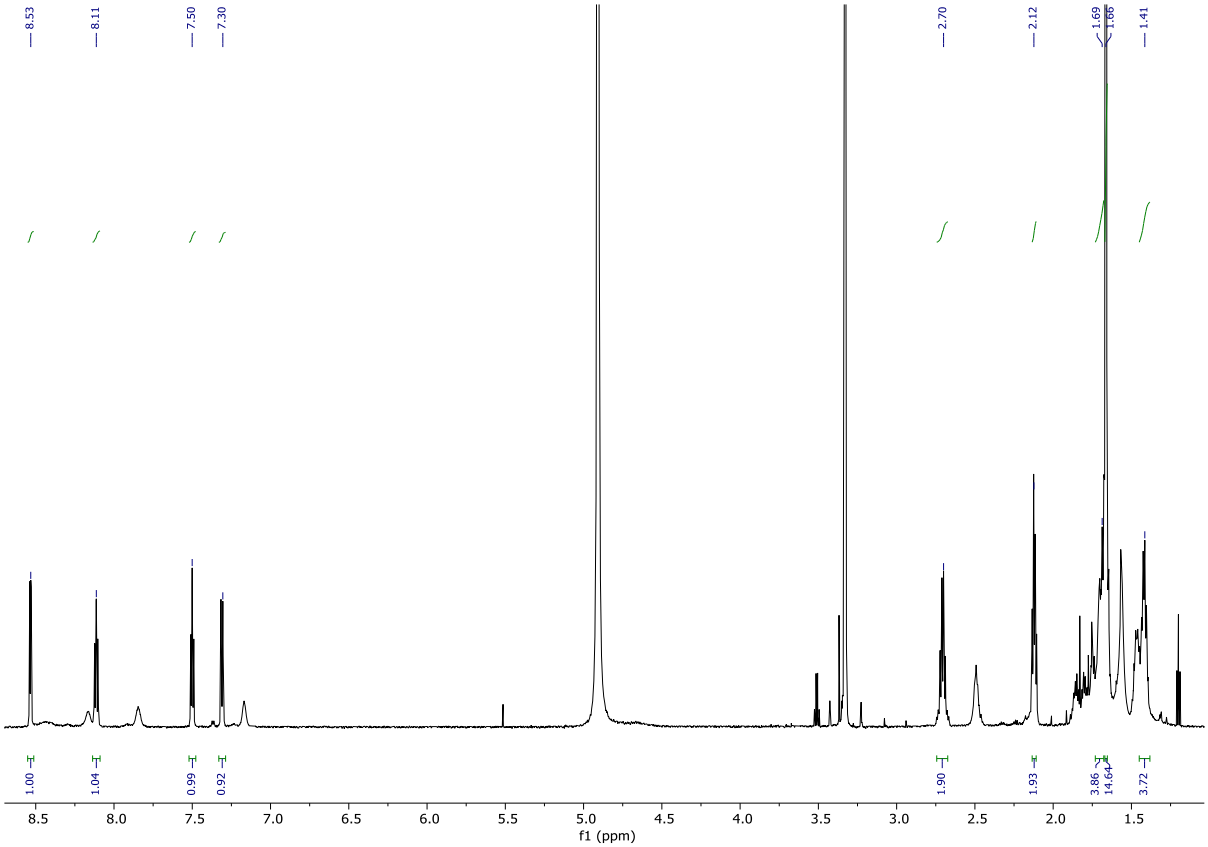

*Figure 89: ^{1}H NMR spectrum of **116** in MeOD.*

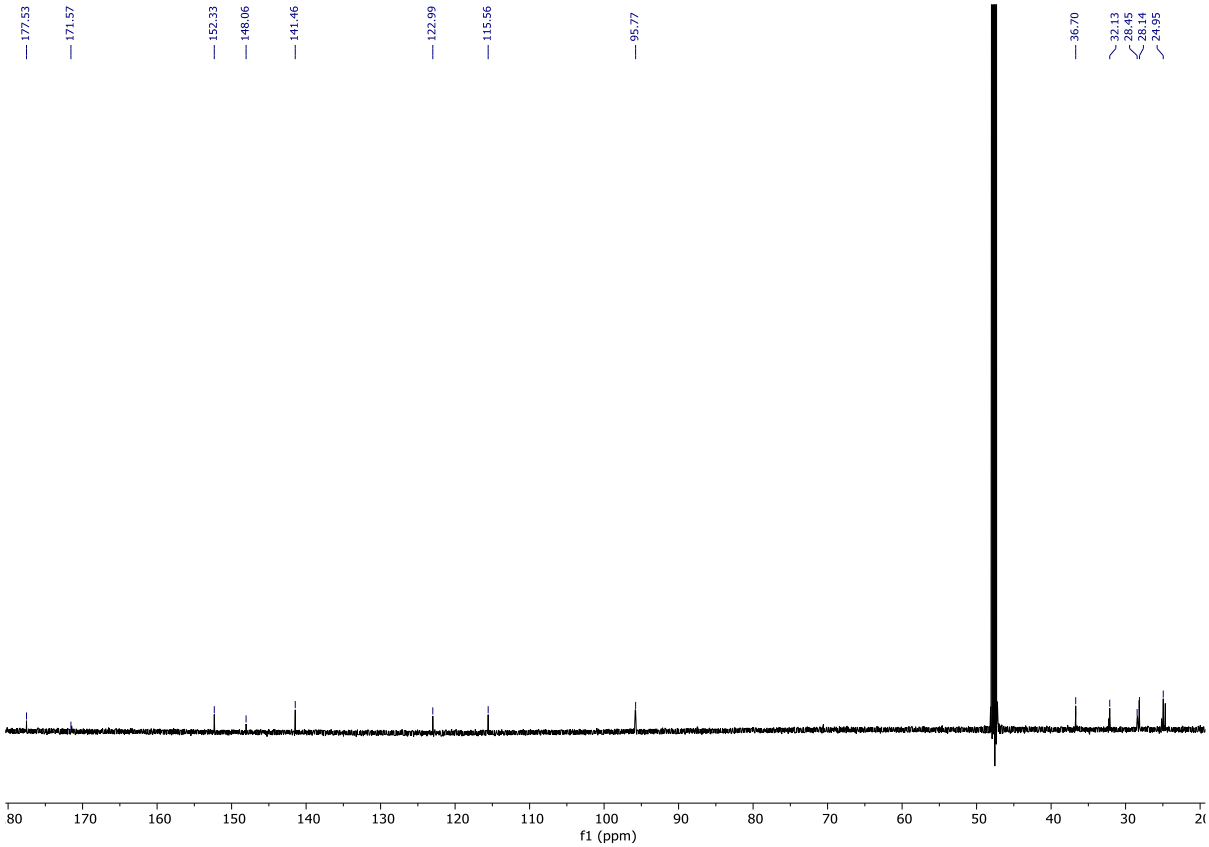

*Figure 90: ^{13}C NMR spectrum of **116** in MeOD.*

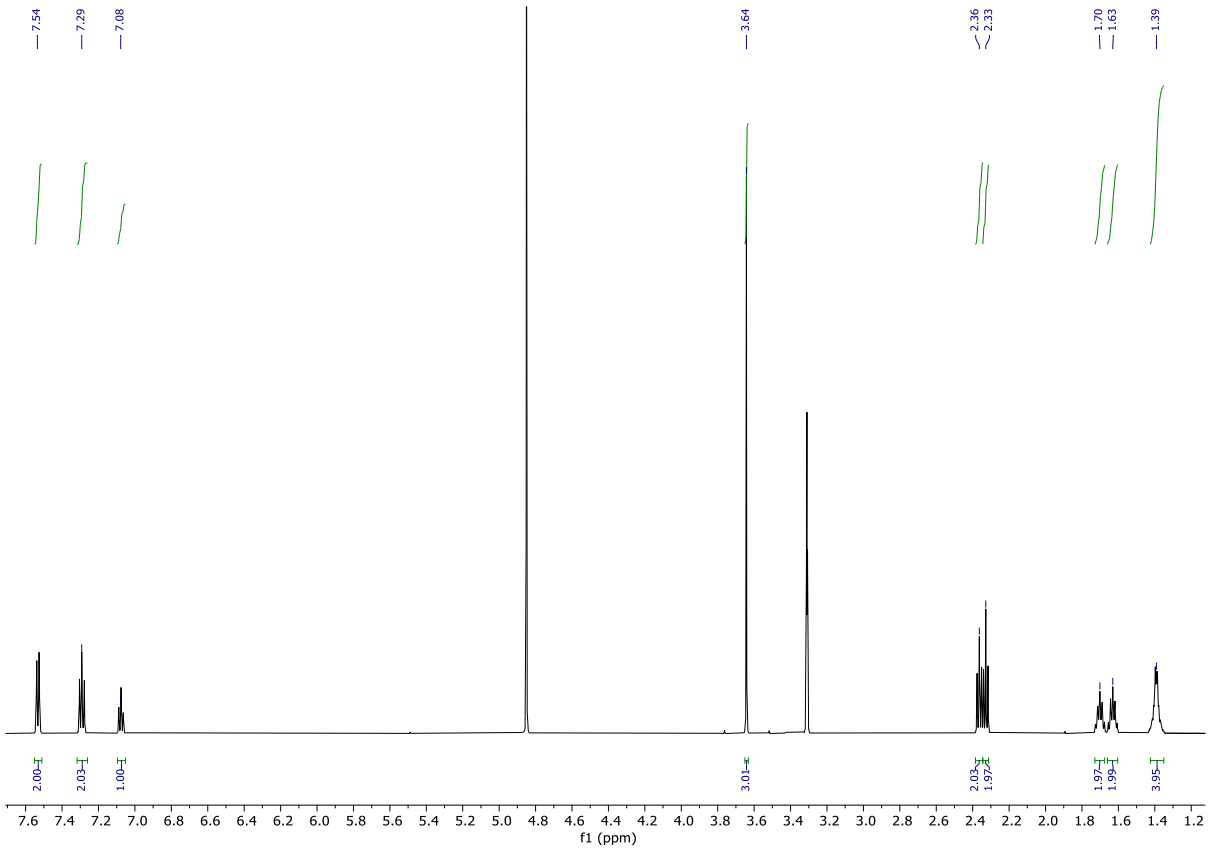

*Figure 91: ^{1}H NMR spectrum of **119** in MeOD.*

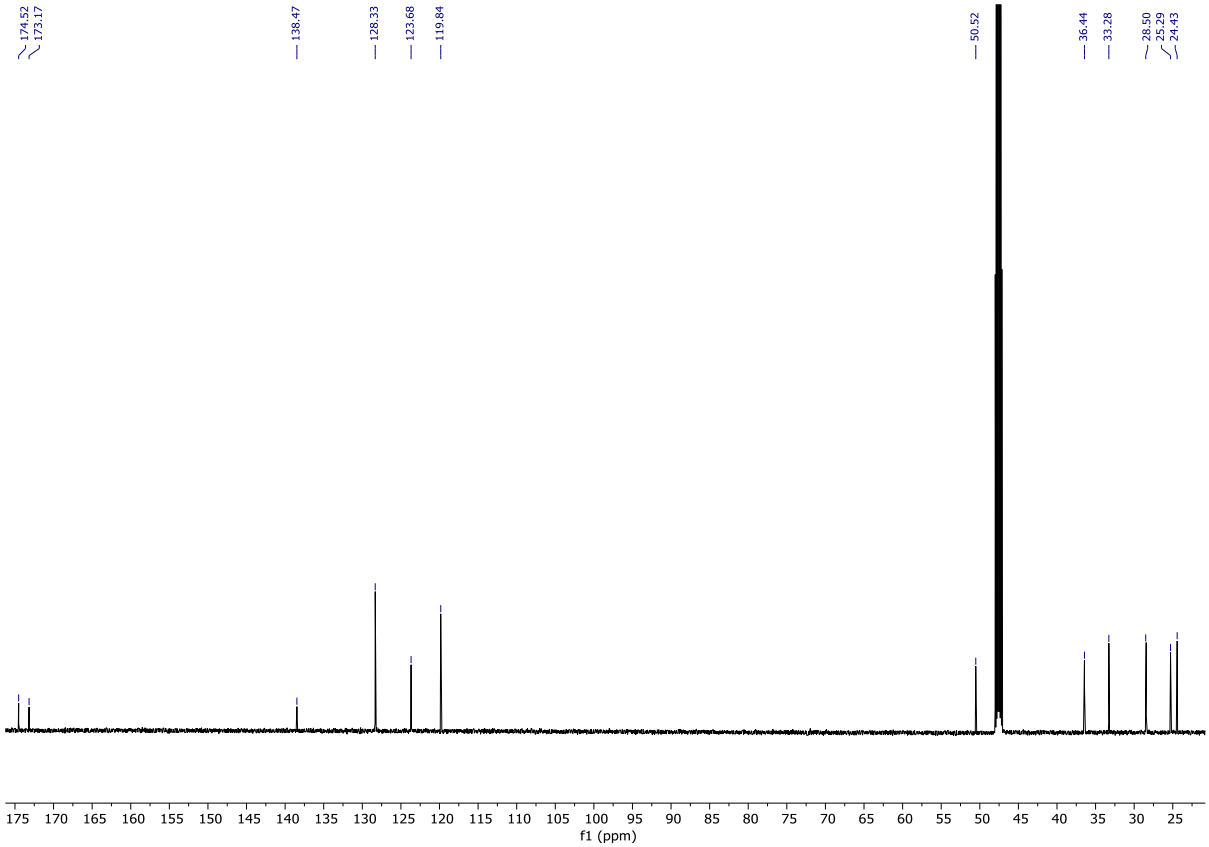

*Figure 92: ^{13}C NMR spectrum of **119** in MeOD.*

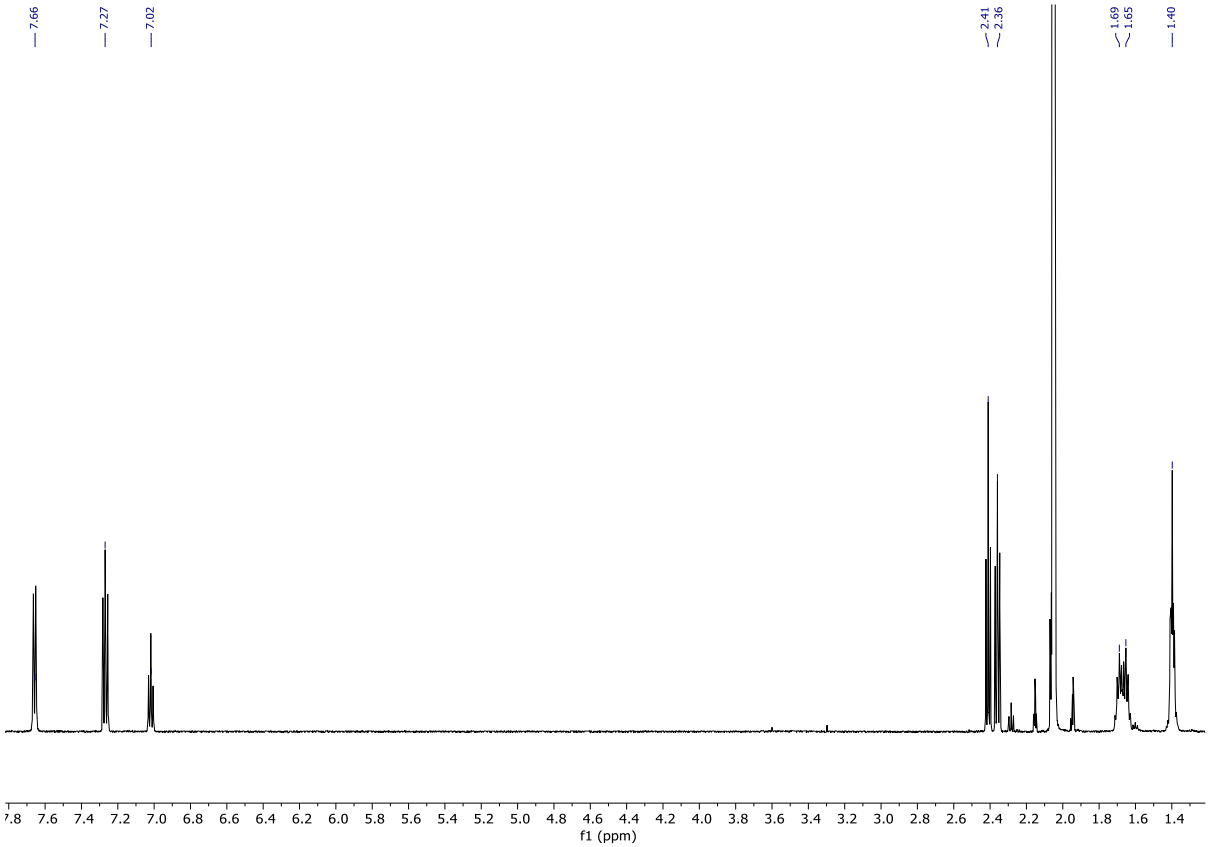

*Figure 93: ^{1}H NMR spectrum of **47** in MeOD.*

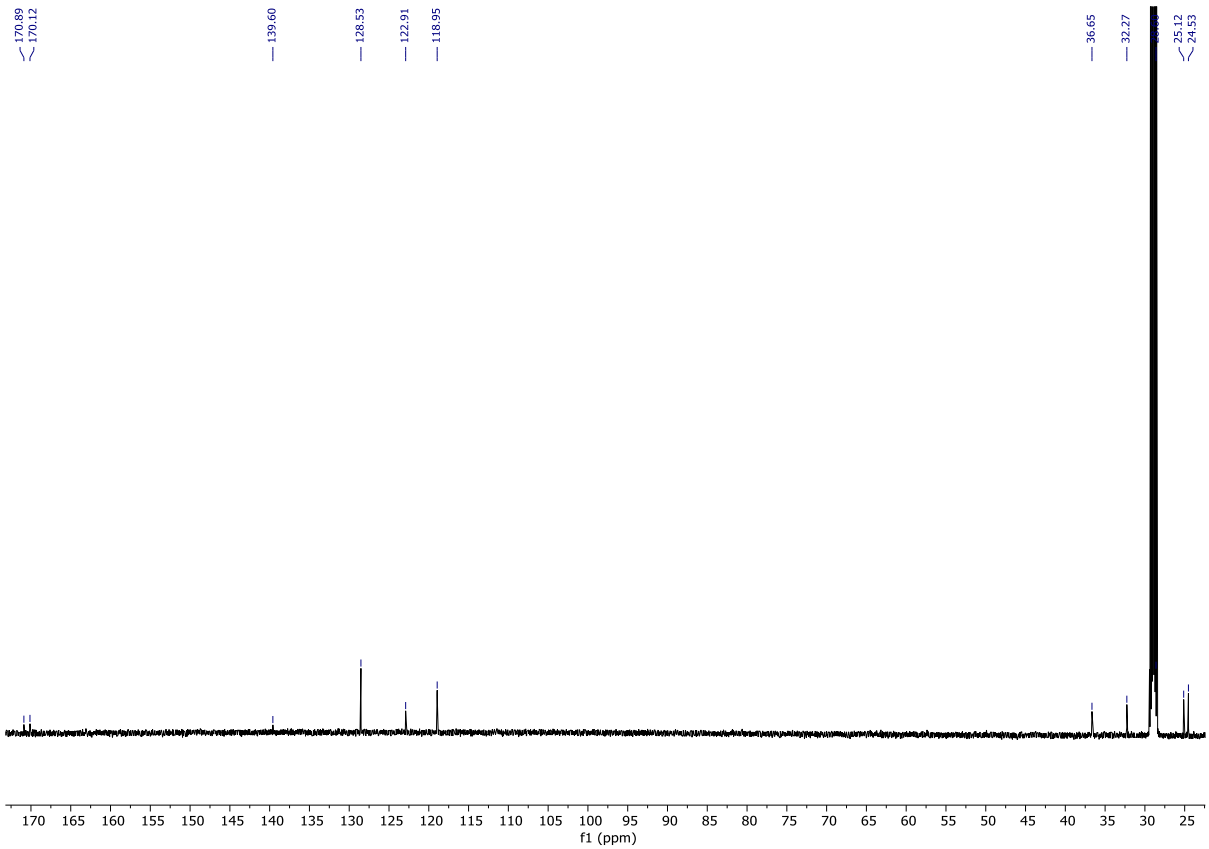

*Figure 94: ^{13}C NMR spectrum of **47** in MeOD.*

5 | REFERENCES

1 S. H. Hassanpour and M. Dehghani, *J. Cancer Res. Pract.*, 2017, **4**, 127–129.

2 World Cancer Research Fund, *World Cancer Res. Fund Int.*, 2021, 1–4.

3 C. E. Meacham and S. J. Morrison, *Nature*, 2013, **501**, 328–337.

4 R. Fisher, L. Pusztai and C. Swanton, *Br. J. Cancer*, 2013, **108**, 479–485.

5 R. L. Siegel, K. D. Miller and A. Jemal, *CA. Cancer J. Clin.*, 2016, **66**, 7–30.

6 J. F. J. D Schottenfeld, *Cancer Epidemilogy & Prevention*, Oxford University Press, 2006.

7 NHS, *What Are Heal. Risks Smok.*, 2018, **3**, 1.

8 P. Anand, A. B. Kunnumakara, C. Sundaram, K. B. Harikumar, S. T. Tharakan, O. S. Lai, B. Sung and B. B. Aggarwal, *Pharm. Res.*, 2008, **25**, 2097–2116.

9 D. M. Parkin, *Int. J. Cancer*, 2006, **118**, 3030–3044.

10 G. Matlashewski, P. Lamb, D. Pim, J. Peacock, L. Crawford and S. Benchimol, *EMBO J.*, 1984, **3**, 3257–3262.

11 E. Shtivelman, B. Lifshitz, R. P. Gale and E. Canaani, *Nature*, 1985, **315**, 550–554.

12 M. De Moura and B. Van Houten, *Environ. Mol. Mutagen.*, 2010, **405**, 391–405.

13 E. R. Álvarez-Buylla, Á. Chaos, M. Aldana, M. Benítez, Y. Cortes-Poza, C. Espinosa-Soto, D. A. Hartasánchez, R. B. Lotto, D. Malkin, G. J. Escalera Santos and P. Padilla-Longoria, *PLoS One*, 2008, **3**, 11-14.

14 A. Portela and M. Esteller, *Nat. Biotechnol.*, 2010, **28**, 1057–1068.

15 B. Jin, Y. Li and K. D. Robertson, *Genes and Cancer*, 2011, **2**, 607–617.

16 A. S. Wilson, B. E. Power and P. L. Molloy, *Biochim. Biophys. Acta - Rev. Cancer*, 2007, **1775**, 138–162.

17 M. Li, W. D. Chen, N. Papadopoulos, S. N. Goodman, N. C. Bjerregaard, S. Laurberg, B. Levin, H. Juhl, N. Arber, H. Moinova, K. Durkee, K. Schmidt, Y. He, F. Diehl, V. E. Velculescu, S. Zhou, L. A. Diaz, K. W. Kinzler, S. D. Markowitz and B. Vogelstein, *Nat. Biotechnol.*, 2009, **27**, 858–863.

18 A. Doi, I. H. Park, B. Wen, P. Murakami, M. J. Aryee, R. Irizarry, B. Herb, C. Ladd-Acosta, J. Rho, S. Loewer, J. Miller, T. Schlaeger, G. Q. Daley and A. P. Feinberg, *Nat. Genet.*, 2009, **41**, 1350–1353.

19 Z. Zhao and A. Shilatifard, *Genome Biol.*, 2019, **20**, 1–16.

20 X. J. Yang and E. Seto, *Oncogene*, 2007, **26**, 5310–5318.

21 P. ten Holte, K. Van Emelen, M. Janicot, P. C. Fong, J. S. de Bono and J. Arts, 2007, 293–331.

22 E. J. Noonan, R. F. Place, D. Pookot, S. Basak, J. M. Whitson, H. Hirata, C. Giardina and R. Dahiya, *Oncogene*, 2009, **28**, 1714–1724.

23 M. A. Glozak and E. Seto, *Oncogene*, 2007, **26**, 5420–5432.

24 V. V. Padma, *Biomed.*, 2015, **5**, 1–6.

25 R. Benedetti, M. Conte, C. Dell'Aversana, F. K. Hansen and C. Zwergel, *Front. Chem.*, 2020, **8**, 3–4.

26 U. Ndagi, N. Mhlongo and M. E. Soliman, *Drug Des. Devel. Ther.*, 2017, **11**, 599–616.

27 R. L. Lucaciu, A. C. Hangan, B. Sevastre and L. S. Oprean, *Molecules*, 2022, **27**, DOI:10.3390/molecules27196485.

28 S. Dasari and P. Bernard Tchounwou, *Eur. J. Pharmacol.*, 2014, **740**, 364–378.

29 T. C. Johnstone, K. Suntharalingam and S. J. Lippard, *Chem. Rev.*, 2016, **116**, 3436–3486.

30 A. Brown, S. Kumar and P. B. Tchounwou, *J. Cancer Sci. Ther.,* 2019, **4**, 1-15.

31 J. C. Dabrowiak, *Metals in Medicine*, 2012, vol. 393.

32 S. E. Miller and D. A. House, *Inorganica Chim. Acta*, 1989, **161**, 131–137.

33 S. E. Miller and D. A. House, *Inorganica Chim. Acta*, 1989, **166**, 189–197.

34 S. E. Miller, K. J. Gerard and D. A. House, *Inorganica Chim. Acta*, 1991, **190**, 135–144.

35 S. J. Berners-Price, L. Ronconi and P. J. Sadler, *Prog. Nucl. Magn. Reson. Spectrosc.*, 2006, **49**, 65–98.

36 T. C. Johnstone, G. Y. Park and S. J. Lippard, *Anticancer Res.*, 2014, **34**, 471–476.

37 T. Makovec, *Radiol. Oncol.*, 2019, **53**, 148–158.

38 K. U. Maheswari, T. Ramachandran and D. Rajaji, *Biochim. Biophys. Acta - Biomembr.*, 2000, **1463**, 230–240.

39 G. Speelmans, W. H. H. M. Sips, R. J. H. Grisel, R. W. H. M. Staffhorst, A. M. J. Fichtinger-Schepman, J. Reedijk and B. De Kruijff, *Biochim. Biophys. Acta - Biomembr.*, 1996, **1283**, 60–66.

40 H. Burger, A. Zoumaro-Djayoon, A. W. M. Boersma, J. Helleman, E. M. J. J. Berns, R. H. J. Mathijssen, W. J. Loos and E. A. C. Wiemer, *Br. J. Pharmacol.*, 2010, **159**, 898–908.

41 A. Schoeberl, M. Gutmann, S. Theiner, M. Corte-Rodríguez, G. Braun, P. Vician, W. Berger and G. Koellensperger, *Front. Mol. Biosci.*, 2022, **9**, 1–14.

42 J. T. Rubino and K. J. Franz, *J. Inorg. Biochem.*, 2012, **107**, 129–143.

43 V. K. Sharma and J. K. Watts, *Future Med. Chem.*, 2015, **7**, 2221–2242.

44 D. Kilari, E. Guancial and E. S. Kim, *World J. Clin. Oncol.*, 2016, **7**, 106–113.

45 and M. J. S. Stephen B. Howell, Roohangiz Safaei, Christopher A. Larson, *Mol. Pharmacol.*, 2010, **77**, 887–894.

46 D. W. Shen, L. M. Pouliot, M. D. Hall and M. M. Gottesman, *Pharmacol. Rev.*, 2012, **64**, 706–721.

47 J. A. Howle and G. R. Gale, *Biochem. Pharmacol.*, 1970, **19**, 2757–2762.

48 A. M. J. Fichtinger-Schepman, P. H. M. Lohman, J. L. van der Veer, J. H. J. den Hartog and J. Reedijk, *Biochemistry*, 1985, **24**, 707–713.

49 M. H. Baik, R. A. Friesner and S. J. Lippard, *J. Am. Chem. Soc.*, 2003, **125**, 14082–14092.

50 M. S. Davies, S. J. Berners-Price and T. W. Hambley, *Inorg. Chem.*, 2000, **39**, 5603–5613.

51 C. R. Centerwall, D. J. Kerwood, J. Goodisman, B. B. Toms and J. C. Dabrowiak, *J. Inorg. Biochem.*, 2008, **102**, 1044–1049.

52 C. R. R. Rocha, M. M. Silva, A. Quinet, J. B. Cabral-Neto and C. F. M. Menck, *Clinics*, 2018, **73**, 1–10.

53 S. A. Aldossary, *Biomed. Pharmacol. J.*, 2019, **12**, 7–15.

54 S. Dhar and S. J. Lippard, *Platin. Other Heavy Met. Compd. Cancer Chemother.*, 2009, 135–147.

55 T. C. Johnstone, K. Suntharalingam and S. J. Lippard, *Philos. Trans. R. Soc. A Math. Phys. Eng. Sci.*, 2014, DOI:10.1098/rsta.2014.0185.

56 J. M. Cross, N. Gallagher, J. H. Gill, M. Jain, A. W. McNeillis, K. L. Rockley, F. H. Tscherny, N. J. Wirszycz, D. S. Yufit and J. W. Walton, *Dalt. Trans.*, 2016, **45**, 12807–12813.

57 N. Muhammad and Z. Guo, *Curr. Opin. Chem. Biol.*, 2014, **19**, 144–153.

58 W. M. Motswainyana and P. A. Ajibade, *Adv. Chem.*, 2015, **2015**, 1–21.

59 M. J. Clarke, F. Zhu and D. R. Frasca, *Chem. Rev.*, 1999, **99**, 2511–2533.

60 L. Côrte-Real, F. Mendes, J. Coimbra, T. S. Morais, A. I. Tomaz, A. Valente, M. H. Garcia, I. Santos, M. Bicho and F. Marques, *J. Biol. Inorg. Chem.*, 2014, **19**, 853–867.

61 I. Kostova, *Curr. Med. Chem.*, 2006, **13**, 1085–1107.

62 P. Zhang and P. J. Sadler, *Eur. J. Inorg. Chem.*, 2017, **2017**, 1541–1548.

63 G. K. Gransbury, P. Kappen, C. J. Glover, J. N. Hughes, A. Levina, P. A. Lay, I. F. Musgrave and H. H. Harris, *Metallomics*, 2016, **8**, 762–773.

64 A. Bergamo, A. Masi, M. A. Jakupec, B. K. Keppler and G. Sava, *Met. Based. Drugs*, 2009, DOI:10.1155/2009/681270.

65 S. Leijen, S. A. Burgers, P. Baas, D. Pluim, M. Tibben, E. Van Werkhoven, E. Alessio, G. Sava, J. H. Beijnen and J. H. M. Schellens, *Invest. New Drugs*, 2015, **33**, 201–214.

66 H. Huang, P. Zhang, B. Yu, Y. Chen, J. Wang, L. Ji and H. Chao, *J. Med. Chem.*, 2014, **57**, 8971–8983.

67 V. R. Putta, N. Chintakuntla, R. R. Mallepally, S. Avudoddi, K. Nagasuryaprasad, D. Nancherla, V. V. N. Yaswanth, R. S. Prakasham, S. S. Surya and S. Sirasani, *J. Fluoresc.*, 2016, **26**, 225–240.

68 Fabiana Meijon Fadul, .

69 A. Weiss, R. H. Berndsen, M. Dubois, C. Müller, R. Schibli, A. W. Griffioen, P. J. Dyson and P. Nowak-Sliwinska, *Chem. Sci.*, 2014, **5**, 4742–4748.

70 P. J. S. Robert E. Morris, Rhona E. Aird, Piedad del Socorro Murdoch, Haimei Chen, Jeff Cummings, Nathan D. Hughes, Simon Parsons, Andrew Parkin, Gary Boyd, Duncan I. Jodrell, *Am. Chem. Soc.*, 2001, **44**, 3616–3621.

71 L. Zeng, P. Gupta, Y. Chen, E. Wang, L. Ji, H. Chao and Z. S. Chen, *Chem. Soc. Rev.*, 2017, **46**, 5771–5804.

72 M. Kellert, I. Sárosi, R. Rajaratnam, E. Meggers, P. Lönnecke and E. Hey-Hawkins, *Molecules*, 2020, **25**, 1–12.

73 S. Y. Lee, C. Y. Kim and T. G. Nam, *Drug Des. Devel. Ther.*, 2020, **14**, 5375–5392.

74 P. Ji, P. Wang, H. Chen, Y. Xu, J. Ge, Z. Tian and Z. Yan, *Pharmaceuticals*, 2023, DOI:10.3390/ph16020234.

75 A. Gupta and S. Lutsenko, *Future Med. Chem.*, 2009, **1**, 1125–1142.

76 M. Sutradhar, Rajeshwari, T. Roy Barman, A. R. Fernandes, F. Paradinha, C. Roma-Rodrigues, M. F. C. Guedes da Silva and A. J. L. Pombeiro, *J. Inorg. Biochem.*, 2017, **175**, 267–275.

77 A. Maroń, K. Czerwińska, B. Machura, L. Raposo, C. Roma-Rodrigues, A. R. Fernandes, J. G. Małecki, A. Szlapa-Kula, S. Kula and S. Krompiec, *Dalt. Trans.*, 2018, **47**, 6444–6463.

78 Z. Shokohi-Pour, H. Chiniforoshan, A. A. Momtazi-Borojeni and B. Notash, *J. Photochem. Photobiol. B Biol.*, 2016, **162**, 34–44.

79 J. Hormann, J. Malina, O. Lemke, M. J. Hülsey, S. Wedepohl, J. Potthoff, C. Schmidt, I. Ott, B. G. Keller, V. Brabec and N. Kulak, *Inorg. Chem.*, 2018, **57**, 5004–5012.

80 C. Trejo-Solís, D. Jimenez-Farfan, S. Rodriguez-Enriquez, F. Fernandez-Valverde, A. Cruz-Salgado, L. Ruiz-Azuara and J. Sotelo, *BMC Cancer*, 2012, **12**, DOI:10.1186/1471-2407-12-156.

81 S. T. Chew, K. M. Lo, S. K. Lee, M. P. Heng, W. Y. Teoh, K. S. Sim and K. W. Tan, *Eur. J. Med. Chem.*, 2014, **76**, 397–407.

82 S. S. Hindo, M. Frezza, D. Tomco, M. J. Heeg, L. Hryhorczuk, B. R. McGarvey, Q. P. Dou and C. N. Verani, *Eur. J. Med. Chem.*, 2009, **44**, 4353–4361.

83 D. S. Sigman, D. R. Graham, V. D'Aurora and A. M. Stern, *J. Biol. Chem.*, 1979, **254**, 12269–12272.

84 S. J. McKie, K. C. Neuman and A. Maxwell, *BioEssays*, 2021, **43**, 1–19.

85 S. Tabassum, M. Afzal and F. Arjmand, *J. Photochem. Photobiol. B Biol.*, 2012, **115**, 63–72.

86 Q. Ban, J. Du, W. Sun, J. Chen, S. Wu and J. Kong, *Macromol. Rapid Commun.*, 2018, **39**, 1–6.

87 H. J. Kim and S. C. Bae, *Am. J. Transl. Res.*, 2011, **3**, 166–179.

88 P. A. Wade, *Hum. Mol. Genet.*, 2001, **10**, 693–698.

89 W. Ellmeier and C. Seiser, *Nat. Rev. Immunol.*, 2018, **18**, 617–634.

90 A. J. M. De Ruijter, A. H. Van Gennip, H. N. Caron, S. Kemp and A. B. P. Van Kuilenburg, *Biochem. J.*, 2003, **370**, 737–749.

91 W. Fischle, F. Dequiedt, M. J. Hendzel, M. G. Guenther, M. A. Lazar, W. Voelter and E. Verdin, *Mol. Cell*, 2002, **9**, 45–57.

92 L. Gao, M. A. Cueto, F. Asselbergs and P. Atadja, *J. Biol. Chem.*, 2002, **277**, 25748–25755.

93 P. Bjerling, R. A. Silverstein, G. Thon, A. Caudy, S. Grewal and K. Ekwall, *Mol. Cell. Biol.*, 2002, **22**, 2170–2181.

94 Y. K. Shi, M. Dong, X. Hong, W. Zhang, J. Feng, J. Zhu, L. Yu, X. Ke, H. Huang, Z. Shen, Y. Fan, W. Li, X. Zhao, J. Qi, H. Huang, D. Zhou, Z. Ning and X. Lu, *Ann. Oncol.*, 2015, **26**, 1766–1771.

95 M. Manal, M. J. N. Chandrasekar, J. Gomathi Priya and M. J. Nanjan, *Bioorg. Chem.*, 2016, **67**, 18–42.

96 A. Petrich and C. Nabhan, *Leuk. Lymphoma*, 2016, **57**, 1755–1765.

97 Y. Li and E. Seto, *Cold Spring Harb. Perspect. Med.*, 2016, **6**, 1–34.

98 J. W. Walton, J. M. Cross, T. Riedel and P. J. Dyson, *Org. Biomol. Chem.*, 2017, **15**, 9186–9190.

99 J. M. Cross, T. R. Blower, A. D. H. Kingdon, R. Pal, D. M. Picton and J. W. Walton, *Molecules*, 2020, **25**, DOI:10.3390/molecules25102383.

100 C. Tang, Y. Du, Q. Liang, Z. Cheng and J. Tian, *Organometallics*, 2018, **37**, 2368–2375.

101 J. Spencer, J. Amin, M. Wang, G. Packham, S. S. S. Alwi, G. J. Tizzard, S. J. Coles, R. M. Paranal, J. E. Bradner and T. D. Heightman, *ACS Med. Chem. Lett.*, 2011, **2**, 358–362.

102 D. Griffith, M. P. Morgan and C. J. Marmion, *Chem. Commun.*, 2009, 6735–6737.

103 M. Hanif, J. Arshad, J. W. Astin, Z. Rana, A. Zafar, S. Movassaghi, E. Leung, K. Patel, T. Söhnel, J. Reynisson, V. Sarojini, R. J. Rosengren, S. M. F. Jamieson and C. G. Hartinger, *Angew. Chemie - Int. Ed.*, 2020, **59**, 14609–14614.

104 W. Liao, W. Yang, J. Xu, Z. Yan, M. Pan, X. Xu, S. Zhou, Y. Zhu, J. Lan, M. Zeng, X. Han, S. Li, Y. Li, K. Liang, Y. Gao and Q. Peng, *Front. Pharmacol.*, 2021, **12**, 1–13.

105 A. Manuscript, *Cancer*, 2011, **8**, 627–644.

106 K. Zhang, F. Lai, S. Lin, M. Ji, J. Zhang, Y. Zhang, J. Jin, R. Fu, D. Wu, H. Tian, N. Xue, L. Sheng, X. Zou, Y. Li, X. Chen and H. Xu, *J. Med. Chem.*, 2019, **62**, 6992–7014.

107 C. Santini, M. Pellei, V. Gandin, M. Porchia, F. Tisato and C. Marzano, *Chem. Rev.*, 2014, **114**, 815–862.

108 C. Slator, Z. Molphy, V. McKee, C. Long, T. Brown and A. Kellett, *Nucleic Acids Res.*, 2018, **46**, 2733–2750.

109 J. King, M. Patel and S. Chandrasekaran, *Metabolites*, 2021, DOI:10.3390/METABO11110792.

110 T. J. P. McGivern, C. Slator, A. Kellett and C. J. Marmion, *Mol. Pharm.*, 2018, **15**, 5058–5071.

111 J. M. Cross, T. R. Blower, N. Gallagher, J. H. Gill, K. L. Rockley and J. W. Walton, *Chempluschem*, 2016, **81**, 1276–1280.

112 A. Mishra, K. Y. Djoko, Y. H. Lee, R. M. Lord, G. Kaul, A. Akhir, D. Saxena, S. Chopra and J. W. Walton, *Org. Biomol. Chem.*, 2023, **21**, 2539–2544.

113 R. N. Adamek, C. N. Suire, R. W. Stokes, M. K. Brizuela, S. M. Cohen and M. A. Leissring, *ChemMedChem*, 2021, **16**, 1775–1787.

114 G. Giacomelli, A. Porcheddu and M. Salaris, *Org. Lett.*, 2003, **5**, 2715–2717.

115 R. Muthyala, W. S. Shin, J. Xie and Y. Y. Sham, *Bioorganic Med. Chem. Lett.*, 2015, **25**, 4320–4324.

116 X. Yuan, H. Wu, H. Bu, P. Zheng, J. Zhou and H. Zhang, *Bioorganic Med. Chem.*, 2019, **27**, 1211–1225.

117 S. M. A. Hussaini, P. Yedla, K. S. Babu, T. B. Shaik, G. K. Chityal and A. Kamal, *Chem. Biol. Drug Des.*, 2016, **4**, 97–109.

118 XANES - Chemistry LibreTexts, https://chem.libretexts.org/Bookshelves/Physical_and_Theoretical_Chemistry_Textbook_Maps/Supplemental_Modules_(Physical_and_Theoretical_Chemistry)/Spectroscopy/X-ray_Spectroscopy/XANES, (accessed 10 September 2022).